FIRST-PRINCIPLES STUDY OF ELECTRIC POLARIZATION IN PIEZOELECTRIC AND MAGNETOELECTRIC MATERIALS

by

ANDREI MALASHEVICH

A Dissertation submitted to the

Graduate School-New Brunswick

Rutgers, The State University of New Jersey

In partial fulfillment of the requirements

For the degree of

Doctor of Philosophy

Graduate Program in Physics and Astronomy

Written under the direction of

Professor David Vanderbilt

And approved by

_____

_____

_____

_____

_____

New Brunswick, New Jersey

October, 2009

ABSTRACT OF THE DISSERTATION

First-principles study of electric polarization in piezoelectric and magnetoelectric materials

By ANDREI MALASHEVICH

Dissertation Director:

Professor David Vanderbilt

First-principles calculations based on the density-functional theory (DFT) have proven to be extremely useful in the study of properties of matter. Not only do they provide a sufficient accuracy to reproduce experimental results, but also they make it possible to predict materials with enhanced or even new properties. Often first-principles calculations become a cheap alternative to real experiments or even allow one to investigate regimes not accessible experimentally either in principle or because of limitations of experimental techniques. But the real power of methods based on computer simulations is that they can help one to understand the microscopic mechanisms of physical processes inside the materials.

In my thesis work I will analyze electric polarization properties of several materials and their dependence on some physical parameters such as strain, chemical doping, and magnetic order.

In the first part of my thesis I will present an *ab-initio* study of wurtzite ZnO doped with Mg. Several ordered structures modeling the $Zn_{1-x}Mg_xO$ alloy are analyzed with different Mg concentrations. The electric polarization is studied as a function of Mg concentration x under different strain conditions. We find that to a good approximation the polarization depends linearly on x. We show that a simple model based on the piezoelectric response of pure ZnO can reproduce the results fairly well.

In the second part, we study the magnetoelectric coupling in a spiral magnet $TbMnO_3$. It is known from experiment that at low temperatures a ferroelectric phase appears simultaneously with the onset of a cycloidal magnetic order. Using first-principles methods, we demonstrate that ferroelectricity in this material is indeed driven by magnetic order. We show that spin-orbit coupling is essential for the electric polarization to appear. We also demonstrate that the ionic displacements induced by a cycloidal magnetic order, though tiny, play a crucial role in producing polarization. We do a detailed analysis of the forces on ions and ionic displacements from the mode-decomposition viewpoint, and find that simple models based only on nearest-neighbor interactions between Mn ions through oxygen are not able to account fully for the results.

Acknowledgements

I am immensely thankful to Professor David Vanderbilt for his support, guidance and teaching during my graduate study at Rutgers University. He sets a great example of what it means to be a scientist. It is a great honor to be one of his students.

I would like to thank my wife, Maryna, who gives me so much love and happiness and always inspires me to achieve new goals.

I would like to thank my parents, Lyudmila and Sergei Malashevich, and my brother, Dmitry Malashevich, for their support and encouragements.

Thanks to my friends and office mates, Yury Polyanskiy, Nikolai Klimov, Evgeny Andriyash, Aleko Khukhunaishvili, Grigol Ovanesyan, Alexey Soluyanov, Jeffrey Goett, Iskander Ziyatdinov, Alexey Litvinov, Sinisa Coh, Xifan Wu, Anindya Roy, Lucia Palova, Carl-Johan Eklund, Rebecca Flint, Oscar Paz, Craig Fennie, Viktor Oudovenko, Valentino Cooper, Eamonn Murray, Junhee Lee, Takeshi Nishimatsu, Alexey Zayak, Xinjie Wang, and Scott Beckman.

Many thanks to the faculty and collaborators, Professors Karin Rabe, Premala Chandra, Morrel Cohen, Piers Coleman, Sang-Wook Cheong, Nicola Spaldin, and Kristjan Haule, for their numerous valuable discussions.

I would also like to thank Andrei Zaboronok and Anatoly Slobodyanyuk who opened the door to the World of Science for me.

Table of Contents

List of Tables

List of Figures

Chapter 1

Introduction

1.1 Electric polarization and types of insulating crystals

Electric polarization in a finite crystal is defined as an electric dipole moment per volume of the crystal. If we denote the charge density as $\rho(\mathbf{r})$ and assume that the crystal is neutral as a whole, then we can write

$$\int \rho(\mathbf{r})d^3r = 0. \tag{1.1}$$

In this case one can define the polarization in the crystal as

$$\mathbf{P} = \frac{1}{V} \int_V \rho(\mathbf{r})\mathbf{r}\, d^3r, \tag{1.2}$$

where V is the volume of the crystal. Because of charge neutrality this definition does not depend on the origin. However, there are several problems with it. First, as can easily be shown [5], the redistribution of surface charges leads to a finite change in the polarization defined by Eq. 1.2. Therefore, this is not a good definition of polarization as a bulk property of the crystal. In this section, we shall assume that the surfaces are perfect and free of defects, so that we don't have to worry about surface effects. Also, in the above we assume that the crystal is uniform. If the crystal is not uniform then one needs to define polarization as a function of position $\mathbf{r}$. One could assume that this can be done by taking the above definition and redefining V as a 'small' volume around $\mathbf{r}$, and then take a limit $V \to 0$. But as this limit is not guaranteed to exist, the above definition is not suitable in this case. We will return to the question of the definition of polarization later (see Sec. 2.5) and will see that a bulk definition is possible freeing us from any assumption about the surface. In this work we will not consider non-uniform crystals, and the above definition is sufficient for the discussion of the types of insulating crystals below.

In ordinary insulators the electric polarization appears only when they are placed in an external electric field. If the electric field is removed, the polarization also disappears. Typically, in such materials, the dependence of polarization on applied electric field is linear and is characterized by the dielectric tensor. Many crystals, however, have finite polarization even in the absence of the external electric field. Such polarization is called *spontaneous polarization*, and crystals having spontaneous polarization are called *pyroelectrics*. The term pyroelectricity comes from the fact that spontaneous polarization depends on temperature. The change in temperature then induces a flow of charge between the surfaces, which is the pyroelectric effect.

In some crystals the spontaneous polarization can be switched by application of an electric field. Such materials are called *ferroelectrics* (or sometimes, in the Russian literature, *segneto-electrics*) [6]. The dependence of polarization on electric field has a hysteretic behavior analogous to that of ferromagnets, in which the magnetization depends on applied magnetic field in a similar fashion. This is the origin of the term 'ferroelectricity'. Ferroelectric hysteresis loops were first observed by Valasek in 1920 [7] in potassium sodium tartrate or Rochelle salt ($KNaC_4H_4O_6 \cdot 4H_2O$). This salt was first prepared in the 17th century by Pierre Seignette of La Rochelle, and the term 'segnetoelectric' takes its origin from his name.

Electric polarization can be induced by applying stress in some crystals. This effect is called *piezoelectricity*. All pyroelectric (and therefore all ferroelectric) materials display piezoelectricity. In fact, an analysis of the symmetry of the crystal can predict whether the crystal will be piezoelectric (or pyroelectric). There are 32 crystal symmetry classes, of which 21 are non-centrosymmetric; 20 of these can be piezoelectric, and 10 of these can have spontaneous polarization (i.e. be pyroelectric).

Ferroelectrics find many applications in technology. They can be used in tunable high permittivity capacitors, non-volatile memory devices like FeRAM, sensors, etc. Piezoelectrics are also widely used in devices where high-precision pointing is required, e.g., in scanning tunneling and atomic force microscopy.

1.2 Improper ferroelectrics

A phase transition is called ferroelectric if spontaneous polarization arises in the transition. Ferroelectric phase transitions are often described by a phenomenological Landau theory of second-order phase transitions [8] in which an order parameter is an essential ingredient. In ordinary ferroelectrics, the role of the order parameter is played by electric polarization. But this does not always have to be the case. It is possible to have an order parameter other than polarization, and at the same time polarization also can appear in the phase transition. Materials showing this behavior are called *improper ferroelectrics* [9].
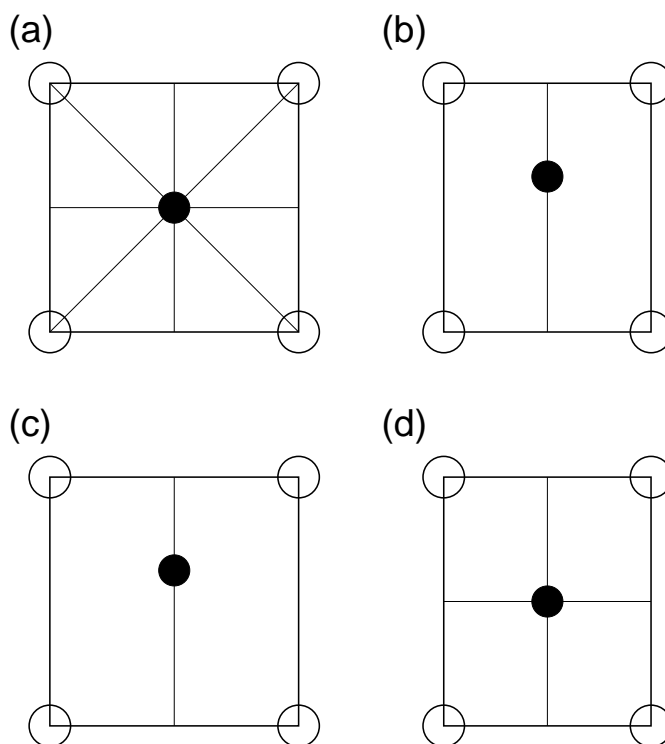
Figure 1.1: Schematic illustration of barium titanate phases related to a ferroelectric phase transition: (a) initial high-temperature cubic phase, (b) final low-temperature tetragonal phase (ferroelectric phase), (c) polarized cubic structure having the same symmetry as (b), (d) deformed high-temperature phase having higher symmetry than (b). Open circles represent Ba sites, while filled circles represent Ti sites. The figure demonstrates that the order parameter in $BaTiO_3$ ferroelectric phase transition is polarization.

To illustrate this point, consider the barium titanate ($BaTiO_3$) transition from the cubic to the

tetragonal phase. This transition is accompanied by the appearance of spontaneous polarization and spontaneous deformation of the crystal. If one clamps the crystal, so that the lattice vectors remain cubic, and polarizes it along one direction as shown in Fig. 1.1(c), the symmetry of the crystal will be the same as in tetragonal phase observed experimentally, shown in Fig. 1.1(b). On the other hand, if one deforms the crystal to force it to tetragonal phase, as in Fig. 1.1(d), the deformed crystal will have a higher symmetry than that observed in the phase transition. Namely, the inversion symmetry will still be present, and polarization will not appear. This shows that the order parameter here is indeed polarization, and therefore $BaTiO_3$ is a *proper* ferroelectric.

In improper ferroelectrics, if one polarizes the initial phase, one will get a higher symmetry than that observed in the actual phase transition. This means that in a phase transition in improper ferroelectrics, the appearance of polarization is not a primary effect but rather a secondary (parasitic) effect accompanying the appearance of some other order parameter. As an example, consider the ferroelectric phase transition in hexagonal $YMnO_3$ [10]. One could imagine that, as in many other ferroelectrics, the polarization in $YMnO_3$ appears due to the softening of the Γ-centered phonon modes. However, as it was shown with the help of first-principles calculations [11], all Γ-centered phonon modes in this material are, in fact, stable. Therefore, polarization is not a primary order parameter. What happens in the actual phase transition is the softening of one of the zone-boundary modes (tilts of MnO_5 trigonal bipyramids), which is a primary order parameter. Due to the coupling of the zone-boundary and zone-centered phonons, this leads to a shift of the equilibrium positions of one of the Γ-modes, thus creating a ferroelectric distortion. This shows that $YMnO_3$ is an improper ferroelectric.

Other examples of improper ferroelectrics include $TbMnO_3$, $Ni_3V_2O_8$ (both are magnetically induced ferroelectrics and are the subject of this work), rare-earth molybdates, e.g. $Gd_2(MoO_4)_3$, boracites, etc. Interestingly, the 'cousin' of the first discovered ferroelectric, ammonium Rochelle salt ($NaNH_4C_4H_4O_6 \cdot 4H_2O$), is also an improper ferroelectric [12].

1.3 Outline of the present work

The rest of this dissertation is organized as follows.

In Chapter 2, I will describe the details of the computational methods we use in our studies. The key aspects of density functional theory (DFT) [13] will be outlined here, although the fact that it is by now a well-established textbook theory means that we can do so only briefly. It is important, however, to describe to a sufficient extent the essential ingredients specific to the physics and materials studied in this work. Thus, I will describe the on-site Coulomb correction (commonly referred to as the LDA+U method) needed for a better treatment of the d-electrons in transition metals. This method will be important in the analysis of the $TbMnO_3$ system in this work. Then I will describe the Berry-phase theory of polarization, which provides a formalism suitable for infinite periodic bulk crystals. For the treatment of the magnetic structure in $TbMnO_3$, the non-collinear spin formulation of DFT is needed. To deal with the effects of the lattice and spin degrees of freedom, the spin-orbit interaction must be included in the theory. The description of these aspects will conclude the Chapter 2. The technical details specific for each system, such as energy cut-offs and Brillouine zone meshes, will be provided as needed in the later chapters.

Chapter 3 will be focused on the study of polarization in bulk wurtzite ZnO, MgO and their alloy compound $Zn_{1-x}Mg_xO$. The effects of the epitaxial strain on the polarization will be analyzed. To understand the behavior of the polarization as a function of Mg concentration in the compound, a special procedure will be used to decompose the polarization into electronic, lattice and piezoelectric contributions.

In Chapter 4, the improper ferroelectricity in the example of perovskite multiferroic $TbMnO_3$ will be discussed. First, I will give an introduction to the subject of multiferroics and the theories used to describe them. Then, the application of the above methods to the study of the mechanism of magnetoelectric coupling will be presented. The effects of the ionic displacements on the polarization will be analyzed. The chapter will be concluded with a discussion of how well present theories can account for the description of the ferroelectricity in this material.

Chapter 2

First-principles calculations

2.1 Density-functional theory

In the present work we study the properties of materials using *ab-initio* techniques. This means that we want to have a theory describing materials quantitatively without the use of any experimental parameters except fundamental physical constants. Density-functional theory (DFT) [13, 14] is one of the most successful such theories. It is an *exact* theory in principle, but approximate in practice. We use DFT in all calculations described in this work.

Density-functional theory is based on the theorem that the total energy of a system of interacting electrons can be viewed as a functional $F[n]$ of the density of electrons $n(\mathbf{r})$. The true ground-state energy is then a minimum of this functional, and the density that minimizes the functional is the true density of electrons in the ground state. Another key idea behind DFT is that the system of N interacting electrons in an external potential $V_{\text{ext}}(\mathbf{r})$ can be 'mapped' onto a system of N non-interacting electrons in an effective Kohn-Sham potential $V_{\text{KS}}(\mathbf{r})$ having the same ground state total energy and density. The Kohn-Sham potential is given by

$$V_{\text{KS}}(\mathbf{r}) = V_{\text{ext}}(\mathbf{r}) + \frac{\delta E_{\text{H}}[n]}{\delta n(\mathbf{r})} + \frac{\delta E_{\text{XC}}[n]}{\delta n(\mathbf{r})}. \tag{2.1}$$

Here, the last two terms are the *functional* derivatives of the Hartree energy and the exchange-correlation energy with respect to density. The Hartree energy is given by

$$E_{\text{H}}[n] = \frac{1}{2} \int d^3r \, d^3r' \frac{n(\mathbf{r})n(\mathbf{r}')}{|\mathbf{r} - \mathbf{r}'|}, \tag{2.2}$$

and $E_{\text{XC}}[n]$ *by definition* is everything that is not included in the kinetic energy, external potential

and Hartree terms:

$$E_{\mathrm{XC}}[n] \equiv F[n] - T_s[n] - E_{\mathrm{H}}[n] - \int d^3 r V_{\mathrm{ext}} n(\mathbf{r}). \qquad (2.3)$$

Here, $T_s[n]$ is the kinetic energy of non-interacting electrons written as a functional of density.

Now one has to solve a Schrödinger-like equations using the effective potential in the Hamiltonian (Kohn-Sham equations):

$$\left(-\frac{\hbar^2}{2m} \nabla^2 + V_{\mathrm{KS}}(\mathbf{r}) \right) \psi_i(\mathbf{r}) = \epsilon_i \, \psi_i(\mathbf{r}). \qquad (2.4)$$

Usually, this is done self-consistently, i.e., at each step the solution of the Kohn-Sham equations gives the wave functions, from which one can calculate new density, and then updates the effective potential using the new density. The process is repeated until the desired accuracy is reached.

As described, the theory is exact. The problem is that the functional $F[n]$ is not known. Equivalently, one may say that the exchange-correlation energy functional $E_{\mathrm{XC}}[n]$ is not known. In practice, people use various approximations, the most common being the local-density approximation (LDA). In this approximation, the exchange-correlation energy is taken from the homogeneous electron gas. Even though this is perhaps the simplest approximation one can make, it proved to work reasonably well for a wide range of materials. The generalization of the LDA to spin-polarized electron systems, the local spin-density approximation, will be briefly reviewed in Sec. 2.3. Throughout this work, we will use the acronym 'LDA' for systems with or without spin-polarization. When we want to emphasize that we consider the spin-polarized case, we will use the acronym 'LSDA'.

A thorough description of DFT can be found in references [15, 16].

2.2 On-site Coulomb correction

As follows from its formulation, DFT is meant to describe ground-state properties only. Thus, the density and total energy in exact DFT should be the same as in real interacting system. On the

other hand, the Kohn-Sham eigenvalues themselves are not expected to reproduce the exact energy levels of the interacting system. Nevertheless, often there is some qualitative agreement, making it appealing to do DFT calculations of the excited-states properties.

For example, in periodic solids, one can calculate the Kohn-Sham energy band structure and infer from it the band gap defined as the smallest energy difference between conduction and valence bands. In the LDA, the band gap is systematically underestimated. So if in LDA calculation one finds a finite band gap, one can expect that in the real system the band gap will be even larger, and the system can be predicted to have insulating properties.

There are many cases, however, in which the electronic structure predicted with LDA does not allow one to make definite statements about excited states. This is usually true for systems with partially filled d or f electron shells. In particular, LDA predicts many transition metal oxides to be metallic while they are experimentally found to be insulators [17, 18]. For these systems, even the ground state properties (like magnetism) can be incorrectly predicted by the LDA.

The problem is that localized d and f electrons are strongly correlated. The physics associated with the strong Coulomb repulsion between electrons localized in the same shell is not correctly captured in the LDA, which always tends to delocalize electrons. In a homogeneous-gas treatment, LDA does not distinguish electrons as separate entities in the electron gas, and the effects of localization of electrons are not reproduced. Perdew *et al.* showed [19] that in the exact density-functional the dependence of energy on the number of electrons N is a series of straight-line segments:

$$E(N + x) = (1 - x)E(N) + xE(N + 1). \tag{2.5}$$

Instead, in the LDA, $E(N)$ is a smooth function. This is one of the main reasons why the LDA fails when describing systems with strongly localized electrons.

Anisimov and coworkers [20–22] formulated a generalization of LDA, the so-called 'LDA+U' method, which adds the missing screened on-site Coulomb interaction to the theory.

Before giving a thorough description of the theory itself, we note that LDA+U is not an *ab-initio* theory in a strict sense. Here, one introduces additional terms and parameters to the original LDA functional which can be justified only to some extent by physical intuition. Though parameters of the theory have an intuitive physical meaning, they do not have a precise definition and include all sorts of screening effects. The parameters can be estimated using various approaches, e.g. constrained-LDA [23]. In practice, however, it is much easier to choose them in such a way that some physical properties (such as band gap, lattice constants, exchange constants, etc.) agree with experiment.

2.2.1 Basic idea of the LDA+U method

Suppose we have a system with partially filled d orbitals like a transition metal oxide (MnO, FeO, CoO, NiO, etc.). For simplicity, we will focus our attention on a d shell of one particular site only. Let us write the energy of the Coulomb interaction between d electrons in a Hubbard-like fashion explicitly as $U/2 \sum_{i \neq j} n_i n_j$, where n_i are occupation numbers. We add this term to the LDA functional. However, the LDA functional already has some contribution coming from the interaction of electrons in the d shell. The Hamiltonian operator corresponding to this interaction can be written as

$$\hat{H}_{\text{int}} = \frac{1}{2} U \sum_{i \neq j} \hat{n}_i \hat{n}_j. \tag{2.6}$$

The expectation value of this operator in the LDA depends on the electron density or, equivalently, on the total number of electrons N in the d shell. Therefore we can write the interaction energy in the LDA as

$$\left\langle \hat{H}_{\text{int}} \right\rangle_{\text{LDA}} = \frac{1}{2} U \left\langle \sum_{i \neq j} \hat{n}_i \hat{n}_j \right\rangle_{\text{LDA}} = \frac{1}{2} U \left\langle \left(\sum_{i,j} \hat{n}_i \hat{n}_j - \sum_i \hat{n}_i \right) \right\rangle_{\text{LDA}} =$$
$$\frac{1}{2} U \left\langle \left(\hat{N}^2 - \hat{N} \right) \right\rangle_{\text{LDA}} \approx \frac{1}{2} U N(N-1). \tag{2.7}$$

To avoid overcounting, we subtract this expression from the energy functional to obtain

$$E = E_{\mathrm{LDA}} - \frac{1}{2}UN(N-1) + \frac{1}{2}U\sum_{i \neq j} n_i n_j. \tag{2.8}$$

This is still a functional of the total density $n(\mathbf{r})$, but it depends on N occupation numbers as parameters. In such case, one can show that corresponding orbital energies are the derivatives of the total energy with respect to these parameters [24]:

$$\epsilon_i = \frac{\partial E}{\partial n_i}. \tag{2.9}$$

Inserting $N = \sum_i n_i$ into the functional (2.8), we can write

$$E = E_{\mathrm{LDA}} - \frac{1}{2}U\sum_i n_i(n_i - 1), \tag{2.10}$$

and we get for the orbital energies

$$\epsilon_i = \epsilon_{\mathrm{LDA}} - U\left(n_i - \frac{1}{2}\right). \tag{2.11}$$

One can see that the occupied orbitals ($n_i = 1$) lowered their energies by $U/2$ while the unoccupied orbitals ($n_i = 0$) increased their energies by the same amount making the difference between the energies of occupied and unoccupied d orbitals exactly U.

One can introduce charge densities $n_i(\mathbf{r})$ of particular orbitals, so that $n_i = \int d^3r\, n_i(\mathbf{r})$. Now one can view equation (2.8) as a functional of N densities. The variation of this functional with respect to the densities yields N effective potentials

$$V_i(\mathbf{r}) = V_{\mathrm{LDA}}(\mathbf{r}) - U\left(n_i - \frac{1}{2}\right). \tag{2.12}$$

One should keep in mind that U is not a bare Coulomb interaction, since it contains the screening effects of the rest of the s and p electrons. This is the essence of the LDA+U method. In the

following, we will describe the details essential for the practical implementations of this method.

2.2.2 Exchange and nonsphericity

In addition to the screened Coulomb repulsion, there is also exchange (Hund's rule) which affects only same-spin orbitals, so that now the term added to the LDA functional is

$$\frac{1}{2} \sum_{m,m',\sigma} U n_{m\sigma} n_{m'-\sigma} + \frac{1}{2} \sum_{\substack{m,m',\sigma \\ m \neq m'}} (U - J) n_{m\sigma} n_{m'\sigma}. \tag{2.13}$$

In this expression, indices m and m' run from 1 to $N/2$, because now we distinguish spins. Note that if we put $J = 0$, we will regain the previous expression $U/2 \sum_{i \neq j} n_i n_j$, where i and j run from 1 to N. Again, as in the previous case, we subtract the total energy corresponding to integer occupation numbers $U N(N-1)/2 - J \left(N^\uparrow (N^\uparrow - 1) + N^\downarrow (N^\downarrow - 1) \right) / 2$ to arrive at the functional

$$E = E_{\text{LDA}} - \left[\frac{1}{2} U N(N-1) - \frac{1}{2} J \sum_\sigma N^\sigma (N^\sigma - 1) \right] +$$
$$\frac{1}{2} \sum_{m,m',\sigma} U n_{m\sigma} n_{m'-\sigma} + \frac{1}{2} \sum_{\substack{m,m',\sigma \\ m \neq m'}} (U - J) n_{m\sigma} n_{m'\sigma}. \tag{2.14}$$

Here we have introduced the notation $N^\sigma = \sum_m n_{m\sigma}$.

This functional can be generalized further by assuming that Coulomb and exchange interactions depend on what particular orbitals are occupied (nonsphericity). This means that parameters U and J must be replaced by matrices $U_{mm'}$ and $J_{mm'}$ leading to the functional [25]

$$E = E_{\text{LDA}} - \left[\frac{1}{2} U N(N-1) - \frac{1}{2} J \sum_\sigma N^\sigma (N^\sigma - 1) \right] +$$
$$\frac{1}{2} \sum_{m,m',\sigma} U_{mm'} n_{m\sigma} n_{m'-\sigma} + \frac{1}{2} \sum_{\substack{m,m',\sigma \\ m \neq m'}} (U_{mm'} - J_{mm'}) n_{m\sigma} n_{m'\sigma}, \tag{2.15}$$

where U is the average over all orbitals of $U_{mm'}$ and $(U-J)$ is the average of $(U_{mm'} - J_{mm'})$:

$$U = \frac{1}{(2l+1)^2} \sum_{m,m'} U_{mm'},$$

$$U - J = \frac{1}{2l(2l+1)} \sum_{m \neq m'} (U_{mm'} - J_{mm'}).$$

(2.16)

Note that we consider U and $(U-J)$ (and not U and J) because the average is taken over different numbers of orbitals in the above two expressions.

The term in square brackets in Eq. (2.15) is sometimes referred to as the double-counting term, $E_{dc}[\{n\}]$, so that schematically one can write

$$E_{\mathrm{LDA}+U}[\rho(\mathbf{r}), \{n\}] = E_{\mathrm{LDA}}[\rho(\mathbf{r})] + E_U[\{n\}] - E_{dc}[\{n\}],$$

(2.17)

where $\rho(\mathbf{r})$ is the usual charge density and $\{n\}$ is a set of occupations of d of f orbitals, $n_{m\sigma}$.

2.2.3   Rotationally invariant formulation

The on-site Coulomb correction formulated above is not really convenient for practical implementation. The reason is that the parameters $U_{mm'}$ and $J_{mm'}$ depend on the choice of basis. If, for example, we rotate the coordinate axes, we will get a different set of d (or f) orbitals leading to a new set of parameters.

Fortunately, there is a way to formulate a rotationally invariant version of the LDA+U method [20]. We will work in a localized orthonormal basis of $|nlm\sigma\rangle$ at each site. For simplicity, we will also restrict ourselves to particular n and l quantum numbers, and from now on we drop corresponding labels. Instead of orbital densities $n_{m\sigma}$ one can define density matrices $n^{\sigma}_{mm'}$. One can proceed then in the same way as before and write a similar functional as in Eq. (2.17). This time, for the U

term we have a Hartree-Fock type expression

$$E_U[\{n\}] = \frac{1}{2} \sum_{\{m\},\sigma} \Bigg[\langle m, m''|V_{\text{ee}}|m', m'''\rangle n^{\sigma}_{mm'} n^{-\sigma}_{m''m'''} +$$

$$\Big(\langle m, m''|V_{\text{ee}}|m', m'''\rangle - \langle m, m''|V_{\text{ee}}|m''', m'\rangle \Big) n^{\sigma}_{mm'} n^{\sigma}_{m''m'''} \Bigg]. \quad (2.18)$$

Here V_{ee} is a Coulomb interaction, and $|m, m'\rangle = |m\rangle \otimes |m'\rangle$. To arrive to this expression, one can start from the well-known second-quantized form of the electron-electron interaction operator

$$\hat{V}_{\text{ee}} = \frac{1}{2} \sum_{\sigma,\sigma'} \int d^3 r \int d^3 r' V_{\text{ee}}(\mathbf{r} - \mathbf{r}') \hat{\Psi}^{\dagger}_{\sigma}(\mathbf{r}) \hat{\Psi}^{\dagger}_{\sigma'}(\mathbf{r}') \hat{\Psi}_{\sigma'}(\mathbf{r}') \hat{\Psi}_{\sigma}(\mathbf{r}). \quad (2.19)$$

Then the field operators $\hat{\Psi}_{\sigma}(\mathbf{r})$ can be expanded in the $|nlm\sigma\rangle$ basis as

$$\hat{\Psi}_{\sigma}(\mathbf{r}) = \sum_m \hat{c}^{\sigma}_m u_{nlm}(\mathbf{r}), \quad (2.20)$$

Leading to

$$\hat{V}_{\text{ee}} = \frac{1}{2} \sum_{\sigma,\sigma'} \sum_{\{m\}} \langle m, m''|V_{\text{ee}}|m', m'''\rangle \hat{c}^{\dagger\sigma'}_{m''} \hat{c}^{\dagger\sigma}_m \hat{c}^{\sigma}_{m'} \hat{c}^{\sigma'}_{m'''}. \quad (2.21)$$

Defining now $n^{\sigma}_{mm'} \equiv \langle G|\hat{c}^{\dagger\sigma}_m \hat{c}^{\sigma}_{m'}|G\rangle$ (where $|G\rangle$ is the ground state) one gets for $\sigma' = \sigma$

$$\langle G|\hat{c}^{\dagger\sigma}_{m''} \hat{c}^{\dagger\sigma}_m \hat{c}^{\sigma}_{m'} \hat{c}^{\sigma}_{m'''}|G\rangle \approx n^{\sigma}_{mm'} n^{\sigma}_{m''m'''} - n^{\sigma}_{mm'''} n^{\sigma}_{m''m'}, \quad (2.22)$$

and for $\sigma' = -\sigma$

$$\langle G|\hat{c}^{\dagger-\sigma}_{m''} \hat{c}^{\dagger\sigma}_m \hat{c}^{\sigma}_{m'} \hat{c}^{-\sigma}_{m'''}|G\rangle \approx n^{\sigma}_{mm'} n^{-\sigma}_{m''m'''}. \quad (2.23)$$

This leads to the expression (2.18). Basically, we have the same LDA+U theory as before (see e.g. Eq. (2.14)), only now $\langle m, m''|V_{\text{ee}}|m', m'''\rangle$ plays the role of U, and $\langle m, m''|V_{\text{ee}}|m''', m'\rangle$ plays the role of J. The double-counting term will have the same form as before,

$$E_{\text{dc}}[\{n\}] = \frac{1}{2}UN(N-1) - \frac{1}{2}J\left[N^{\uparrow}(N^{\uparrow}-1) + N^{\downarrow}(N^{\downarrow}-1) \right], \quad (2.24)$$

where $N = N^\uparrow + N^\downarrow$ and $N^\sigma = \text{Tr}(n^\sigma_{mm'})$. Note that if density matrix is diagonal, $n^\sigma_{mm'} = n^\sigma \delta_{mm'}$, then we get back (2.15).

Now let's establish a proper relationship between $\langle m, m''|V_{\text{ee}}|m', m'''\rangle$, $\langle m, m''|V_{\text{ee}}|m''', m'\rangle$, U and J. Let's write explicitly

$$\langle m, m''|V_{\text{ee}}|m', m'''\rangle = \int d^3r \int d^3r' u^*_{nlm}(\mathbf{r})u^*_{nlm''}(\mathbf{r}')V_{\text{ee}}(\mathbf{r} - \mathbf{r}')u_{nlm'}(\mathbf{r}')u_{nlm'''}(\mathbf{r}). \quad (2.25)$$

For the *unscreened* Coulomb interaction, one can use the addition theorem for spherical harmonics to expand

$$\frac{1}{|\mathbf{r} - \mathbf{r}'|} = \sum_{l=0}^{\infty} \sum_{m=-l}^{l} \frac{r_<^l}{r_>^{l+1}} \frac{4\pi}{2l+1} Y^*_{lm}(\theta_>, \phi_>)Y_{lm}(\theta_<, \phi_<), \quad (2.26)$$

where $r_<$ ($r_>$) is the lesser (greater) of r and r'. Then separating integrals of products of spherical harmonics and radial parts we can write

$$\langle m, m''|V_{\text{ee}}|m', m'''\rangle = \sum_k a_k(m, m', m'', m''')F^k, \quad (2.27)$$

where

$$a_k(m, m', m'', m''') = \frac{4\pi}{2k+1} \sum_{q=-k}^{k} \langle lm|Y_{kq}|lm'\rangle\langle lm''|Y^*_{kq}|lm'''\rangle, \quad (2.28)$$

and F^k are the corresponding integrals over r and r' (Slater integrals [26]). It is known that integrals of triple products of spherical harmonics can be written in terms of Clebsch-Gordan coefficients or Wigner's $3 - j$ symbols [27]. Using their properties one can show [20] that for d electrons ($l = 2$) only F^0, F^2 and F^4 are needed.

Although F^k are introduced for the unscreened Coulomb interaction, we will assume that the same procedure is valid for the screened interaction, and in our case F^k will include effects of screening by all electronic states except the states in the open d (or f) shell.

A calculation of the averages similar to (2.16) yields [25] the relations

$$U = F^0,$$

$$J = (F^2 + F^4)/14$$

(2.29)

between U, J, and F^k values. For most transition metals, the ratio $F^4/F^2 \approx 0.625$ [28]. In DFT code packages, the LDA+U is usually implemented in this form, that is, Eq. (2.16) with the terms $E_U[\{n\}]$ and $E_{\mathrm{dc}}[\{n\}]$ given by (2.17) and (2.24) respectively, and matrix elements given by (2.27-2.29).

2.2.4 Simplified version of LDA+U

As was mentioned, in the derivation of the LDA+U functional in the previous section we took into account the nonsphericity of the Coulomb interaction. In many cases, this leads to small corrections that can be neglected. Then one can start directly from Eq. (2.14), keeping in mind that U and J are now spherically-averaged matrix elements of the screened Coulomb interaction. If one plugs into this expression $N = \sum_{m,\sigma} n_{m\sigma}$ and $N^\sigma = \sum_m n_{m\sigma}$, then the functional takes a very simple form [29]

$$E_{\mathrm{LDA}+U} = E_{\mathrm{LDA}} + \frac{U-J}{2} \sum_{m,\sigma} \left[n_{m\sigma} - n_{m\sigma}^2 \right].$$

(2.30)

One can also write the rotationally invariant analogue of the above expression as

$$E_{\mathrm{LDA}+U} = E_{\mathrm{LDA}} + \frac{U-J}{2} \sum_{\sigma} \left[\mathrm{Tr}(n^\sigma) - \mathrm{Tr}(n^\sigma n^\sigma) \right].$$

(2.31)

This is another form of the LDA+U method widely used in practical calculations. Note that in this case the functional depends only on one parameter $(U-J)$.

2.3 Noncollinear magnetism

Before discussing approaches to noncollinear magnetism in DFT, we quickly review the local spin-density approximation (LSDA) used for spin-polarized calculations. Because up and down electrons are treated separately in the LSDA, it opens the possibility for studying magnetic systems.

How does one generalize the LDA to the spin-polarized case? The straightforward way is to assume the total energy to be a functional of two densities, for up and down spins. Then for each spin channel there will be a separate effective Kohn-Sham potential

$$V_{\text{KS}}^{\alpha}(\mathbf{r}) = V_{\text{ext}}(\mathbf{r}) + \frac{\delta E_{\text{H}}[n^{\uparrow}, n^{\downarrow}]}{\delta n^{\alpha}(\mathbf{r})} + \frac{\delta E_{\text{XC}}[n^{\uparrow}, n^{\downarrow}]}{\delta n^{\alpha}(\mathbf{r})}, \tag{2.32}$$

where α can be either $\uparrow$ or $\downarrow$. The Hartree energy can be immediately written from Eq. (2.2), where one should put $n(\mathbf{r}) = n^{\uparrow}(\mathbf{r}) + n^{\downarrow}(\mathbf{r})$. Since the exchange energy E_{X} is the sum of contributions from both channels (up and down spins), it is straightforward to write the expression for it in terms of the LDA unpolarized functional

$$E_{\text{X}}[n^{\uparrow}, n^{\downarrow}] = \frac{1}{2} \left\{ E_{\text{X}}^{\text{unpol}}[2n^{\uparrow}] + E_{\text{X}}^{\text{unpol}}[2n^{\downarrow}] \right\}. \tag{2.33}$$

The correlation energy is more complicated and cannot be written as a sum of two separate contributions from up and down spins. The parametrization for the correlation energy is extracted from quantum Monte-Carlo (QMC) simulations or many-body techniques applied to the uniform spin-polarized electron gas. Thus, there exist well-known expressions for the correlation energy in LSDA [30–32].

Von Barth and Hedin [31] proposed a formal justification of the spin-polarized density functional theory. They suggested to introduce a (2×2) density matrix $n^{\alpha\beta}(\mathbf{r})$, and replaced the scalar external potential $V_{\text{ext}}(\mathbf{r})$ by $V_{\text{ext}}^{\alpha\beta}(\mathbf{r})$. They showed that in this case there is no one-to-one correspondence between $V_{\text{ext}}^{\alpha\beta}(\mathbf{r})$ and $n^{\alpha\beta}(\mathbf{r})$ (unlike in the non-polarized case), but nevertheless any ground state property is a functional of $n^{\alpha\beta}(\mathbf{r})$. In this formulation, the exchange-correlation potential is given

by

$$V_{\text{XC}}^{\alpha\beta}(\mathbf{r}) = \frac{\delta E_{\text{XC}}}{\delta n^{\alpha\beta}(\mathbf{r})}. \tag{2.34}$$

Then dividing the system into small boxes, one can assume that in each box the exchange-correlation energy density is given by the expression for a homogeneous spin-polarized electron gas, $\epsilon_{\text{XC}}(n^{\uparrow}, n^{\downarrow})$, where now $n^{\uparrow}(\mathbf{r})$ and $n^{\downarrow}(\mathbf{r})$ are eigenvalues of the density matrix $n^{\alpha\beta}(\mathbf{r})$:

$$E_{\text{XC}}[\{n^{\alpha\beta}(\mathbf{r})\}] = \int d^3 r \left\{ n^{\uparrow}(\mathbf{r}) + n^{\downarrow}(\mathbf{r}) \right\} \epsilon_{\text{XC}}(n^{\uparrow}, n^{\downarrow}). \tag{2.35}$$

Here the labels $\uparrow$ and $\downarrow$ refer to a local spin quantization axis given by $\sum_{\alpha,\beta} \boldsymbol{\sigma}^{\beta\alpha} n^{\alpha\beta}$, where $\boldsymbol{\sigma} = (\sigma_x, \sigma_y, \sigma_z)$ are Pauli matrices. This leads to the expression

$$V_{\text{XC}}^{\alpha}(\mathbf{r}) = \frac{\partial}{\partial n^{\alpha}(\mathbf{r})} \left[\left\{ n^{\uparrow}(\mathbf{r}) + n^{\downarrow}(\mathbf{r}) \right\} \epsilon_{\text{XC}}(n^{\uparrow}, n^{\downarrow}) \right] \tag{2.36}$$

for the exchange-correlation potential.

Note that von Barth and Hedin used the density matrix as a stepping stone to arrive at the LSDA theory. In the end, the functional depends on $n^{\uparrow}$ and $n^{\downarrow}$. However, their formalism is naturally fit to the description of systems with noncollinear spins. Kübler *et al.* [33] were among the first to realize this idea by allowing the spin-quantization axis to change throughout the system. Basically, they still used the LSDA functional which depended on $n^{\uparrow}$ and $n^{\downarrow}$, but the quantization axis was allowed to vary in space. More specifically, they suggested to calculate the density matrix at each position, diagonalize it, and use Eq. (2.36) for the exchange-correlation potential at this point. (For simplicity, they used the atomic sphere approximation, assuming that the spin-quantization axis does not change within some sphere centered on an atom.)

An equivalent way of treating noncollinear magnetism is to vary the energy functional with respect to the whole density matrix $n^{\alpha\beta}(\mathbf{r})$ and to use four exchange-correlation potentials $V_{\text{XC}}^{\alpha\beta}(\mathbf{r})$

as in the original formalism of von Barth and Hedin. Then there is no need to consider local spin-quantization axes. In this case, the exchange-correlation functional is given by

$$E_{\mathrm{XC}}[\{n^{\alpha\beta}\}] = \int d^3r\, n_0(\mathbf{r})\epsilon_{\mathrm{XC}}(\{n^{\alpha\beta}(\mathbf{r})\}). \tag{2.37}$$

We note that $n_0(\mathbf{r}) = \mathrm{Tr}(n) \equiv \sum_\alpha n^{\alpha\alpha}$ is the usual electron density; the index 0 was added to distinguish it from the density matrix in this discussion. Any (2×2) matrix can be decomposed into the set of identity and Pauli matrices. Therefore, we can write

$$n^{\alpha\beta}(\mathbf{r}) = \frac{1}{2}\left[n_0(\mathbf{r})\delta_{\alpha\beta} + \mathbf{m}(\mathbf{r}) \cdot \boldsymbol{\sigma}^{\alpha\beta}\right]. \tag{2.38}$$

One can easily check by taking a trace of this expression that indeed $n_0(\mathbf{r}) = \mathrm{Tr}(n)$. Also, multiplying this expression by each of the Pauli matrices and taking a trace, one can find that

$$\mathbf{m}(\mathbf{r}) = \mathrm{Tr}[n(\mathbf{r})\boldsymbol{\sigma}] = \sum_{\alpha,\beta} n^{\alpha\beta}(\mathbf{r})\boldsymbol{\sigma}^{\beta\alpha}. \tag{2.39}$$

So the functional of the exchange-correlation energy can be written as

$$E_{\mathrm{XC}}[n_0(\mathbf{r}), \mathbf{m}(\mathbf{r})] = \int d^3r\, n_0(\mathbf{r})\epsilon_{\mathrm{XC}}(n_0(\mathbf{r}), \mathbf{m}(\mathbf{r})). \tag{2.40}$$

However, for the homogeneous electron gas the energy density ϵ_{XC} does not depend on the direction of the magnetic moment, i.e. $\epsilon_{\mathrm{XC}}(n_0, \mathbf{m}) = \epsilon_{\mathrm{XC}}(n_0, m)$. This means that in case of noncollinear magnetism, we can use the same parametrization as in the LSDA for the exchange-correlation energy density, but using $n^\uparrow = \frac{1}{2}(n_0 + m)$ and $n^\downarrow = \frac{1}{2}(n_0 - m)$.

2.4 Relativistic effects and spin-orbit interaction

In Chapter 4, the electric polarization induced by non-collinear magnetic order in $TbMnO_3$ will be studied. As we discuss later, this effect is believed to be mostly due to the inverse Dzyaloshinskii-Moriya interaction, which is one of the consequences of the spin-orbit interaction. Therefore, it is important to include spin-orbit coupling in DFT calculations. This section describes how this is done in principle; the practical implementations vary from code to code.

2.4.1 General considerations

For a proper treatment of relativistic effects, instead of the Schrödinger equation one has to solve the Dirac equation [34, 35]

$$i\hbar \frac{\partial}{\partial t} \Psi = (c\boldsymbol{\alpha} \cdot \mathbf{p} + \beta mc^2)\Psi. \tag{2.41}$$

Here Ψ is a four-component spinor, and $\boldsymbol{\alpha}$ and β are (4×4) matrices which can be written in terms of Pauli matrices and (2×2) identity matrix $\mathbf{1}$ as

$$\boldsymbol{\alpha} = \begin{pmatrix} 0 & \boldsymbol{\sigma} \\ \boldsymbol{\sigma} & 0 \end{pmatrix}, \qquad \beta = \begin{pmatrix} \mathbf{1} & 0 \\ 0 & -\mathbf{1} \end{pmatrix}. \tag{2.42}$$

It is convenient to measure energies relative to the rest-mass energy of the electron:

$$H = c\boldsymbol{\alpha} \cdot \mathbf{p} + (\beta - 1)mc^2 + V(\mathbf{r}), \tag{2.43}$$

where we also added the external potential. Since the relativistic effects are only significant close to the nucleus, it is safe to assume the potential $V(\mathbf{r})$ to be spherically symmetric. In this case, the stationary solution can be shown to have the form [36]

$$\Psi^l_{njm} = \begin{bmatrix} g^l_{nj}(r)\phi^l_{jm} \\ if^l_{nj}(r)\frac{\boldsymbol{\sigma} \cdot \mathbf{r}}{r}\phi^l_{jm} \end{bmatrix}, \tag{2.44}$$

where ϕ_{jm}^l are two-component spinors which are relativistic equivalents of the usual spherical harmonics. We will drop the index n from now on. The dependence of the radial functions $g_j^l(r)$ and $f_j^l(r)$ on quantum numbers l and j can be written in terms of a quantum number k defined as

$$k = \begin{cases} l & \text{if } j = l - \frac{1}{2}, \\ -(l+1) & \text{if } j = l + \frac{1}{2}. \end{cases} \tag{2.45}$$

Then, as follows from the Dirac equation [37], the radial functions $g_k(r)$ and $f_k(r)$ must satisfy equations

$$\frac{df_k(r)}{dr} = \frac{1}{\hbar c}(V(r) - E)g_k(r) + \left(\frac{k-1}{r}\right)f_k(r),$$
$$\frac{dg_k(r)}{dr} = -\left(\frac{k+1}{r}\right)g_k(r) + \frac{2}{\hbar}M(r)cf_k(r). \tag{2.46}$$

Here $M(r)$ is an effective mass which now depends on r:

$$M(r) \equiv m + \frac{1}{2c^2}(E - V(r)). \tag{2.47}$$

Eliminating $f_k(r)$ from equations (2.46), one gets the following differential equation for $g_k(r)$:

$$\left(\frac{-\hbar^2}{2M}\right)\left[g_k'' + \frac{2}{r}g_k' - \frac{l(l+1)}{r^2}g_k\right] - \frac{V'g_k'\hbar^2}{4M^2c^2} - \frac{k+1}{r}\frac{V'g_k\hbar^2}{4M^2c^2} = (E - V)g_k. \tag{2.48}$$

The function f_k can then be found using the second equation in (2.46). These radial functions must also satisfy the normalization condition

$$\int (g_k^2 + f_k^2)r^2 dr = 1. \tag{2.49}$$

Equation (2.48) looks like the Schrödinger equation except that the mass $M(\mathbf{r})$ is a function of radius, and there are two additional terms. These terms are the last two terms on the left hand side of the equation, which can be identified as the Darwin term and the spin-orbit coupling term,

respectively. Using the relation

$$\mathbf{L} \cdot \boldsymbol{\sigma} \phi_{km} = -\hbar(k+1)\phi_{km}, \tag{2.50}$$

one can rewrite the spin-orbit coupling as an operator in a more familiar form

$$H_{\mathrm{SO}} = \frac{\hbar^2}{2M^2c^2} \frac{1}{r} \frac{\partial V}{\partial r} \mathbf{L} \cdot \mathbf{S}, \tag{2.51}$$

where $\mathbf{L}$ is the angular momentum operator and $\mathbf{S}$ is the spin operator.

In practice, when solving the relativistic equation (2.48) the spin-orbit coupling is often assumed to be small and neglected. In this case, Eq. (2.48) is called the *scalar relativistic* equation. Then, if needed, the spin-orbit coupling contribution can be calculated using perturbation theory.

2.4.2 Relativistic effects in the pseudopotential context

In order to solve the Kohn-Sham equations, the electronic wave functions are expanded in a set of basis functions like plane waves or atomic orbitals. Plane-wave basis sets are usually used in solid state physics because they are well suited for problems with periodic boundary conditions. They also have an advantage that the precision of the calculations is controlled by the number of plane waves in the basis. However, there are shortcomings too. Because the Kohn-Sham wave functions oscillate rapidly in the vicinity of the nuclei, their expansion into plane waves requires very large basis sets, which makes the calculations very inefficient. There are several ways to avoid this problem, most common being the use of the pseudopotential and projector augmented wave (PAW) [38] methods. In the pseudopotential approach, the bare Coulomb potentials of the nuclei that make the external potential are replaced with effective potentials that effective potentials are constructed in such a way that the chemically active valence electrons are described by nodeless pseudo wave functions. At the same time, the less important core electrons are built into the pseudopotentials. When constructing the pseudopotential, one makes sure that the eigenenergies and scattering properties are reproduced. Modern pseudopotential calculations are usually based on norm-conserving [39] or ultrasoft [40]

pseudopotentials.

Since the relativistic effects discussed in this section have their origin deep in the core, one can incorporate them into the pseudopotentials. This is done by generating two pseudopotentials for each $l > 0$, one for $j = l + 1/2$ and one for $j = l - 1/2$ (only one pseudopotential is constructed for $l = 0$). The pseudopotentials are generated in two steps. First, one solves the fully-relativistic Eq. (2.48) for a single atom by doing an all-electron calculation. Then, for each j, one searches for a pseudopotential V_j such that the Schrödinger equation with this V_j has solutions having the same eigenvalues and the same wavefunction tails beyond some cut-off radii as solutions of Eq. (2.48). Having pseudopotentials generated, one can then define the averaged pseudopotential

$$V_l = \frac{1}{2l + 1} \left[(l + 1)V_{l+1/2} + lV_{l-1/2} \right].$$ (2.52)

This weighted averaging procedure done on Eq. (2.48) results in omitting the spin-orbit coupling term. Therefore, the pseudopotential V_l will incorporate only the scalar relativistic effects (the mass shift and the Darwin term). One also defines

$$\delta V_l^{\text{SO}} = \frac{2}{2l + 1} \left[V_{l+1/2} - V_{l-1/2} \right],$$ (2.53)

which stores information about the spin-orbit coupling.

Now one can do the usual Kohn-Sham calculations using the above pseudopotentials V_l, and the scalar relativistic effects for the core electrons will automatically be taken into account. In order to include the spin-orbit coupling, one has to add a term to the Hamiltonian [41]:

$$H_{\text{SO}} = \sum_l |l\rangle \delta V_l^{\text{SO}}(r) \mathbf{L} \cdot \mathbf{S} \langle l|.$$ (2.54)

It is important to emphasize that once the relativistic effects are incorporated in the pseudopotentials, one can then solve the non-relativistic Kohn-Sham equations. This approach is implemented in many code packages, e.g., in ABINIT [42] and QUANTUM-ESPRESSO [43].

2.4.3 Relativistic effects in the context of the PAW method

The PAW method [38] is a general formulation of DFT in which the pseudo wave functions are mapped onto the Kohn-Sham wave functions by a linear transformation. The wave functions are divided into parts residing in the atom-centered sphere (augmentation region Ω_R) and in the region outside the sphere. The all-electron (AE) and pseudo (PS) wave functions coincide outside the augmentation region. Within Ω_R the wave functions are expanded into partial waves as

$$
\begin{aligned}
|\tilde{\Psi}\rangle &= \sum_i c_i |\tilde{\phi}_i\rangle, \\
|\Psi\rangle &= \sum_i c_i |\phi_i\rangle,
\end{aligned}
\tag{2.55}
$$

where tilde denotes PS wave functions. The coefficients c_i are the same in the both expansions, which means that partial waves ϕ_i and $\tilde{\phi}_i$ are related by the same transformation as Ψ and $\tilde{\Psi}$. The linearity of the transformation implies that c_i can be written as

$$
c_i = \langle \tilde{p}_i | \tilde{\Psi} \rangle,
\tag{2.56}
$$

with the set of projector functions $\tilde{p}_i$ satisfying the orthogonality condition

$$
\langle \tilde{p}_i | \tilde{\phi}_j \rangle = \delta_{ij}.
\tag{2.57}
$$

Now the transformation from the PS to AE wave function can be written as

$$
|\Psi\rangle = |\tilde{\Psi}\rangle + \sum_i \left(|\phi_i\rangle - |\tilde{\phi}_i\rangle \right) \langle \tilde{p}_i | \tilde{\Psi} \rangle = \hat{\tau} |\tilde{\Psi}\rangle.
\tag{2.58}
$$

The PS version of any operator $\hat{A}$ is then simply $\tilde{A} = \hat{\tau}^\dagger \hat{A} \hat{\tau}$. The PS version of the identity operator becomes the overlap operator

$$
\tilde{S} = \mathbf{1} + \sum_{i,j} |\tilde{p}_i\rangle \left[\langle \phi_i | \phi_j \rangle - \langle \tilde{\phi}_i | \tilde{\phi}_j \rangle \right] \langle \tilde{p}_j |.
\tag{2.59}
$$

Then instead of the Schrödinger (or scalar relativistic) equation, one has to solve the generalized eigenvalue equation

$$\tilde{H}|\tilde{\Psi}_n\rangle = \epsilon_n \tilde{S}|\tilde{\Psi}_n\rangle. \tag{2.60}$$

The explicit form of the Hamiltonian can be found in Ref. [38] or Ref. [44].

In order to treat the spin-orbit interaction in the PAW formalism, one has to add the PS version of H^{SO} given by Eq. (2.51). Usually, in this case one makes several approximations. First, the spin-orbit operator is added only in the augmentation region, which is justified because the spin-orbit effect dominates in the region close to the nuclei. And second, only the spherically symmetric part (or $l = 0$) of the effective potential $V(\mathbf{r})$ is put in the spin-orbit part of the Hamiltonian. This way it is implemented in the VASP code package [45].

2.5   Berry-phase polarization

In this section the modern theory of polarization developed by King-Smith, Vanderbilt and Resta [46, 47] will be discussed. As was already mentioned in the introduction, the simple definition given by Eq. (1.2) is not suited for the definition of the local polarization at each point in the material, because the limit $V \rightarrow 0$ is not well-defined. Moreover, even for the averaged polarization where the integral is taken over some finite volume element V, the above definition fails for infinite periodic crystals. Indeed, in this case the value of polarization will depend on the choice of the unit cell V. The modern theory of polarization overcomes these troubles and gives a definition of the polarization closely connected to the way it is measured experimentally. Also, the formalism of the modern theory of polarization is readily adapted to DFT calculations. The discussion below closely follows Ref. [5].

The modern theory is based on the argument that polarization $\mathbf{P}$ itself cannot be defined, because only the *difference* in polarization $\Delta\mathbf{P}$ that occurs during some physical process has physical meaning. The situation is analogous to the measurement of the energy of some system: one does not measure the value of the energy itself but rather the difference in energies of the final and initial

states. Therefore, the proper definition of the change in polarization would be

$$\Delta\mathbf{P} = \int dt \frac{1}{V} \int_V d\mathbf{r}\, \mathbf{j}(\mathbf{r}, t), \qquad (2.61)$$

where $\mathbf{j}(\mathbf{r}, t)$ is the electric current density in the sample during some physical process and V is a unit cell of the crystal. One can then consider a more general situation, where polarization depends on some parameter λ that changes adiabatically during some process, and write

$$\Delta\mathbf{P} = \int_0^1 d\lambda \frac{d\mathbf{P}}{d\lambda}. \qquad (2.62)$$

Although now we do not assign any meaning to the polarization $\mathbf{P}$ at any particular λ, one can ask how to relate this definition to the experimentally measured polarization. If, for example, the state with $\lambda = 0$ corresponds to the crystal having inversion symmetry, then one can say that this crystal has zero polarization ($\mathbf{P}_{\lambda=0}^{\mathrm{eff}} = 0$). Now one can define the spontaneous polarization as

$$\mathbf{P}_{\mathrm{sp}} = \int_0^1 d\lambda \frac{d\mathbf{P}}{d\lambda}, \qquad (2.63)$$

where $\lambda = 1$ corresponds to the polarized state of interest. Thus, if one wants to make a connection of the theory with experiment, one needs to consider some reference structure, and then calculate the difference of polarization between the given structure and the reference structure.

From now on we will focus on periodic systems for which Bloch's theorem is valid. In this case the eigenfunctions of the Hamiltonian will have the form

$$\psi_{n\mathbf{k}}(\mathbf{r}) = e^{i\mathbf{k}\cdot\mathbf{r}} u_{n\mathbf{k}}(\mathbf{r}), \qquad (2.64)$$

where $u_{n\mathbf{k}}(\mathbf{r})$ has the periodicity of the lattice. One can rewrite the Schrödinger equation as

$$H_{\mathbf{k}}|u_{n\mathbf{k}}\rangle = E_{n\mathbf{k}}|u_{n\mathbf{k}}\rangle \qquad (2.65)$$

with

$$H_{\mathbf{k}} = \frac{(\mathbf{p} + \hbar\mathbf{k})^2}{2m} + V. \tag{2.66}$$

For simplicity we assume that there are no band degeneracies, and we do not consider spin. The Hamiltonian depends on λ which varies adiabatically, so one can use adiabatic perturbation theory to find the change in the eigenstate to first order:

$$|\delta\psi_{n\mathbf{k}}\rangle = -i\hbar\frac{d\lambda}{dt}\sum_{m\neq n}\frac{\langle\psi_{m\mathbf{k}}|\partial_\lambda\psi_{n\mathbf{k}}\rangle}{E_{n\mathbf{k}} - E_{m\mathbf{k}}}|\psi_{m\mathbf{k}}\rangle. \tag{2.67}$$

Then the contribution to the electric current from band n will be given by

$$\mathbf{j}_n = \frac{d\mathbf{P}_n}{dt} = \frac{i\hbar e}{(2\pi)^3 m}\frac{d\lambda}{dt}\sum_{m\neq n}\int d\mathbf{k}\frac{\langle\psi_{n\mathbf{k}}|\mathbf{p}|\psi_{m\mathbf{k}}\rangle\langle\psi_{m\mathbf{k}}|\partial_\lambda\psi_{n\mathbf{k}}\rangle}{E_{n\mathbf{k}} - E_{m\mathbf{k}}} + \text{c.c.} \tag{2.68}$$

This result can be further simplified [5] to

$$\frac{d\mathbf{P}_n}{d\lambda} = \frac{ie}{(2\pi)^3}\int d\mathbf{k}\langle\nabla_{\mathbf{k}}u_{n\mathbf{k}}|\partial_\lambda u_{n\mathbf{k}}\rangle + \text{c.c.} \tag{2.69}$$

Now the total change in the polarization can be written as

$$\Delta\mathbf{P} = \Delta\mathbf{P}_{\text{ion}} + \Delta\mathbf{P}_{\text{el}}, \tag{2.70}$$

where the ionic contribution comes from the displacements of the nuclei and the electronic contribution is found by integrating Eq. (2.69) and summing over all bands n. In the end one can *formally* define the total polarization as

$$\mathbf{P} = \mathbf{P}_{\text{el}} + \mathbf{P}_{\text{ion}} = \frac{e}{(2\pi)^3}\text{Im}\sum_n\int d\mathbf{k}\langle u_{n\mathbf{k}}|\nabla_{\mathbf{k}}|u_{n\mathbf{k}}\rangle + \frac{e}{\Omega}\sum_s Z_s^{\text{ion}}\mathbf{r}_s. \tag{2.71}$$

The sum in the ionic contribution is taken over all nuclei in the unit cell. It should be emphasized that this is a formal definition. Calculation of the polarization by the above formula will not in general

correspond to the polarization measured in the experiment, but the change in the polarization will.

The integral in the expression for $\mathbf{P}_{el}$ is known as the Berry phase. That is why the theory is often referred to as the Berry-phase polarization theory. An important consequence of this derivation is that the polarization turns out to be defined only modulo some quantum, because the Berry phase itself is defined only modulo 2π. A simple calculation shows that the quantum of polarization is given by $e\mathbf{R}/\Omega$, where $\mathbf{R}$ is any lattice vector. This is not a problem in practice, because when one calculates changes in polarization the quantum cancels out.

Chapter 3

Polarization properties of $Zn_{1-x}Mg_xO$ alloys

3.1 Introduction

Recently, much attention has been paid to wurtzite $Zn_{1-x}Mg_xO$ alloys as candidates for applications in optoelectronic devices in the blue and ultraviolet region. ZnO is a wide-band-gap semiconductor with a direct gap of $\sim$3.3 eV. The band gap becomes even larger if Zn atoms are substituted by Mg atoms, which have a similar ionic radius, allowing the construction of quantum-well and superlattice devices [48]. Similar behavior is well known for the zincblende GaAs/Al_xGa_{1-x}As system and is the basis of much of modern optoelectronics [49]. Recent trends have led in the direction of fabricating similar structures in wide-gap semiconductor systems such as wurtzite III-V nitrides [50] and in $Zn_{1-x}Mg_xO$ [48, 51, 52]. There has also been recent interest in other kinds of nanostructures based on the ZnO and $Zn_{1-x}Mg_xO$ materials systems [53–56].

Pure ZnO prefers the wurtzite crystal structure, while MgO adopts the cubic rocksalt structure. Substitution of Zn by Mg results in a metastable wurtzite alloy for certain magnesium concentrations. Experimental reports concerning the growth of these alloys on sapphire substrates indicate that Mg concentrations up to $\sim$30% [48, 52], or even $\sim$50% [57], can be achieved.

Many *ab-initio* calculations of the properties of the parent compounds MgO and ZnO have appeared in the literature [58–61]. The properties of ternary $Zn_{1-x}Mg_xO$ alloys have been less well studied. There have been calculations of the dependence of the band structure and band gap on concentration x [62]. Regarding the question of crystal structure and stability, Kim *et al.* have shown that the wurtzite $Zn_{1-x}Mg_xO$ alloy is stable with respect to the corresponding rocksalt alloy for $x < 0.375$ [63]. Similar results were obtained by Sanati *et al.* but for $x < 0.33$ [64]. However, Sanati *et al.* also have shown that $Zn_{1-x}Mg_xO$ is unstable with respect to phase separation into wurtzite ZnO and rocksalt MgO phases even for low x values. This means that $Zn_{1-x}Mg_xO$ alloys

are not thermodynamically stable, consistent with a rather low observed solid solubility limit for Mg in ZnO [65]. The success in fabricating samples with higher concentrations indicates that the phase separation is kinetically limited, i.e., the time scale required for the alloy to phase segregate into the two lower-energy constituents is long compared to the growth time at the growth temperature.

To our knowledge, there have not been any previous calculations of the the polarization properties in the $Zn_{1-x}Mg_xO$ system. This is an important property to study, since if an interface occurs between a ZnO region and a $Zn_{1-x}Mg_xO$ region within a superlattice or quantum-well structure, bound charges are expected to appear at the interface. These charges, in turn, will create electric fields that are likely to affect the electrical and optical properties of the quantum-well devices. In the present work, therefore, we have undertaken a study of the polarization and piezoelectric properties of $Zn_{1-x}Mg_xO$ [1].

The structure of the chapter is as follows. In the next section we describe the computational methods used in our work. In Sec. 3.3 we introduce the six supercell structures that were constructed and used as the structural models for the alloys of interest. Then, in Sec. 3.4, we report the main results of this work. Finally, a brief summary is given in Sec. 3.5.

3.2   Computational methods

Calculations of structural and polarization properties are carried out using a plane-wave pseudopotential approach to density-functional theory (DFT). We use the ABINIT code package [42] with the local-density approximation (LDA) implemented using the Teter parametrization of the exchange-correlation [66] and with Troullier-Martins pseudopotentials [67]. For the Zn pseudopotential the $3d$ valence electrons are included in the valence, as their presence has a significant effect on the accuracy of the results [68]. A plane-wave basis set with an energy cutoff of 120 Ry is used to expand the electronic wave functions. A $6 \times 6 \times 4$ Brillouin-zone k-point sampling is used for pure wurtzite ZnO, and equivalent k-point meshes are constructed for use in all wurtzite supercell calculations. The electric polarization is calculated using the Berry-phase approach [46].

3.3   Supercell structures

In the present work we study the properties of six different models of the ternary $Zn_{1-x}Mg_xO$ alloy, to be described shortly. However, first consider pure wurtzite ZnO. It can be viewed as two identical hexagonal closed-packed (*hcp*) lattices; we take the O sublattice to be shifted in the $+\hat{z}$ direction relative to the Zn sublattice. Three parameters determine this structure: a and c are the lattice constants of the *hcp* lattice, and u describes the shift between the two sublattices.

Replacing some of the Zn atoms by Mg atoms, we get a ternary $Zn_{1-x}Mg_xO$ alloy. Of course, the real alloy is highly disordered. In order to carry out calculations using periodic boundary conditions, we construct ordered supercells having the same Mg concentration x as the alloy of interest. By comparing properties of different supercells having the same x, we may obtain a rough estimate of the size of the errors that result from the replacement of the true disordered alloy by an idealized supercell model.

When constructing supercells, we restricted ourselves to structures having hexagonal symmetry about the z-axis, since real $Zn_{1-x}Mg_xO$ alloys have this symmetry on average. This makes the calculation and interpretation of the results easier. We constructed six model alloy structures: one for $x = 1/6$ (Model 1), two for $x = 1/4$ (Models 2 and 3), one for $x = 1/3$ (Model 4) and two for $x = 1/2$ (Models 5 and 6), as follows.

The simplest alloy one can make (Model 5) is obtained by replacing the Zn atoms by Mg atoms in every second Zn layer along z, giving a structure with Mg concentration $x = 1/2$ and retaining the primitive periodicity of pure ZnO (four atoms per cell). Similarly, if one replaces every fourth layer of Zn by Mg, one arrives a model with $x = 1/4$ (Model 2); this has an eight-atom supercell with the primitive 1×1 in-plane periodicity but with a doubled periodicity along the z-direction.

In the remaining models, we retain the primitive periodicity along z but expand the size of the supercell in the x-y plane, as illustrated in Fig. 3.1. Models having 2×2 in-plane periodicity (Models 3 and 6) are specified with reference to Figs. 3.1(a) and (b), and those having $\sqrt{3} \times \sqrt{3}$ periodicity (Models 1 and 4), are shown in Figs. 3.1(c) and (d). Models 3 and 6 thus have 16 atoms
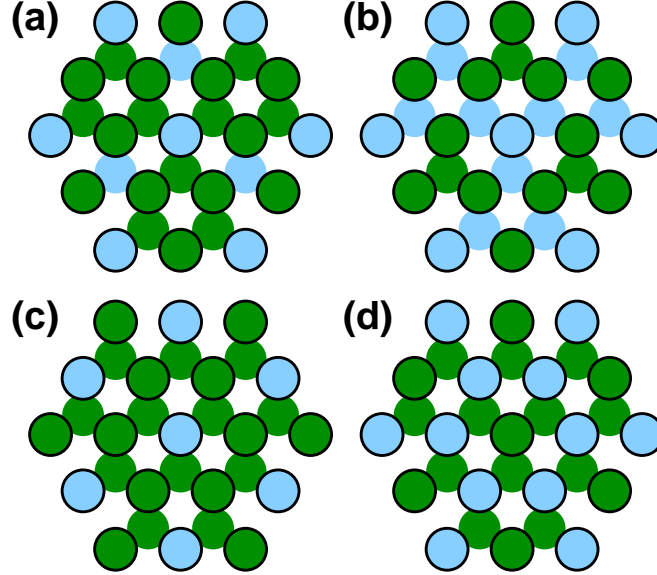
Figure 3.1: Top view of cation layers of supercell models for $Zn_{1-x}Mg_xO$ alloys [1]. Dark-green circles correspond to Zn and light-blue circles correspond to Mg. The black outline over some circles emphasizes that these ions belong to the top layer while the rest of the ions belong to the bottom layer. (a) Structure with 2×2 periodicity and concentration of Mg $x = 1/4$ (Models 3). (b) Structure with 2×2 periodicity and $x = 1/2$ (Models 6). (c) Structure with $\sqrt{3} \times \sqrt{3}$ periodicity and $x = 1/6$ (Models 1). (d) Structure with $\sqrt{3} \times \sqrt{3}$ periodicity and $x = 1/3$ (Models 4).

per supercell, while Models 1 and 4 have 12 atoms. As one can see from the figure, Model 3 is a model with $x = 1/4$ in each cation layer and $x = 1/4$ overall. In Model 6 one has alternating cation layers with $x = 1/4$ and $x = 3/4$, for an overall Mg concentration of $x = 1/2$. Turning to the $\sqrt{3} \times \sqrt{3}$ structures, one can see that the hexagonal symmetry requires that all atoms must be the same in every second layer (see Figs. 3.1(c) and (d)). We construct Model 1 by alternating layers with $x = 0$ and $x = 1/3$ for an average $x = 1/6$. Finally, for Model 4 we alternate layers with $x = 0$ and $x = 2/3$, averaging to $x = 1/3$.

Of course, it would be possible to generate more supercell models of the alloy by expanding the periodicity or reducing the symmetry. However, the six models described above provide a reasonable coverage of concentrations in the range $0 \le x \le 1/2$ with some redundancy (for $x = 1/4$ and $x = 1/2$). We have thus chosen to limit ourselves to these six models in the present work.

3.4 Results

3.4.1 Pure ZnO and MgO

To determine the crystal structures and cell parameters of pure ZnO and MgO, we carried out DFT calculations for both materials in both the wurtzite and rocksalt structures. For wurtzite ZnO we obtained lattice parameters $a = 3.199\,\text{Å}$, $c = 5.167\,\text{Å}$ and $u = 0.379$. While these results are very close to previously reported theoretical values [69], they slightly differ from experimental values [70] ($a = 3.258\,\text{Å}$, $c = 5.220\,\text{Å}$ and $u = 0.382$). The cohesive energy (defined as the energy per formula unit needed to separate the crystal into atoms) is found to be $8.26\,\text{eV}$. Comparing this to the cohesive energy of rocksalt ZnO ($8.03\,\text{eV}$), one may conclude that ZnO prefers the wurtzite structure, in agreement with experiment. For rocksalt MgO we found $a = 4.240\,\text{Å}$ and a cohesive energy of $10.00\,\text{eV}$. We find that if we start with a plausible wurtzite MgO structure with a, c and u similar to that of ZnO, the crystal can monotonically lower its energy along a transformation path in which a increases, c decreases, and u tends toward 1/2 in agreement with the previous results of Ref. [60]. The minimum occurs at $u = 1/2$, which corresponds to the higher-symmetry h-MgO structure [60]. For this structure we obtain $a = 3.527\,\text{Å}$ and $c = 4.213\,\text{Å}$, in good agreement [58, 60] with previous calculations. We find its cohesive energy to be $9.81\,\text{eV}$, consistent with the fact that MgO prefers the rocksalt structure. (For more details concerning the previous theoretical literature on lattice parameters and binding energies, see Ref. [58].)

The main goal of the present work is to study the polarization and piezoelectric properties of $\text{Zn}_{1-x}\text{Mg}_x\text{O}$. We recall (Sec. 2.5) that only changes in polarization have physical meaning. Therefore, the calculated values of polarization are usually reported relative to some reference structure (corresponding to $\lambda = 0$ in Eq. 2.62). In ferroelectrics, one can take as a reference a centrosymmetric structure corresponding to a paraelectric phase (where polarization can be said to be zero from symmetry arguments). In simple cases, such a structure can be obtained by taking the average of the atomic positions in structures with polarizations $\mathbf{P}$ and $-\mathbf{P}$. Wurtzite ZnO (as well as $\text{Zn}_{1-x}\text{Mg}_x\text{O}$)

is not a ferroelectric but a pyroelectric material, which means that one cannot find a physical cen-trosymmetric structure corresponding to $\lambda = 0$. Instead, to find a reference value of polarization, we use an ideal wurtzite ($u = 3/8$) ionic model, where Zn and O atoms are replaced by point charges with values $+2e$ and $-2e$ respectively. One can show that in this model, the polarization is (modulo ec/V)

$$P_{\mathrm{model}} = \frac{1}{2}\frac{ec}{V} = 0.9041\,\mathrm{C/m^2}. \tag{3.1}$$

Actual Berry-phase calculation for the optimized structure (i.e. $u = 0.379$) gave $P' = 0.8719\,\mathrm{C/m^2}$. Thus, we report the value of polarization relative to the reference value as $P = P' - P_{\mathrm{model}} = -0.0322\,\mathrm{C/m^2}$. Note that the Berry phase calculation for $u = 0.375$ gives $0.9015\,\mathrm{C/m^2}$, which is very close to the result obtained with the ionic model. This indicates that the polarization in ZnO comes mostly from the relaxation of u. From now on (unless mentioned otherwise) the values of polarization will be given relative to P_{model}. Note that the value of the spontaneous polarization differs somewhat from the previous theory of Dal Corso *et al.* [59], who reported a polarization of $-0.05\,\mathrm{C/m^2}$ when using the experimental $u = 0.382$; our value becomes much closer to theirs if we also use the experimental u. Since we are primarily interested in *differences* of the polarization with respect to pure ZnO, we do not believe that these small discrepancies are important.

For reference, our calculated piezoelectric coefficients for pure ZnO are found to be $e_{31} = a\partial P_c/\partial a = -0.634\,\mathrm{C/m^2}$ and $e_{33} = c\partial P_c/\partial c = 1.271\,\mathrm{C/m^2}$. The values of piezoelectric coef-ficients are in good agreement with previous theoretical calculations of Wu *et al.* [71] who found $e_{31} = -0.67\,\mathrm{C/m^2}$ and $e_{33} = 1.28\,\mathrm{C/m^2}$ (and who also provide comparisons with other theoretical and experimental results).

3.4.2 Crystal structure and energies of alloys

For each model described in Sec. 3.3, we calculated the *hcp* lattice parameters a and c in the equi-librium state. Since we are interested in properties of $\mathrm{Zn_{1-x}Mg_xO}$ layers that might be grown on a ZnO substrate, we also calculated the lattice parameters for epitaxially strained structures (i.e., a

Table 3.1: Theoretical equilibrium lattice parameters for bulk ZnO and for models of $Zn_{1-x}Mg_xO$ [1]. Subscript 'free' indicates zero-stress elastic boundary conditions, while 'epit' indicates that a is constrained to be identical to that of bulk ZnO (the values in column V are thus identical by construction).

	x	a_{free} (Å)	$(c/a)_{\text{free}}$	a_{epit} (Å)	$(c/a)_{\text{epit}}$
ZnO	0.0	3.199	1.615	3.199	1.615
Model 1	0.17	3.216	1.605	3.199	1.624
Model 2	0.25	3.230	1.593	3.199	1.625
Model 3	0.25	3.225	1.600	3.199	1.628
Model 4	0.33	3.238	1.589	3.199	1.630
Model 5	0.5	3.266	1.564	3.199	1.635
Model 6	0.5	3.256	1.580	3.199	1.640

Table 3.2: Theoretical cohesive and formation energies (eV per formula unit) for bulk ZnO and MgO and for each supercell model [1].

	x	E_{coh}	E_{form}
ZnO	0.0	8.258	0.0
Model 1	0.17	8.496	-0.053
Model 2	0.25	8.602	-0.093
Model 3	0.25	8.612	-0.083
Model 4	0.33	8.729	-0.123
Model 5	0.5	8.955	-0.176
Model 6	0.5	8.958	-0.173
MgO	1.0	10.004	0.0

fixed to that of pure ZnO). The results are given in Tab. 3.1. In both cases, the c/a ratio exhibits an almost linear dependence on x. However, this ratio is found to decrease with x for the fully relaxed structures, while it increases with x when the epitaxial strain condition is enforced. When the cell is allowed to relax, a increases and c/a decreases with magnesium concentration making the lattice parameters closer to the parameters of the h-MgO structure discussed in Sec. 3.4.1. The latter trend is somewhat surprising because the ZnO and MgO are both ionic compounds, and the ionic radius of Mg is slightly less than that of Zn. Perhaps, charge transfer plays some role by making the bonds partially covalent (the covalent radius of Mg is larger than that of Zn).

In Tab. 3.2 we give cohesive and formation energies for each alloy. One can see that in every case the formation energy is negative. Thus, according to our LDA calculations, at zero temperature the $Zn_{1-x}Mg_xO$ alloy is never stable with respect to phase-separated wurtzite ZnO and rocksalt

Table 3.3: Calculated values of total polarizations of $Zn_{1-x}Mg_xO$ alloy models ($10^{-2} \times C/m^2$) [1]. Subscript 'free' indicates zero-stress elastic boundary conditions, while 'epit' indicates that a is constrained to be identical to that of bulk ZnO. Superscript 'est' indicates value estimated by the model of Eq. (3.2).

	x	P_{free}	P_{epit}	$P_{\text{epit}}^{\text{est}}$
ZnO	0.0	−3.22	−3.22	
Model 1	0.17	−4.23	−2.77	−2.79
Model 2	0.25	−5.01	−2.47	−2.47
Model 3	0.25	−4.70	−2.44	−2.50
Model 4	0.33	−5.65	−2.30	−2.39
Model 5	0.5	−7.89	−1.99	−2.22
Model 6	0.5	−6.99	−2.02	−2.25

MgO. (Of course, at $T > 0$ a small solid solubility of Mg in wurtzite ZnO is expected [65].)

3.4.3 Polarization and piezoelectric properties

The results of the calculations of spontaneous polarization are given in Tab. 3.3, both for the fully relaxed and for the epitaxially strained cases. Note that the values of polarization for models having the same x are fairly consistent with one another; the choice of supercell does not significantly affect the overall trend with x, which is reasonably smooth. A linear fit $P(x) = P(\text{ZnO}) + Ax$ yields coefficients of $A_{\text{free}} = (-0.088 \pm 0.009)\,\text{C/m}^2$ and $A_{\text{epit}} = (0.024 \pm 0.002)\,\text{C/m}^2$. The latter value may be of direct interest for experimental studies of epitaxial superlattices and quantum wells.

Thus, with increasing Mg concentration x, the absolute value of the polarization increases for the relaxed structures and decreases for the epitaxial structures with fixed a. This behavior is very similar to what we saw in Sec. 3.4.2 for the c/a ratios, suggesting that the c/a ratio may be a dominant factor in determining the total polarization. Indeed, since $2e_{31} + e_{33} \approx 0$, one expects the polarization to be almost independent of a change in volume (isotropic strain), so that the change of c/a should be the most important strain effect.

In order to study more thoroughly the role of strain and other factors in determining the polarizations of the $Zn_{1-x}Mg_xO$ structures, we first define ΔP_{tot} to be the polarization of the alloy superlattice structure relative to that of pure ZnO. We then decompose ΔP_{tot} into "electronic,"

"ionic," and "piezoelectric" contributions as follows. First, we construct an artificial $Zn_{1-x}Mg_xO$ superlattice structure in which the structural parameters (a, c, and all internal coordinates) are frozen to be those of pure ZnO, and define ΔP_{elec} to be the polarization of this structure relative to that of pure ZnO. Next, we allow only the internal coordinates of the $Zn_{1-x}Mg_xO$ supercell to relax, while continuing to keep a and c frozen at the pure-ZnO values, and let ΔP_{ion} be the polarization change produced by this internal relaxation. Finally, we allow the lattice constants to relax as well, and define ΔP_{piezo} to be the associated change in polarization. Clearly $\Delta P = \Delta P_{\text{elec}} + \Delta P_{\text{ion}} + \Delta P_{\text{piezo}}$.

The results of such a decomposition are given in Tab. 3.4 for both the stress-free and epitaxial-strain cases. For scale, recall that these are changes relative to $P(\text{ZnO}) = -0.0322\,\text{C/m}^2$. The purely electronic and ionic contributions are the same in both cases because of the way ΔP_{ion} and ΔP_{elec} are defined. The purely electronic contributions ΔP_{elec} are quite small, showing a relatively poor correlation with x. The contribution ΔP_{ion} associated with the ionic relaxations is also quite small, although it is typically 2-3 times larger than ΔP_{elec} and shows a clearer trend (becoming more negative with increasing x). In the stress-free case, by far the largest contribution comes from the piezoelectric effect of the strain relaxation, being typically 5-10 times larger than the ionic one. As is seen from the table, the piezoelectric contribution also dominates in the epitaxial-strain case.

This being the case, it seems likely that many of the polarization-related properties of the $Zn_{1-x}Mg_xO$ alloy can be estimated by using a model based on the piezoelectric effect alone. For example, one might hope that $\delta P = P_{\text{epit}} - P_{\text{free}}$, the difference between the epitaxially-constrained and free-stress polarizations at a given x, could be estimated by a linear approximation of the form

$$\delta P = 2e_{31}\frac{a_{\text{epit}} - a_{\text{free}}}{a_{\text{free}}} + e_{33}\frac{c_{\text{epit}} - c_{\text{free}}}{c_{\text{free}}}. \tag{3.2}$$

In fact, we find that this is the case even if we use the piezoelectric constants of bulk ZnO, already obtained in Sec. 3.4.1, in this formula. Using the computed value of P_{free} reported in the third column of Tab. 3.3, together with the constrained a values and epitaxially-relaxed c values given in the last two columns of Tab. 3.1, we report the computed estimates $P_{\text{epit}}^{\text{est}} = P_{\text{free}} + \delta P$ in the last

Table 3.4: Theoretical values of electronic, ionic, piezoelectric and total contributions to polarization ($10^{-2} \times$C/m^2) for each model, relative to bulk ZnO. Superscript 'free' indicates zero-stress elastic boundary conditions, while 'epit' indicates that a is constrained to be identical to that of bulk ZnO.

	x	ΔP_{elec}	ΔP_{ion}	$\Delta P_{\text{piezo}}^{\text{free}}$	$\Delta P_{\text{tot}}^{\text{free}}$	$\Delta P_{\text{piezo}}^{\text{epit}}$	$\Delta P_{\text{tot}}^{\text{epit}}$
ZnO	0.0	0.0	0.0	0.0	0.0	0.0	0.0
Model 1	0.17	0.01	-0.22	-0.81	-1.01	0.65	0.45
Model 2	0.25	0.18	-0.23	-1.75	-1.80	0.80	0.75
Model 3	0.25	0.00	-0.27	-1.22	-1.48	1.05	0.78
Model 4	0.33	0.09	-0.38	-2.14	-2.43	1.21	0.92
Model 5	0.5	0.23	-0.63	-4.27	-4.67	1.63	1.23
Model 6	0.5	-0.19	-0.62	-2.96	-3.77	2.01	1.20

column of Tab. 3.3. The use of the piezoelectric coefficients of pure ZnO is not obviously justified except at small x, but the results show excellent agreement with the computed P_{epit} values in the fourth column even up to $x = 0.5$, where the error is only about 10%. This approximation thus seems to work quite well.

3.5   Summary

We have investigated the polarization-related properties of wurtzite Zn$_{1-x}$Mg$_x$O alloys using calculations based on density-functional theory in the local-density approximation and the Berry-phase approach to calculating electric polarization. In particular, we have studied the dependence of the spontaneous polarization on Mg concentration using six alloy supercell models with hexagonal symmetry, spanning the range of Mg concentration from $x = 1/6$ to $1/2$. We performed these calculations both for free-stress and epitaxial-strain elastic boundary conditions.

Our results indicate a roughly linear dependence of spontaneous polarization on Mg concentration, although the sign of the linear coefficient is opposite in the free-stress and epitaxial-strain cases. In order to understand this behavior in more detail, we decomposed the change in polarization into electronic, lattice-displacement-mediated, and strain-mediated components, and found that the latter component is dominant. This means that the change in polarization is mostly governed by piezoelectric effects connected with the x-dependent changes of the a and c lattice constants.

We further confirmed this picture by showing that the polarization changes could be well approximated by a model in which the only first-principles inputs to the model are the piezoelectric coefficients of pure ZnO and the x-dependence of the equilibrium lattice constants of the $Zn_{1-x}Mg_xO$ alloy. These results suggest that charging effects associated with polarization discontinuities in $ZnO/Zn_{1-x}Mg_xO$ superlattices and quantum wells should be subject to prediction and interpretation in a fairly straightforward manner.

Chapter 4

Improper ferroelectricity in TbMnO$_3$

4.1 Introduction

4.1.1 Multiferroics and magnetoelectrics

In the introduction, we defined a *ferroelectric* as a material having a spontaneous polarization that is switchable under applied electric field. As was mentioned already, this behavior is similar to that of *ferromagnets*, which have a spontaneous magnetization that is switchable under applied magnetic field. In general, one may refer to any order parameter that appears spontaneously and is switchable, as in the above two examples, as a *ferroic* order parameter. Four primary ferroic order parameters are frequently discussed. Apart from the aforementioned ferroelectric and ferromagnetic orderings, there are also *ferroelastic* and *ferrotoroidic* orderings [72]. Some materials may have more than one primary ferroic order parameter in a single phase. Such materials are called *multiferroics*. In the literature, the term 'multiferroic' is often used to describe a wider range of materials, which may include other orderings such as antiferromagnetism, ferrimagnetism etc. We will also use this term in a general sense.

Materials in which electric and magnetic properties are coupled are called *magnetoelectrics*. Multiferroics are often magnetoelectrics and vice-versa. However, in general one should distinguish between the meanings of these terms.

Multiferroic and magnetoelectric materials are currently under intensive study, both from the point of view of fundamental materials physics, and because of their potential application in memories, sensors, and transducers [72]. An interesting class of systems are improper ferroelectrics (see Sec. 1.2) in which an electric polarization is induced by the magnetic order.

Magnetically induced ferroelectricity provides a route to materials with a large magneto-electric (ME) effect. The appearance of the ferroelectric phase associated with a particular magnetic order

already suggests that magnetic and electric properties are closely interconnected within a given material. Therefore, one might expect to observe a strong dependence of the electric polarization on external magnetic fields in such materials, or a strong dependence of magnetic properties on electric fields. A large interplay between ferroelectricity and magnetism has been experimentally observed in a variety of compounds of this type, including $(Gd,Tb,Dy)MnO_3$, $(Tb,Dy)Mn_2O_5$, $Ni_3V_2O_8$, etc. [73–76].

4.1.2 Inversion symmetry breaking

Since polarization is a polar vector quantity, it is necessary to break the inversion symmetry in order for the ferroelectric phase to appear. This can happen in collinear spin systems if the spin pattern breaks inversion symmetry via exchange striction or related effects [77–82]. In such systems, the crystal structure considered separately from the magnetic structure (e.g. in the paramagnetic phase) may have inversion symmetry. If one then creates a certain spin pattern (which by itself also may have inversion symmetry), the spins together with the lattice can break the inversion symmetry. This can happen if the centers of the inversion symmetry of the lattice and spins do not coincide, and may lead to a further polar distortion of the lattice. Therefore, these systems are improper ferroelectrics, in which ferroelectricity is induced by the magnetic order. A simple example of such a mechanism of inversion symmetry breaking is found in Ca_3CoMnO_6 [81], as schematically illustrated in Fig. 4.1.

In this work, we shall be concerned with another class of systems in which a non-collinear cycloidal spin structure induces an electric polarization via the spin-orbit (SO) interaction [83]; examples include $Ni_3V_2O_8$ [76], $CuFeO_2$ [84], and orthorhombic $RMnO_3$ [73, 85, 86]. This mechanism is schematically illustrated in Fig. 4.2. Again, in these systems, the crystal structure in the paramagnetic phase does have inversion symmetry. The spiral spin structure, however, breaks this symmetry, because the spatial inversion operation changes the chirality of the spin spiral. The SO coupling is essential in this mechanism in order to allow the broken symmetry to be communicated from the magnetic to the charge and lattice degrees of freedom.
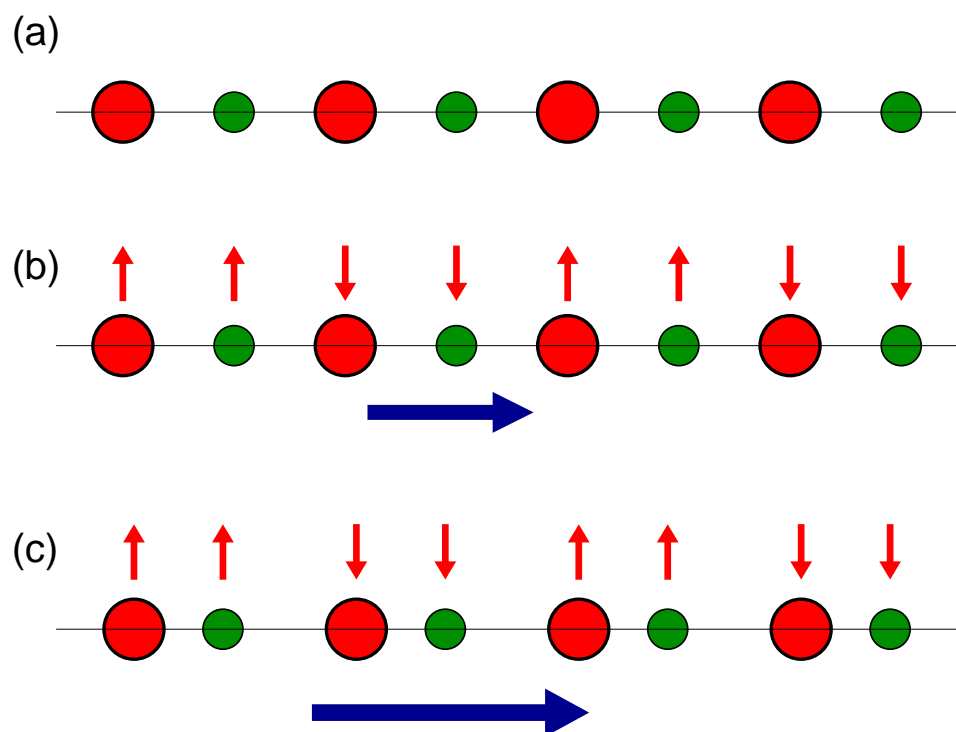
Figure 4.1: Schematic illustration of inversion symmetry breaking by a collinear magnetic order in Ca_3CoMnO_6. The circles represent Co and Mn ions. The lattice has inversion symmetry in a paramagnetic phase (a). The onset of the up-up-down-down spin pattern shown by small arrows above the circles in (b) breaks the inversion symmetry. This leads to a polar distortion of the lattice (c). Large arrows show the direction of electric polarization.
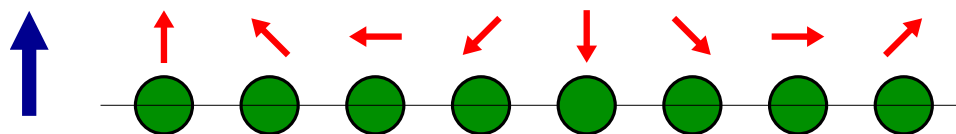
Figure 4.2: Schematic illustration of inversion symmetry breaking by a non-collinear magnetic order. Small arrows show the magnetic moments. Large arrow show the direction of electric polarization.

While such spiral spin structures and the resulting polarizations usually appear only at low temperature, these systems are of special interest because the coupling between magnetic and electric degrees of freedom is so profound.

4.1.3   Symmetric and antisymmetric exchange interaction

In the previous section we discussed how collinear and non-collinear magnetism can break the inversion symmetry. However, the inversion symmetry breaking alone is not sufficient to induce the electric polarization. The physical mechanisms of polarization induction by magnetic order are often discussed in terms of exchange (or superexchange, if the interaction between magnetic ions is mediated through a ligand) interaction between magnetic ions. Here, we will discuss this interaction from a phenomenological point of view. For simplicity, we will focus on the two examples from the previous section: Ca_3CoMnO_6 for a discussion of collinear magnetism, and $TbMnO_3$ with the spin spiral of the form depicted in Fig. 4.2 for a discussion of non-collinear magnetism (the circles in the figure can be viewed as Mn ions in this example). Of course, these examples do not cover every possible scenario of magnetically induced ferroelectricity in real materials, but they give a feeling for the role played by the exchange interaction.

We start by writing a general expression for the term in the Hamiltonian describing the exchange interaction between two magnetic ions,

$$H_{\text{ex}} = \vec{S}_1 \cdot \overleftrightarrow{J} \cdot \vec{S}_2, \tag{4.1}$$

where $\vec{S}_1$ and $\vec{S}_2$ are the spins on the two ions and $\overleftrightarrow{J}$ is the 3×3 exchange tensor. This tensor can be decomposed into a sum of the symmetric and antisymmetric parts,

$$\overleftrightarrow{J} = \overleftrightarrow{J}^{\text{S}} + \overleftrightarrow{J}^{\text{A}}. \tag{4.2}$$

Assuming isotropic exchange, the symmetric exchange tensor takes the simple form

$$\overleftrightarrow{J}^{\mathrm{S}} = \begin{pmatrix} J & 0 & 0 \\ 0 & J & 0 \\ 0 & 0 & J \end{pmatrix} \tag{4.3}$$

and the corresponding term in the Hamiltonian is just

$$H_{\mathrm{ex}}^{\mathrm{S}} = J\vec{S}_1 \cdot \vec{S}_2. \tag{4.4}$$

If $J < 0$, then spins prefer to align in the same direction (ferromagnetic exchange), while if $J > 0$ then the spins prefer an antiparallel alignment (antiferromagnetic exchange). In both Ca_3CoMnO_6 and $TbMnO_3$ considered above, the observed spin pattern is a result of the competition between nearest-neighbor ferromagnetic exchange and next-nearest-neighbor antiferromagnetic exchange interactions. (In $TbMnO_3$ the situation is more complicated and will be discussed in Sec. 4.4.3 in more detail.) In Ca_3CoMnO_6 the magnetic moments are collinear because of strong magnetic anisotropy, and the spins are aligned with the easy axis [81]. The polar distortion of the lattice shown in Fig. 4.1(c) is also explained by the symmetric exchange interaction, since nearest-neighbor spins want to move closer to each other in order to increase the exchange coupling and minimize the total energy. This mechanism is called *exchange striction*.

In $TbMnO_3$, the symmetric exchange cannot explain the appearance of electric polarization. One can see this already from the fact that, unlike in the case of Ca_3CoMnO_6, the angle between the magnetic moments of all nearest-neighbor Mn ions is the same (see Fig. 4.2). However, the antisymmetric exchange can play an important role. The corresponding tensor may be written as

$$\overleftrightarrow{J}^{\mathrm{A}} = \begin{pmatrix} 0 & D_z & -D_y \\ -D_z & 0 & D_x \\ D_y & -D_x & 0 \end{pmatrix}, \tag{4.5}$$
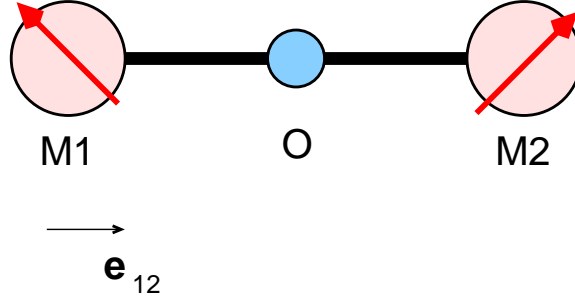
Figure 4.3: The three ion cluster model. The oxygen (O) is located half between the two transition metal ions (M1 and M2). The arrows on the metals indicate spins. The unit vector $\hat{e}_{12}$ is directed from M1 to M2.

where $\vec{D}$ is some constant vector. Using this notation, one can write the Hamiltonian term coming from the antisymmetric exchange as

$$H_{\text{ex}}^{\text{A}} = \vec{D} \cdot (\vec{S}_1 \times \vec{S}_2). \tag{4.6}$$

This interaction was originally discussed by Dzyaloshinskii and Moriya [87, 88] to explain the origin of weak ferromagnetism in α-Fe$_2$O$_3$ and other materials, in which the anisotropic superexchange causes the canting of the antiferromagnetically aligned spins. This type of exchange is called Dzyaloshinskii-Moriya (DM) interaction, and $\vec{D}$ is called the DM vector. In the case of TbMnO$_3$, the situation is the opposite: the spins are already non-collinear, and the DM interaction may be responsible for the displacements of oxygen ions in the Mn–O–Mn bond. For this reason, this interaction is often referred to as the *inverse* Dzyaloshinskii-Moriya interaction.

Let us demonstrate how this interaction may induce oxygen displacements. Consider a cluster of three ions: two transition metal ions and oxygen between them exactly in the middle, as shown in Fig. 4.3. The displacement of oxygen ion $\vec{u}$ from the center of the bond affects the strength of the exchange interaction, which is manifested by the dependence of the vector $\vec{D}$ on $\vec{u}$ [89]. In this case, to the first order in oxygen displacement $\vec{u}$, one can write $D_i = c_{ij}u_j$ (zero order term is not interesting) to arrive at

$$H_{\text{ex}}^{\text{A}} = c_{ij}u_j(\vec{S}_1 \times \vec{S}_2)_i, \tag{4.7}$$

where c_{ij} are some constants and summation over i and j is assumed. The energy is a scalar, therefore it must be invariant under inversion symmetry and all mirror symmetries of the Mn–O–Mn bond. Consider, for example, mirror symmetry M_x, which changes x to $-x$ (where $\hat{x}$ is some axis perpendicular to the bond). In the cross product $\vec{S}_1 \times \vec{S}_2$, the x-component is invariant, while other components change their sign under this symmetry. As for the displacement $\vec{u}$, only u_x changes sign. Therefore, c_{xx} must also change sign, while c_{yx} and c_{zx} must remain invariant. One can check that $c_{ij} = c\,\epsilon_{ijk}\hat{e}_{12,k}$ satisfies these conditions, where ϵ_{ijk} is the fully antisymmetric tensor and c is some constant (scalar). One can similarly verify that with the above expression for c_{ij}, the term in the Hamiltonian $H_{\mathrm{ex}}^{\mathrm{A}}$ remains invariant under mirror symmetries M_y and M_z, as well as inversion symmetry. Thus, we found that $\vec{D} = c\,(\vec{u} \times \hat{e}_{12})$ and

$$H_{\mathrm{ex}}^{\mathrm{A}} = c\,(\vec{u} \times \hat{e}_{12}) \cdot (\vec{S}_1 \times \vec{S}_2) = c\,\vec{u} \cdot (\hat{e}_{12} \times (\vec{S}_1 \times \vec{S}_2)). \tag{4.8}$$

The oxygens will move in such a way as to minimize the interaction energy $H_{\mathrm{ex}}^{\mathrm{A}}$, so that $\vec{u}$ must be parallel or antiparallel (depending on the sign of c) to $\hat{e}_{12} \times (\vec{S}_1 \times \vec{S}_2)$. These displacements will create local dipole moments along this direction. One can also see that for the spin spiral shown in Fig. 4.2, the contributions from each pair of transition metals are the same in this model. Therefore, one can write the general result

$$\vec{P} = \gamma \hat{e}_{12} \times (\vec{S}_1 \times \vec{S}_2). \tag{4.9}$$

This expression predicts the direction of polarization as shown in the figure. It can also be used to predict the direction of polarization in other types of spin patterns, e.g. conical spirals, screw spirals etc. [83]. Of course, when we say 'direction', we mean that it is parallel or antiparallel; the sign cannot be determined from these general considerations.

It should be noted that the mechanism we just described for TbMnO$_3$ is just one of the possible mechanisms proposed in literature. Here we considered this scenario for the purpose of illustrating how the electric polarization can be induced by a spiral magnetic order.

Note that we could predict the direction of the polarization induced by a cycloidal spin spiral

(Fig. 4.2) using only symmetry analysis. However, the expression given by Eq. 4.9 gives more information, e.g. how polarization depends on the wave vector of the spiral.

4.1.4 Electronic and lattice mechanisms

Theoretically, the use of symmetry analysis and phenomenological modeling have clarified the circumstances under which a spiral spin structure can give rise to an electric polarization [90–92], but these are are not well suited to identifying the dominant microscopic mechanisms. Two types of mechanisms have been discussed. The first are purely electronic mechanisms in which the SO interaction (SOI) modifies the hybridization of electronic orbitals in such a way as to shift the center of charge [93–95]. The second are 'lattice mechanisms' involving magnetically-induced ionic displacements, usually discussed in terms of inverse DM interactions [89, 92, 96]. However, it is generally difficult to estimate the magnitudes (and even signs) of these two kinds of contributions from the models. Because experiments have not been sensitive enough to resolve the tiny SO-induced atomic displacements, a central unanswered question is whether electronic or lattice mechanisms are dominant. It is also unclear whether the pattern of displacements should follow the predictions of a simple DM model, or whether more complicated interactions enter the picture.

4.2 Orthorhombic TbMnO$_3$

First-principles calculations can play an invaluable role in resolving the questions posed in the previous section. Density-functional theory (DFT) has already been used to make important contributions to the understanding of improper magnetic ferroelectrics of the collinear-spin type [97–99] and in the spiral magnetic materials like LiCu$_2$O$_2$ and LiCuVO$_4$ [100]. The spiral magnetic materials are less studied by such methods compared to collinear-spin systems. This is mainly because of the computational difficulties associated with applying these methods to systems with non-collinear magnetic order. In order to investigate the effects of magnetic spirals, one has to perform DFT calculations that allow treatment of non-collinear spins, and often the LDA+U method is needed for a proper treatment of d-electrons of transition metals. As was mentioned above, the spin-orbit

coupling also must be taken into account. Since the effects of the spin-orbit interaction are usually small, the calculations must be done with high-precision requirements for both the total energy in the electronic structure calculations and the forces for the structural relaxation of the system. To model the spin spiral itself, one has to use large supercells.

For our study [101, 4] we chose orthorhombic $TbMnO_3$ as a paradigmatic system of the cycloidal type. It also has a relatively small (20-atoms) structural unit cell, so that it is possible to use a supercell approach in our calculations. Ferroelectricity in this material was discovered by Kimura *et al.* [73]. At room temperature, $TbMnO_3$ is an orthorhombically distorted perovskite (space group *Pbnm*) with a 20-atom cell containing four formula units (see Fig. 4.4). It is paramagnetic at this temperature. The magnetic properties at low temperatures come mostly from the Mn ions. The Mn^{3+} ions form a collinear sinusoidal spin wave at temperatures between $\sim$27 K and $\sim$41 K, but below $\sim$27 K a cycloidal spin wave forms with incommensurate wave vector $k_s = 0.28$ along b, and a polarization simultaneously appears along c [73, 83]. Here the wave vectors are expressed in units of reciprocal lattice vectors. Note that the spin spiral (and any property related to the spiral) is a periodic function of k_s with a period $\Delta k_s = 2$, i.e., k_s and $k_s + 2$ correspond to the same spin spiral. The period is 2 and not 1 because the unit structural cell has *two* Mn atoms in each a–b layer (see Fig. 4.4). For example, $k_s = 0$ corresponds to a ferromagnetic spin structure (in each layer), while $k_s = 1$ corresponds to an antiferromagnetic spin structure.

4.3   Computational details

In this work, electronic-structure calculations are carried out using a plane-wave pseudopotential approach to DFT as implemented within the VASP code [45] using PAW potentials[38, 44]. (The Tb potential does not have f electrons in the valence.) We use the local-density approximation (Ceperley-Alder[102] with Vosko-Wilk-Nusair correlation[32]) with on-site Coulomb interactions (LDA+U) in a rotationally invariant formulation [29]. We consider values of U up to 4 eV. Since the periodic boundary conditions are required by our superlattice approach, we cannot model spin spirals with arbitrary wave vector, but only spirals that are commensurate with the crystal lattice.
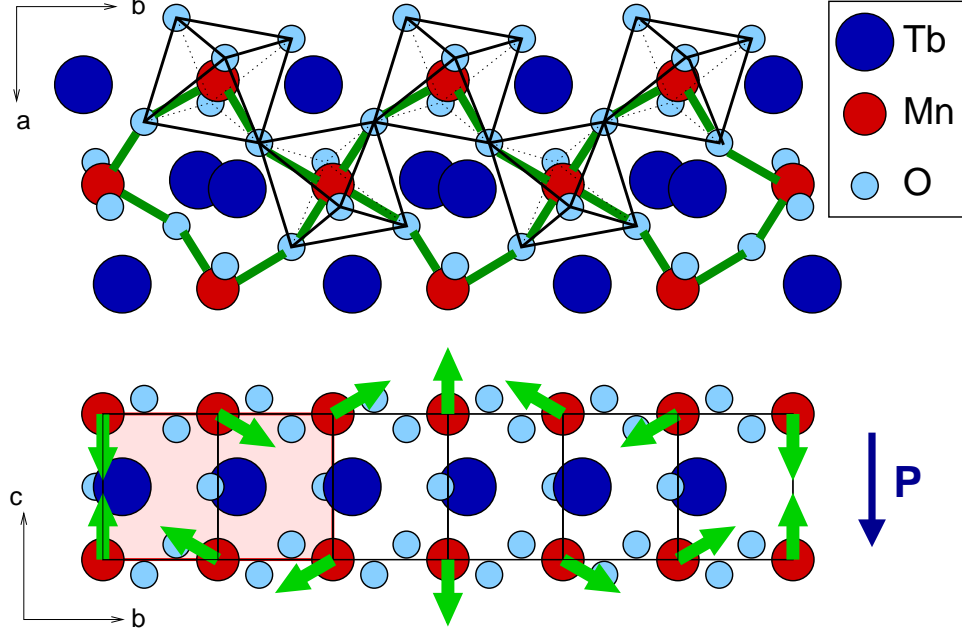
Figure 4.4: Sketch of the $a \times 3b \times c/2$ orthorhombic cell of TbMnO$_3$ (*Pbnm* space group) showing MnO$_6$ octahedral tilts (top) and the cycloidal magnetic structure on the Mn^{3+} sites (bottom) [4].

In this work, we use a 20-atom unit cell to model wave vectors $k_s = 0$ and $k_s = 1$, a 40-atom cell (unit cell doubled in the b-direction) for $k_s = 1/2$, a 60-atom cell for $k_s = 1/3$ and $k_s = 2/3$, and an 80-atom cell for $k_s = 1/4$ and $k_s = 3/4$. Fig. 4.4 shows the spin spiral with $k_s = 1/3$. Note that, in general, using the primitive cell repeated n times in the b-direction, one can construct spirals with wave vectors m/n, where $0 \leq m \leq n$. A $3 \times 1 \times 2$ k-point sampling is used for the 60-atom supercell, and equivalent k-point meshes are used for the 20- and 40-atom supercells. For the 80-atom supercell we use the same $3 \times 1 \times 2$ k-point mesh. The plane-wave energy cutoff is 500 eV, and the electric polarization is calculated using the Berry-phase approach [46].

4.4 Results

4.4.1 Crystal structure

A crystal structure optimization was performed for the 60-atom supercell (see Fig. 4.4) using $U = 1\,\text{eV}$ and $U = 4\,\text{eV}$ (see also Sec. 4.4.2 for the details regarding the choice of values of U). These calculations were carried out without SO interaction to obtain centrosymmetric reference structures,

Table 4.1: Experimental (Ref. [2]) and theoretical (this work) structural parameters for orthorhombic $TbMnO_3$.

			Exp.	$U = 1\,\text{eV}$	$U = 4\,\text{eV}$
Lattice vectors		a (Å)	5.293	5.195	5.228
		b (Å)	5.838	5.758	5.775
		c (Å)	7.403	7.308	7.343
Tb	4c(x y 1/4)	x	0.983	0.979	0.980
		y	0.082	0.084	0.084
Mn	4b(1/2 0 0)				
O1	4c(x y 1/4)	x	0.104	0.107	0.111
		y	0.467	0.469	0.465
O2	8d(x y z)	x	0.704	0.699	0.700
		y	0.326	0.320	0.323
		z	0.051	0.052	0.053

Table 4.2: The Mn–O bond lengths (Å) in MnO_6 octahedra as calculated from structural parameters given in Tab. 4.1. The bonds are listed in the order of increasing their length.

Mn–O bond	Exp.	$U = 1\,\text{eV}$	$U = 4\,\text{eV}$
1	1.905	1.912	1.912
2	1.940	1.919	1.936
3	2.220	2.148	2.174

with respect to which Berry phase polarization will be calculated in the subsequent analysis. The lattice parameters and Wyckoff coordinates of the relaxed structures are given in Tab. 4.1. For both values of U, the calculated structural parameters are very close to the experimental ones, with the lattice vectors being in slightly better agreement with experiment for the case of $U = 4\,\text{eV}$.

As one can see from the table, the crystal structure differs significantly from the ideal perovskite structure. In the ideal perovskite system ABO_3, the B sites together with their 6 neighboring oxygens form ideal BO_6 octahedra. Instead, the MnO_6 octahedra in $TbMnO_3$ are distorted (Jahn-Teller distortion). The three pairs of Mn–O bonds have different bond lengths (see Tab. 4.2), with the shortest and the longest bonds formed with the O2 oxygens (the bonds that almost lie in the a–b plane), while the bond with the medium length is to O1 (sticking out of this plane). The Jahn-Teller distortion in $TbMnO_3$ plays an important role in its electronic structure, as will be described in Sec. 4.4.2.
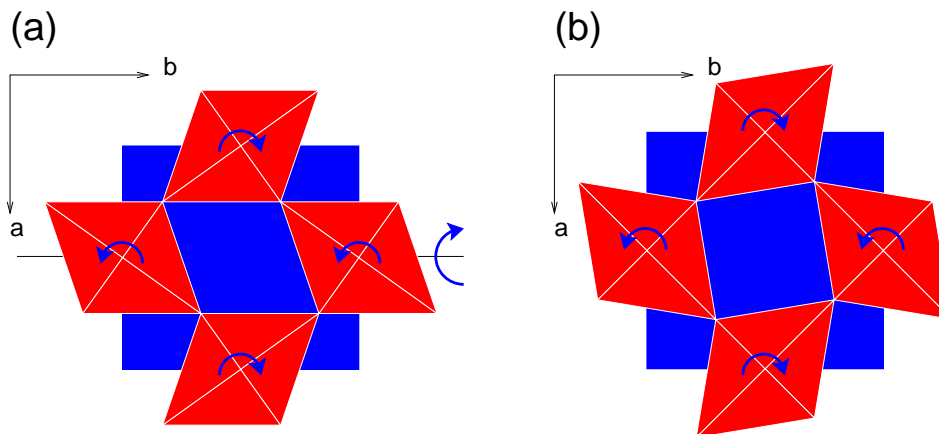
Figure 4.5: The two initial configurations considered in the model of rigid MnO_6 octahedra rotations. The positive directions of rotations are shown with curved arrows. (a) corresponds to the case 1, and (b) corresponds to the case 2 (see text for details).

Orthorhombic perovskite materials are often described in terms of octahedral rotations. In $Pbnm$ symmetry, the rotations can be described as $(a^-a^-b^+)$ in Glazer's notation [103], meaning that the octahedra are rotated around [110] and [001] axes in the original Cartesian frame. In the frame chosen as in Fig. 4.4, this corresponds to rotations around $\hat{b}$ and $\hat{c}$ axes correspondingly. A plus (minus) sign indicates that the nearest octahedra connected along the axis of rotation rotate in the same (opposite) direction.

In general, the different order of rotations leads to different final configurations, because rotations do not commute. Therefore, when describing the $TbMnO_3$ system in terms of MnO_6 octahedral rotations, one should carefully specify the meaning of the rotations and their order. For example, if we start with the ideal perovskite configuration and induce the Jahn-Teller distortion, we can arrive at several possible initial configurations as shown in Fig. 4.5. If we apply $(a^-a^-b^+)$ rotations to the configuration shown in Fig. 4.5(b), regardless of the order of rotations, the final structure will not have $Pbnm$ symmetry. However, applying rotation around $\hat{b}$ followed by rotation around $\hat{c}$ to the configuration shown in Fig. 4.5(a), we will preserve the $Pbnm$ symmetry.

Fitting the angles of rotation to the relaxed structure (Tab. 4.1), we find the rotation angles around $\hat{b}$ and $\hat{c}$ to be approximately $19.0°$ and $11.6°$ respectively.
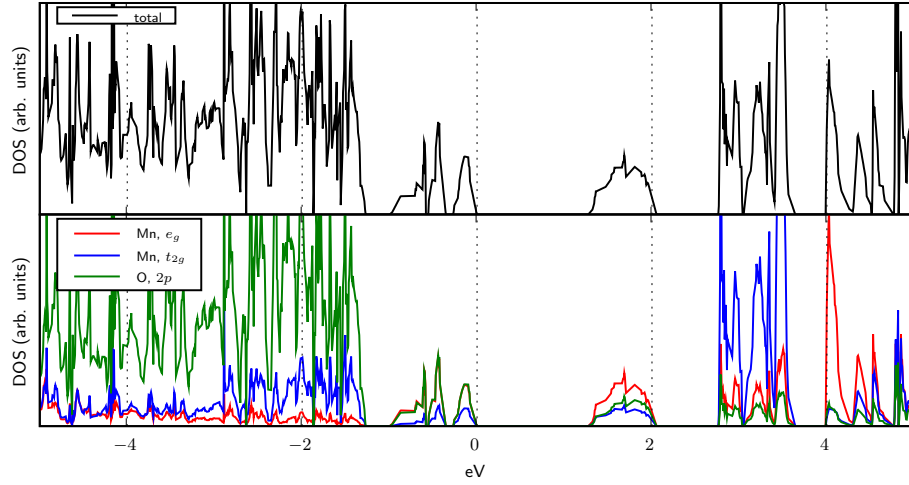
Figure 4.6: Density of states of TbMnO$_3$ with the noncollinear cycloidal spin structure ($k_\text{s} = 1/3$) for $U = 4\,\text{eV}$ in the presence of SO interaction. Top of the valence band is at $0\,\text{eV}$. Upper figure shows total density of states. Lower figure shows partial density of states projected onto Mn e_g and t_{2g} levels, and onto O $2p$ levels.

4.4.2   Electronic structure

We find that the LDA predicts TbMnO$_3$ to be metallic in the ground state. However, using the LDA+U method, we find that already for small values of U a finite band gap appears, and the system becomes insulating. The calculated density of states in the region around Fermi energy is shown in Fig. 4.6 for $U = 4\,\text{eV}$. Near the Fermi level, manganese $3d$-orbitals and oxygen $2p$-orbitals contribute most strongly to the density of states.

It is known from crystal field theory that the five $3d$ orbitals of the transition metal ion in the ideal octahedral environment form a triply degenerate t_{2g} set of orbitals (d_{xy}, d_{xz}, and d_{yz}) and a doubly degenerate e_g set ($d_{x^2-y^2}$ and d_{z^2}). The density of states projected onto the Mn e_g and t_{2g} orbitals is also shown in Fig. 4.6. The small overlap of the e_g and t_{2g} orbitals is artificial, because the MnO$_6$ octahedra are rotated with respect to the ($\hat{a},\hat{b},\hat{c}$) coordinate frame used in the calculation of the density of states. The calculation done for TbMnO$_3$ in the configuration shown in Fig. 4.5(a) shows that there is no such overlap (see Fig. 4.7). As seen from Fig. 4.6, below ∼-1 eV the states are composed of the three Mn t_{2g} (spin majority) levels and O $2p$ levels. The majority t_{2g} levels lie
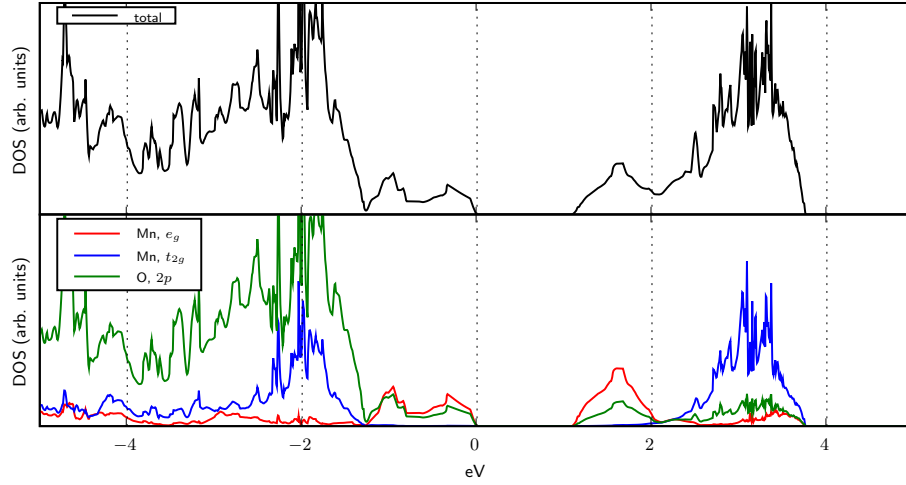
Figure 4.7: Density of states of TbMnO$_3$ with the noncollinear cycloidal spin structure ($k_\mathrm{s} = 1/3$) for the configuration shown in Fig. 4.5(a) for $U = 4\,\mathrm{eV}$ in the presence of SO interaction. Top of the valence band is at $0\,\mathrm{eV}$. Upper figure shows total density of states. Lower figure shows partial density of states projected onto Mn e_g and t_{2g} levels, and onto O $2p$ levels.

below the majority e_g levels, one of which lies just below the Fermi energy, and another one lies in the region from $\sim 1.5\,\mathrm{eV}$ to $\sim 2\,\mathrm{eV}$. Minority t_{2g} and e_g levels lie above $\sim 2\,\mathrm{eV}$. The Mn^{3+} ion has 4 electrons in the d shell, which occupy 3 t_{2g} levels and one of the e_g levels. It is important to emphasize that the Mn e_g levels are split because of the Jahn-Teller distortion. If we do a DFT calculation of TbMnO$_3$ in the ideal perovskite structure, we get a metallic state (even in the LDA+U method, see Fig. 4.8). When the Jahn-Teller distortion is taken into account, the LDA still fails to reproduce the splitting of the e_g levels, and LDA+U helps to restore the gap between these levels. The dependence of the gap on U value can be seen from the density of states calculations shown in Fig. 4.9.

We note that at $U = 1\,\mathrm{eV}$ the band gap is close to the experimental value of $\sim 0.5\,\mathrm{eV}$ [104]. For this reason, when comparing to experiments, we will mostly use numerical results obtained with this choice of U. In general, a better strategy for choosing the U value would be to calculate the exchange parameters and fit those, rather than the band gap, to the experimental data. In the present case, however, such an approach leads to a similar choice [3] of parameters.
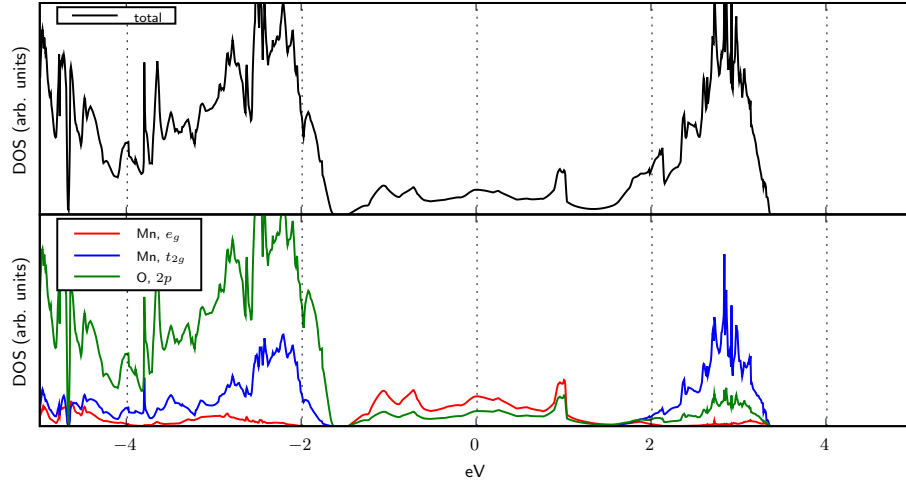
Figure 4.8: Density of states of TbMnO$_3$ with the noncollinear cycloidal spin structure ($k_\mathrm{s} = 1/3$) in ideal perovskite configuration for $U = 4\,\mathrm{eV}$ in the presence of SO interaction. Top of the valence band is at $0\,\mathrm{eV}$. Upper figure shows total density of states. Lower figure shows partial density of states projected onto Mn e_g and t_{2g} levels, and onto O $2p$ levels. Figure illustrates that without Jahn-Teller distortion, even in the LDA+U method, the system is metallic.

4.4.3 Spin structure

The appearance of the spiral spin structure in TbMnO$_3$ indicates the presence of competing interactions. However, the exact microscopic origin is a subject of much debate. It can be shown [105] that in a string of Heisenberg spins with nearest-neighbor (NN) ferromagnetic ($J_1 < 0$) or antiferromagnetic ($J_1 > 0$) interactions and next-nearest-neighbor (NNN) antiferromagnetic ($J_2 > 0$) interactions, the spin spiral can form with a wave vector **q** along the string satisfying

$$\cos(qa) = -\frac{J_1}{4J_2}. \tag{4.10}$$

This condition can easily be derived by minimizing the Hamiltonian of the form

$$H(q) = J_1 \cos(qa) + J_2 \cos(2qa). \tag{4.11}$$

Kimura *et al.* [106] suggested that in TbMnO$_3$ the incommensurate phase is a result of competing NN ferromagnetic (FM) and NNN antiferromagnetic (AFM) spin interactions in the a–b plane.
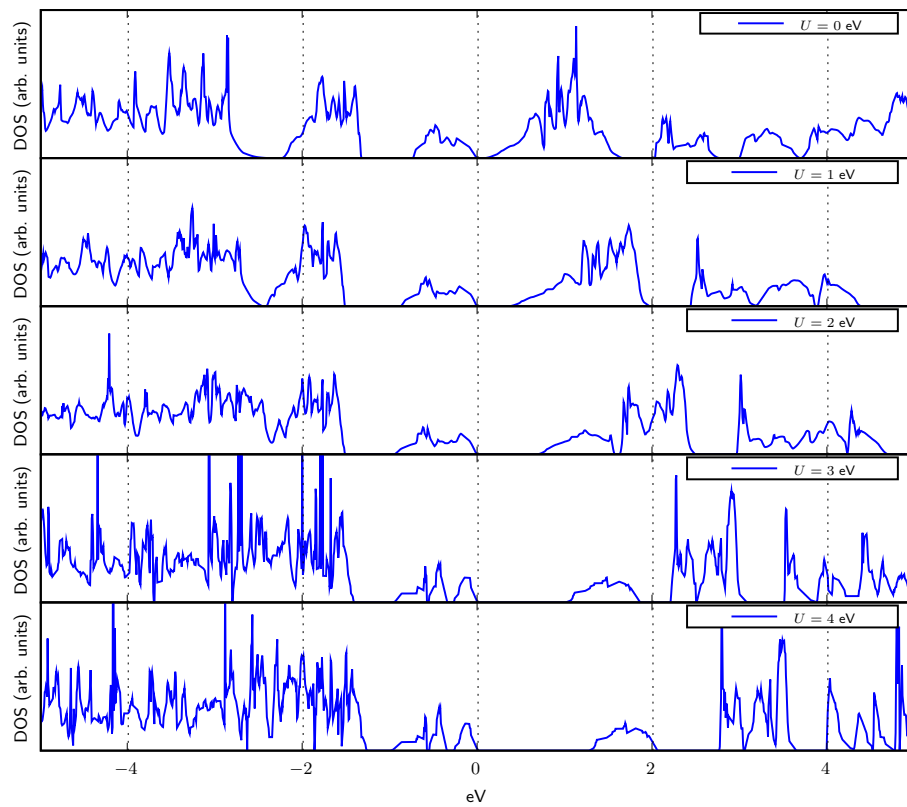
Figure 4.9: Density of states of TbMnO$_3$ with the noncollinear cycloidal spin structure ($k_\mathrm{s} = 1/3$) for various values of U in the presence of SO interaction. Top of the valence band is at $0\,\mathrm{eV}$.

Zhou and Goodenough [107] argued that the responsible competition is between FM e_g–O–e_g and AF t_{2g}–O–t_{2g} interactions in the a–b plane. Xiang *et al.* [3] from their first-principles calculations found that the NN spin interaction is antiferromagnetic rather than ferromagnetic as suggested by Kimura *et al.* They also argued that the Jahn-Teller distortion leads to a large NNN spin superexchange interaction. However, their calculated exchange couplings J_1 and J_2 were incompatible with the experimentally observed wave vector ($k_{\mathrm{s}} = 0.28$) as argued by Dong *et al.* [108]. Dong *et al.* considered an effective Hamiltonian model which, apart from the NN and NNN exchange interactions, also included Jahn-Teller distortions, and using Monte-Carlo simulations they were able to obtain a spin spiral with realistic wave vector. Sergienko and Dagotto [89] argued that Dzyaloshinskii-Moriya (DM) interaction may be responsible for the stabilization of the spin spiral in TbMnO$_3$. Recently, Mochizuki and Furukawa [109] considered a model that included superexchange interactions, single-ion anisotropy and DM interactions. They showed that the NN DM interactions in the a–b plane and the single-ion anisotropies favor the a–b cycloidal spin state, while the NN DM interactions along $\hat{c}$ favors the b–c cycloidal spin state. This competition was shown to be controlled by the NNN J_2 superexchange enhanced by the GdFeO$_3$-type distortion (movement of oxygens in Mn–O–Mn perpendicular to the Mn–Mn bond). While the complete picture of the origin of the cycloidal spin phase is not yet established, it is clear that it must have many ingredients.

In our work, we set the initial magnetic moments on Mn sites as shown in Fig. 4.4, and then allow them to evolve during the self-consistent iterations in DFT calculation. We find that the directions of the magnetic moments are stable, while their magnitude may change depending on the choice of U in the LDA+U method. Our computed magnetic moments have magnitudes of approximately $3.4\,\mu_{\mathrm{B}}$ and $3.7\,\mu_{\mathrm{B}}$ for $U = 1\,\mathrm{eV}$ and $U = 4\,\mathrm{eV}$ respectively, and rotate in the b–c plane as one scans along b, and this result hardly changes when SO is turned on. Experimentally, the magnetic moments on the Mn^{3+} sites are found to form an elliptical spiral with amplitudes $m_b = 3.9\,\mu_{\mathrm{B}}$ and $m_c = 2.8\,\mu_{\mathrm{B}}$ [85]. The origin of this ellipticity, which is apparently not captured by our calculation, deserves further investigation.

4.4.4   Contributions to the polarization

Our calculations confirmed that the Berry-phase polarization vanishes in the absence of SO. When the SO is turned on, one expects the broken inversion symmetry in the spin sector to be communicated to the spatial (charge) degrees of freedom. And indeed, as will be shown shortly, our calculations confirm this expectation.

To separate the effects of the purely electronic and lattice mechanisms discussed in Sec. 4.1.4, we proceed in the following way. First, we turn on the SO but keep the lattice vectors and ionic positions frozen. In this case, the polarization can appear only due to the change in the electronic charge density. On the other hand, if we allow the relaxation of ionic positions when the SO is turned on, we can calculate the total polarization (which includes both electronic and ionic contributions).

Focusing first on the purely electronic mechanism, we find $P^{\text{elec}} = 32\,\mu\text{C}/\text{m}^2$ and $P^{\text{elec}} = -14\,\mu\text{C}/\text{m}^2$ for $U = 1\,\text{eV}$ and $U = 4\,\text{eV}$ respectively (with the direction of polarization parallel to the c axis, as was expected from symmetry). In both cases, the magnitude is much smaller than the observed value of $\sim 600\,\mu\text{C}/\text{m}^2$ [73]. This result suggests that the lattice mechanism must be dominant, and that the electronic contribution to the polarization can be neglected for any reasonable value of U.

We now turn our attention to the lattice contribution. As a first step, we computed the Hellmann-Feynman forces appearing on the ions as the SO is turned on (with the structural coordinates still clamped). Using the 20-atom cell of the $Pbnm$ space group to label the forces, we found that: (i) 64.8% of the forces belong to the symmetry-preserving $A_1(\Gamma)$ irreducible representation (irrep); (ii) 28.7% of the forces belong to the $B_{1u}(\Gamma)$ irrep, i.e., zone-center infrared-active (IR-active) modes with dynamical dipoles along c; and (iii) 6.5% correspond to forces at $k_y = \pm 2\pi/3b$, i.e., those that would be responsible for lowering the translational symmetry of the 20-atom cell. The remaining contributions are found to vanish to numerical precision. Since the only forces that generate an electric polarization in linear order are those of type (ii), we henceforth focus our attention on the zone-center IR-active B_{1u} modes.

Eight Wyckoff coordinates contribute to the B_{1u} irrep in the 20-atom $Pbnm$ structure: three

associated with Mn atoms in Wyckoff position 4b, one each for Tb and O1 atoms in Wyckoff position 4c, and three for the O2 atoms in Wyckoff position 8d [110]. To find the polarization induced by the SOI, we need to deduce the displacements resulting from these forces. To this end we calculated the 8×8 force-constant matrix $\Phi_{ij} = -\partial f_i / \partial u_j$ connecting the B_{1u} forces and displacements at linear order using finite-difference methods (i.e., we shift each Wyckoff coordinate by $\sim 10^{-3}$ Å and calculate the resulting forces). For computational convenience, the determination of Φ_{ij} was done in the absence of SO. (A dependence of Φ_{ij} on SOI would only give a dependence of polarization at quadratic or higher order, and we are primarily concerned with linear effects. Also, we note one could have used the 20-atom unit cell for this calculation, with $k_s = 0$, since the force-constant matrix depends only weakly on the wave vector.) Furthermore, we identify the linear combination t_j of the eight coordinates corresponding to a uniform shift of the crystal along the c direction (acoustic mode) and make sure to project this combination out of the computed forces and displacements. Thus, the displacements are predicted from

$$u_i = -\sum_{j=1}^{8} \tilde{\Phi}_{ij}^{-1} f_j,$$

(4.12)

where $\tilde{\Phi}^{-1}$ is a pseudo-inverse [71] having the property that $\tilde{\Phi}^{-1}\Phi u = u$ for any u orthogonal to t.

The computed forces and predicted atomic displacements in the IR-active B_{1u} sector for TbMnO$_3$ are presented in the Tab. 4.3. We calculated the $B_{1u}(\Gamma)$ forces again in the presence of the predicted displacements and found that 99% of these forces were eliminated, thus justifying our approach. Of course, instead of computing the force-constant matrix, one could just relax the coordinates in the presence of the SOI. However, we prefer the present approach both because it is numerically more stable and because it facilitates the analysis of polarization contributions coming from phonon modes, atomic spin-orbit interactions, etc.

The distorted crystal structure is now non-centrosymmetric (space group $Pna2_1$), and the calculated Berry-phase polarization (including both electronic and ionic contributions) is $P^{\text{tot}} = -467\,\mu\text{C/m}^2$ and $P^{\text{tot}} = -218\,\mu\text{C/m}^2$ for $U = 1\,\text{eV}$ and $U = 4\,\text{eV}$ respectively. In both cases,

the total polarization is more than an order of magnitude larger than the corresponding values computed from purely electronic mechanisms, and the $U = 1\,\text{eV}$ result is comparable in magnitude with the experimental value of $\sim$-600 $\mu\text{C/m}^2$ [86]. Note that the sign of the total polarization is also in agreement with experiment.

We thus arrive at one of the major conclusions of our work, namely, that in the case of b–c spiral in TbMnO$_3$, the lattice contributions dominate strongly and have approximately the right magnitude to explain the experimentally observed polarization. Purely electronic mechanisms, e.g. as described by the Katsura-Nagaosa-Balatsky (KNB) model[93] or related work [94, 95], are not sufficient to describe the ferroelectricity in TbMnO$_3$.

4.4.5 Mode decomposition of spin-orbit induced forces and ionic displacements

Knowing the ionic displacements, one can also find the contributions to the polarization from each mode by calculating the effective charges of the modes. The results of such calculations for both values of U are given together with the forces and displacements in Tab. 4.3.

Note that the values for the forces in the table represent the forces acting on the 'modes' rather than ions themselves. Each mode is characterized by a unit vector in the (20×3)-dimensional space. Therefore, to get the actual number for the force acting on a particular ion, one must multiply the corresponding value from the table by an appropriate unit vector. This procedure will give absolute values for the ionic forces that are two times smaller than the numbers in the table for the first five modes, and $2\sqrt{2}$ times smaller for the rest of the modes.

To understand which modes contribute most strongly and to test whether simple models (based, e.g., on DM interactions) can predict the forces and displacements, we performed a further analysis as follows. For each B$_{1u}$ Wyckoff coordinate, we computed the corresponding effective charge Z (derivative of polarization with respect to the Wyckoff coordinate) by augmenting the same finite-difference calculations used earlier with Berry-phase polarization calculations. We then multiplied the effective charges by the displacements to get the contribution ΔP made by each Wyckoff coordinate. These results are also given in the Tab. 4.3. For $U = 1\,\text{eV}$, the total ionic polarization (sum

Table 4.3: Forces (meV/Å), displacements (mÅ), effective charges (e) and contributions to the polarization ($\mu C/m^2$) from IR-active modes. See text for the description of the conventions used to describe the modes. The values for ΔP^* are calculated with the SO coupling turned off everywhere except on Mn sites. In the last row, the values for ionic contributions to the polarization obtained from a direct Berry-phase calculations are given for comparison.

Wyckoff coordinate	$U = 1\,\mathrm{eV}$					$U = 4\,\mathrm{eV}$			
	F	Δu	Z	ΔP	ΔP^*	F	Δu	Z	ΔP
1 (Tb 4c, z)	0.43	−0.17	7.47	−94	−73	0.47	−0.08	7.38	−42
2 (O1 4c, z)	2.26	−0.16	−6.82	81	69	1.46	−0.03	−6.34	15
3 (Mn 4b, x)	−7.04	−0.32	0.57	−13	−14	−2.00	−0.07	0.56	−3
4 (Mn 4b, z)	−8.93	−0.45	7.46	−248	−232	−3.86	−0.18	7.02	−94
5 (Mn 4b, y)	−2.94	−0.01	0.55	0	−1	−1.06	0.04	0.65	2
6 (O2 8d, x)	5.06	0.54	0.08	3	2	2.00	0.26	0.09	2
7 (O2 8d, y)	3.57	0.93	0.23	16	9	1.59	0.41	0.19	6
8 (O2 8d, z)	4.41	0.56	−5.74	−234	−208	1.37	0.21	−5.71	−87
$\sum \Delta P$				−489	−448				−201
P^{ion}				−499					−204

of the fifth column) is $-489\,\mu C/m^2$, in good agreement with the change of polarization in going from the centrosymmetric to the distorted structure as reported earlier ($-467 - 32 = -499\,\mu C/m^2$). Similar results are found for $U = 4\,\mathrm{eV}$ (see Tab. 4.3). Not surprisingly, the Z values are much larger for the four Wyckoff coordinates involving displacements along z, and these give by far the largest contributions to ΔP.

The results in Tab. 4.3 for $U = 1\,\mathrm{eV}$ and $U = 4\,\mathrm{eV}$ may seem different, but in fact they are qualitatively similar. The forces for these two values of U may be viewed as vectors in an 8-dimensional space, and one can calculate the angle θ between them to find $\cos \theta = 0.98$. Thus, the direction of the forces is almost the same, although the magnitude is different. This means that the underlying physical mechanism of the magnetically induced polarization does not depend strongly on the choice of U, while the magnitude of the effect does change with U. Therefore, from now on we will focus only on $U = 1\,\mathrm{eV}$.

In a simple DM model [79], one considers interactions involving nearest-neighbor triplets of ions along Mn–O–Mn bonds. Such a picture leads to the expectation that a force $\gamma\, \hat{\mathbf{e}}_{nn'} \times \mathbf{S}_n \times \mathbf{S}_{n'}$ should appear on the central O ion (where γ is a coupling, $\mathbf{S}_n$ and $\mathbf{S}_{n'}$ are neighboring Mn spins, and

Table 4.4: Forces, displacements, effective charges and contributions to ionic polarization from modes corresponding to eigenvectors of the force-constant matrix.

Eigenvalue (eV/Å^2)	F (meV/Å)	Δu (mÅ)	Z^* (e)	ΔP (μC/m^2)
34.86	6.349	0.182	-8.111	-108
31.37	-8.259	-0.263	4.565	-88
13.32	2.783	0.209	8.132	125
11.87	7.614	0.641	-2.127	-100
10.35	1.684	0.163	-3.406	-41
6.99	-2.784	-0.398	4.316	-126
3.85	4.032	1.047	-1.991	-153

$\hat{\mathbf{e}}_{nn'}$ is the unit vector connecting them), with an equal and opposite force shared between the Mn ions. The cycloidal spin structure of TbMnO$_3$ is such that O1 ions should be unaffected, and O2 ions should all feel the same force along c, with Mn ions feeling an opposite force. Thus, within such a model one would expect only the 4th and 8th rows of Tab. 4.3 to give significant contributions. Inspecting the table, we see that this is rather far from being the case; one does find substantial oppositely-directed forces and displacements for the (Mn 4b, z) and (O2 8d, z) coordinates, but the forces and displacements are comparable for some other coordinates. The contributions to ΔP are more strongly dominated by these two coordinates, but only because the Z values are so much larger for displacements along $\hat{z}$. Interestingly, the Tb displacements are responsible for $\sim$20% of the lattice polarization, despite being uninvolved in the usual picture of Mn–O–Mn couplings. Thus we conclude that the simple DM model, and indeed any model that considers only nearest-neighbor Mn–Mn spin interactions, is unable to provide a detailed description of the ferroelectricity in TbMnO$_3$.

As an alternative way of analyzing the SO-induced B$_{1u}$ forces and displacements, we transform into the basis of eigenvectors of the 8×8 force-constant matrix Φ. The results are presented in Tab. 4.4. The displacements are largest for the softest mode, but other modes also show substantial displacements. Moreover, the mode dynamical charges are much larger for some of the harder modes, so that many of these also give substantial contributions. This shows that the electric polarization in TbMnO$_3$ is not dominated by a single softest mode.

4.4.6 Site-specific spin-orbit interactions

To better understand the role of the spin-orbit interaction, we studied how the behavior of the system changes depending on the strength of the SO interaction and on the presence of SO on various atomic sites. We performed calculations of the forces with the SO interaction turned off on all sites other than Tb, then Mn, then O. Using the force-constant matrix, we estimated the lattice contributions to the polarization and found them to be $-11\,\mu\text{C/m}^2$, $-447\,\mu\text{C/m}^2$ and $-8\,\mu\text{C/m}^2$, respectively. This result shows that the SO interaction on the Mn sites is responsible for almost all of the lattice-mediated contribution to the polarization (see the column for ΔP^* in the Tab. 4.3). We also calculated the purely electronic contributions to the polarizations for these three cases. Interestingly, the electronic contribution comes almost entirely from the spin-orbit effect on the Tb sites. However, since the electronic contribution is small, the relative errors in the polarization may become large, and one cannot draw definite conclusions on the role of Tb from these results. Several calculations of the forces with modified SO strength confirmed that they depend linearly on the SO strength.

4.4.7 Dependence on wave vector

Microscopic theoretical models involving the displacements of ions [89, 92, 96] show that the inverse Dzyaloshinskii-Moriya (DM) interaction can induce ferroelectric displacements of ions. Usually, only the spin interaction between the nearest-neighbor transition metals is considered in such models. As a consequence, the polarization is expected to depend sinusoidally on the angle between the spins of the nearest-neighbor Mn sites, $\mathbf{P} \propto \mathbf{e}_{n,n'} \times (\mathbf{S}_n \times \mathbf{S}_{n'})$ [83], and thus sinusoidally on k_s. To study the dependence of the lattice contribution to the electric polarization on k_s, we have carried calculations of the SO-induced forces for a 40-atom supercell ($k_\text{s} = 1/2$) and an 80-atom supercell ($k_\text{s} = 1/4$ and $k_\text{s} = 3/4$). Note also that the same 60-atom supercell can be used to set up a spiral with the wave vector $k_\text{s} = 2/3$. We also used the primitive 20-atom cell for the calculations with $k_\text{s} = 0$ and $k_\text{s} = 1$. In all these calculations we kept the same structural coordinates as for the 60-atom structure to make sure that we only change one parameter (k_s) in this study. We calculated

the forces, and again filtered those that were IR-active. We find that the pattern of the IR forces matches almost exactly that of the 60-atom cell, i.e., the directions of the eight-dimensional vectors almost coincide in all cases. Using the force-constant matrix calculated on the 60-atom supercell and the effective charges from Tab. 4.3, we can estimate the polarization for the new wave vectors. The result is shown in Fig. 4.10. Actual calculations were performed only for non-negative values of k_s, as symmetry arguments show that the polarization must be an odd function of spin-spiral wave vector. The values $k_s = 0$ and $k_s = 1$ correspond to a collinear spin arrangement. In these cases the polarization was zero as expected. One can see that the dependence of the polarization on k_s deviates significantly from a simple sinusoidal form. Surprisingly, the polarization is almost linear in k_s up to $k_s = 1/2$; such a linear dependence is expected in the long-wavelength limit, but that is a rather stretched assumption for k_s up to 1/2. This result indicates that nearest-neighbor DM models oversimplify the mechanism of the polarization induction, and that taking the next-nearest-neighbor interactions into account may be important.

The experimental k_s lies in the range where we can assume a linear dependence. The extrapolation to $k_s = 0.28$ yields a value for the lattice contribution of the polarization of about $-410\,\mu\text{C/m}^2$.

Fig. 4.10 also shows the dependence of the total energy per formula unit on the wave vector. The parameters E_1 and E_2 essentially give us the exchange parameters in the effective Hamiltonian (4.11). Assuming that the interactions responsible for the appearance of the spin spiral are intralayer NN (J_1) and NNN (J_2) superexchange interactions, from the parameters of the Fourier fit we find $J_1 = -1.7\,\text{meV}$ and $J_2 = 1.2\,\text{meV}$. Note that not all NNN interaction paths are equivalent, and thus J_2 is the average exchange parameter. We can use Eq. (4.10) to find the wave vector k_s minimizing the energy given by Eq. (4.11), keeping in mind that in our case $qa = k_s\pi$. Such a calculation yields $k_s = 0.38$, slightly overestimating the experimental value of k_s. We remind that in these calculations the structural parameters were kept fixed (and obtained by the full relaxation of the structure with k_s in the absence of the SOI), with only the directions of the magnetic moments on the Mn sites being changed.

Although the purely electronic contribution to the polarization in b–c spiral TbMnO$_3$ is rather
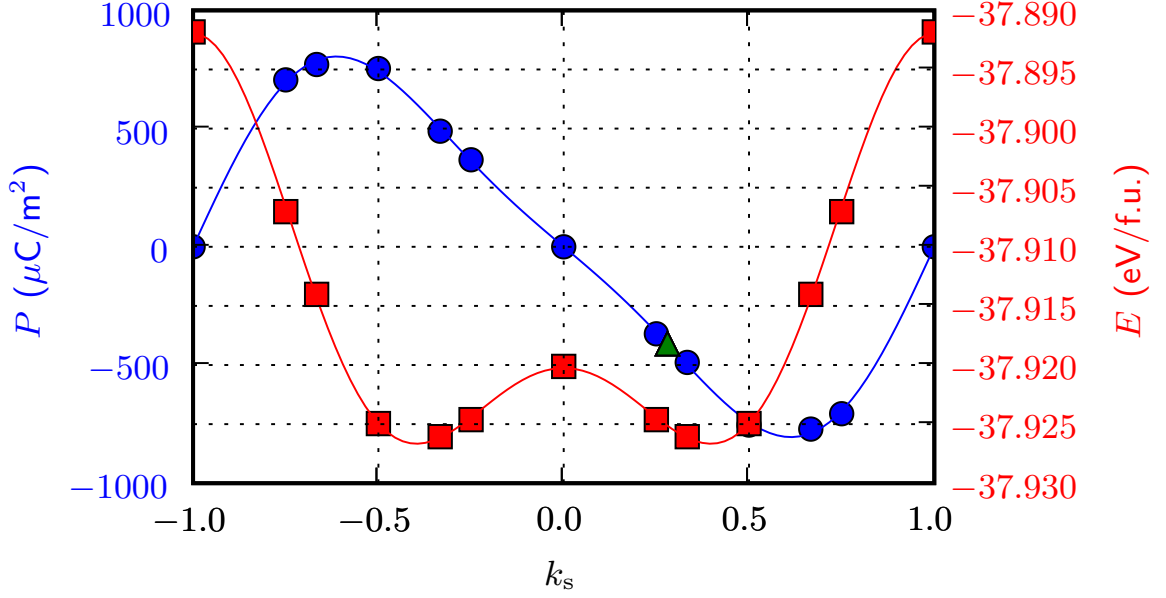
Figure 4.10: Dependence of lattice contribution to the polarization (circles, scale at left) and total energy (squares, scale at right) on the spiral wave vector k_s. The triangle indicates the extrapolation of the polarization to the experimental wave vector of $k_s = 0.28$. The curves show the Fourier fits to the data.

small, it is still worth analyzing its dependence on the spin spiral wave vector. The results of such calculations are presented in Fig. 4.11. Again, the dependence is not sinusoidal. Since we know that the polarization is an odd periodic function of k_s (with a period $\Delta k_s = 2$), we can fit the calculated points to the Fourier series

$$P = P_1 \sin(\pi k_s) + P_2 \sin(2\pi k_s) + \dots \tag{4.13}$$

Similarly, the energy, being an even and periodic function of k_s, can be expanded as

$$E = E_0 + E_1 \cos(\pi k_s) + E_2 \cos(2\pi k_s) + \dots \tag{4.14}$$

The result of such fitting is given in Tab. 4.5. One can see that the most important coefficients of the Fourier expansion are those with indices '1' and '2'. If the polarization has the DM form (Eq. 4.9), then it is easy to see that terms with index '1' come from nearest-neighbor (NN) interactions, terms with index '2' come from next-nearest-neighbor (NNN) interactions, and so on. The
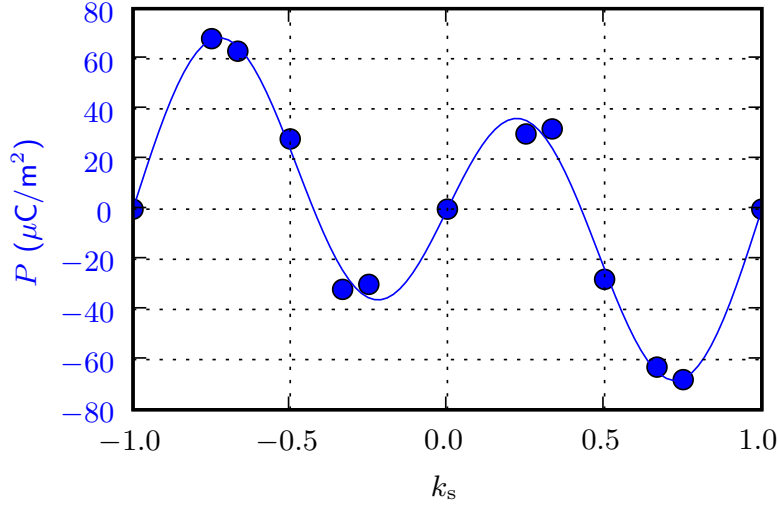
Figure 4.11: Dependence of electronic contribution to the polarization on the spiral wave vector k_s (circles). The curve shows the Fourier fit to the data.

Table 4.5: Parameters of the fits of the electronic and lattice contributions to the polarization, and the total energy to the Fourier series.

n	P_n^{elec} (μC/m^2)	P_n^{lat} (μC/m^2)	E_n (meV/f.u.)
1	-23.3	-744.2	-13.4
2	51.5	166.3	9.4
3	0.6	-2.7	-0.8

result that we see is that NNN interactions play an important role in TbMnO$_3$, and should be taken into account in models describing the origin of the induced ferroelectricity. At the same time, it is not necessary to go beyond NNN interactions, as higher-order terms in the Fourier expansions are negligible.

4.5 Spin spiral in the a–b plane

In the previous section we showed that the electronic contribution to the polarization is much smaller than the ionic contribution in TbMnO$_3$ when the spin spiral is lying in the b–c plane. Now, one can ask how general this result is. Picozzi *et al.* showed that in orthorhombic HoMnO$_3$, which is an improper ferroelectric with polarization induced by a collinear antiferromagnetic order, the

electronic contribution to the polarization is of the same order as the ionic contribution. Although the mechanism of polarization induction in $HoMnO_3$ is different from that in $TbMnO_3$, there is no *a priori* reason why the electronic contribution should be negligible in $TbMnO_3$. In this section, we study the polarization induced by the spin spiral lying in the a–b plane and show that this case differs a lot from the case of the b–c-plane spiral. In Sec. 4.6, we analyze the electronic contribution in both cases in more detail by considering a structural model of rigid MnO_6 octahedra.

It was shown experimentally [73] that when a magnetic field is applied to a $TbMnO_3$ sample along the b-direction, at some point the polarization changes its direction from c to a (this is a so-called electric polarization flop). It was naturally suggested (and recently observed [111]) that the polarization flop occurs due to the change of the spin spiral plane from b–c to a–b; the polarization simply follows the spiral. We will refer to these two magnetic states as the 'b–c spiral' and 'a–b spiral'. Note also that in the a–b spiral state the wave vector of the spiral becomes commensurate with the lattice ($k_s = 1/4$). A first-principles study by Xiang *et al.* [3] suggests that in the a–b spiral case the electronic contribution to the polarization is of the same order of magnitude as the ionic contribution.

We performed calculations of the Berry phase polarization in the case of the a–b-spiral for a set of U values from $1\,eV$ to $4\,eV$. We note that in these calculations the reference crystal structures were fully relaxed only for $U = 1\,eV$ and $U = 4\,eV$ (in the absence of SOI, see Tab. 4.1). The values of the polarization for $U = 2\,eV$ were obtained by using the lattice and structural parameters from the $U = 1\,eV$ column of Tab. 4.1. The results are presented in Tab. 4.6. For comparison, in the fourth column of the table, we show the results of similar calculations by Xiang *et al.* [3], who used $U = 2\,eV$ and also included Tb f electrons (with $U_{Tb} = 6\,eV$) in their considerations. In the b–c spiral case, as we mentioned before, the results do not depend strongly on the choice of U. Comparing in this case the results of Xiang *et al.* with our results for $U = 1\,eV$, we find an agreement in that the purely electronic contribution is negligible, and the total polarization values agree with each other within 10%. However, as seen from the Tab. 4.6, in the a–b spiral case the polarization is extremely sensitive to the value of U. The value of the electronic contribution at

Table 4.6: Purely electronic and total polarizations for the b–c and a–b spirals. Values in the column marked with one asterisk (*) were obtained using the reference crystal structures relaxed with $U = 1\,\mathrm{eV}$. Values in the column marked with two asterisks (**) are taken from Ref. [3] for comparison. The polarization values are given in $\mu\mathrm{C/m}^2$.

	U	$U = 1\,\mathrm{eV}$	$U = 2\,\mathrm{eV}^*$	$U = 2\,\mathrm{eV}^{**}$	$U = 4\,\mathrm{eV}$
b–c	P_c^{elec}	32	1	1	-14
spiral	P_c^{tot}	-467		-424	-218
a–b	P_a^{elec}	1530	691	331	174
spiral	P_a^{tot}	740		-131	-23

$U = 2\,\mathrm{eV}$ differs by a factor of two from the result of Xiang *et al.* This difference is not surprising, since the structural relaxation was performed with $U = 1\,\mathrm{eV}$ in our work, and $U = 2\,\mathrm{eV}$ in theirs (also the polarization in this case is very sensitive to the choice of exchange-correlation potential). More importantly, in all calculations the electronic contribution is comparable or even larger than the lattice contribution. This leads us to conclude that the domination of the lattice contribution in the case of b–c spiral is not a general phenomenon but was special to that case.

The high sensitivity of the polarization to the choice of U in the a–b spiral case means that (unlike in the case of b–c spiral) any prediction of the polarization made with LDA+U calculations in this case will have a large uncertainty. Even the use of the method itself becomes questionable, and perhaps other methods (such as, e.g., GW quasiparticle approaches [112]) should be exploited in this case.

Note that the magnitude of the electronic contribution in the a–b spiral case falls rapidly with increasing U. We know that the band gap increases almost linearly with U (see Fig. 4.9). Fig. 4.12 shows the electronic contributions to the polarization for both a–b and b–c spirals plotted versus the average direct band gap. One can see from the plot that, roughly, the polarization is inversely-proportional to the gap (up to a constant). This behavior can perhaps be understood as follows. Consider electric polarization as a function of ionic displacements. This function at zero ionic displacements is the purely electronic contribution (what we show in Fig. 4.12). The derivatives of the polarization with respect to ionic displacements (Born effective charges) within the density-functional perturbation theory can be written as sums of terms that are inversely proportional to the
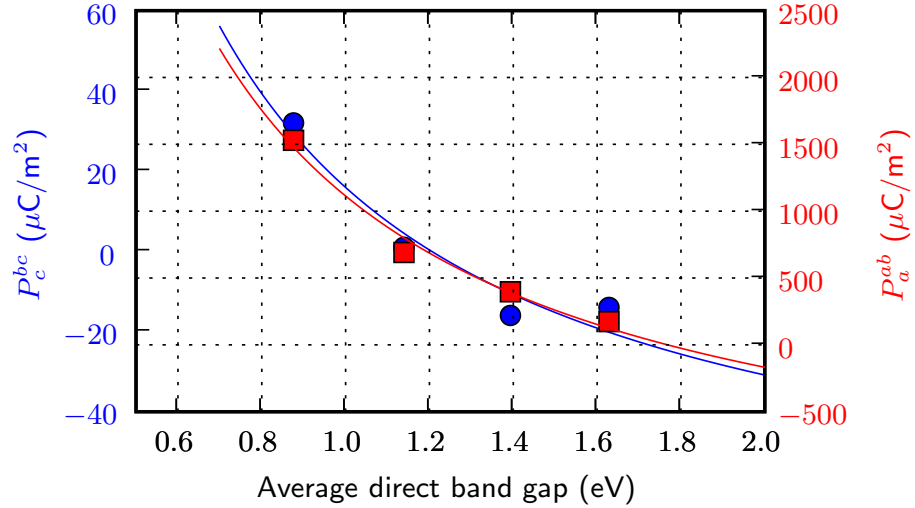
Figure 4.12: Dependence of electronic contribution to the polarization on the average direct band gap in the b–c spiral (circles, scale at left) and a–b spiral (squares, scale at right) cases when varying U.

differences of the eigenenergies of the unoccupied and occupied states [113]. The largest contributions are expected to come from the terms inversely proportional to the difference of the eigenenergies of the lowest unoccupied and highest occupied states, leading to an inverse dependence on direct band gap. If the derivatives of P with respect to displacements have this behavior, it is not very surprising to find that the polarization itself has a similar behavior.

4.6 Phenomenological model for the electronic contribution

4.6.1 Model with rigid MnO_6 octahedra rotations

To further understand the mechanism of the electronic contribution to the polarization, we decided to consider a simplified model crystal structure in which the Tb ions are placed in the high-symmetry positions (Wyckoff coordinate (0,0,1/4)), and the Mn atoms together with their 6 neighboring oxygens form rigid octahedra. We then rotated the MnO_6 octahedra and studied how the polarization depends on the rotation angles. All calculations within this model were done with $U = 1\,\mathrm{eV}$. As was discussed above, in the a–b spiral case the values of polarization are perhaps not realistic. However, at this point we are interested in understanding the origins and behavior of the polarization, rather

than making comparisons to real experiments. Also, we would like to compare the results with previous calculations, most of which were done with $U = 1$ eV.

Actually, before we even apply the rotations, we first need to apply a Jahn-Teller (JT) distortion, since we will get a metallic state otherwise (see Sec. 4.4.2). In our model, we take the JT distortion into account by constraining the ratios of the longest bond length to the shortest bond length, $\lambda_1 = 1.124$, and of the medium bond length to the shortest bond length, $\lambda_2 = 1.004$. The values of λ_1 and λ_2 are extracted from the bond lengths given in Tab. 4.2 for $U = 1$ eV.

We then apply rotations to the octahedra, starting from the configuration shown in Fig. 4.5(a) as discussed at the end of Sec. 4.4.1. In the fully relaxed structure the rotational angles around $\hat{b}$ and $\hat{c}$ are approximately $19.0°$ and $11.6°$ respectively. We constrain the ratio between these two angles (1.64), and calculate the polarization for the a–b and b–c spirals for a range of rotation angles θ around $\hat{b}$ from $-15°$ to $20°$. We also made several calculations for the initial configuration shown in Fig. 4.5(b), where the octahedra were rotated only around $\hat{c}$. To distinguish between the two sets of calculations, we will refer to the first one as 'case 1', and to the second one as 'case 2'. The results of the calculations are presented in Fig. 4.13 and Fig. 4.14. We remind that all structures considered here have inversion symmetry, and the Berry-phase calculations give us purely electronic contribution to the polarization induced by the SOI.

These calculations reveal that even in the case of the b–c spiral the electronic contribution to the polarization spans a wide range of values ($\sim 300\ \mu C/m^2$) depending on the octahedral rotations. This is another indication that this contribution is negligible in the relaxed structure only by coincidence.

4.6.2 Phenomenological model

To find out whether the observed dependence of the polarization on octahedra rotations can be explained within some relatively simple model, we decided to analyze the possible contributions coming from each pair of Mn–Mn ions. As was shown in Sec. 4.4.7, the most important contributions come from the NN and NNN interactions. We start our analysis with the Mn–O–Mn triplet (see Fig. 4.3). Let us introduce the notations that will be used in this analysis. We will use $\hat{a}$, $\hat{b}$, and

Figure 4.13: Dependence of electronic contribution to the polarization in the b–c spiral case on the MnO_6 octahedral rotation angle θ, which specifies the angle of rotation around $\hat{b}$ ($\hat{c}$) in the case 1 (case 2). In the case 1, the angle of rotation around $\hat{c}$ is approximately equal to $\theta/1.64$. See text for details.
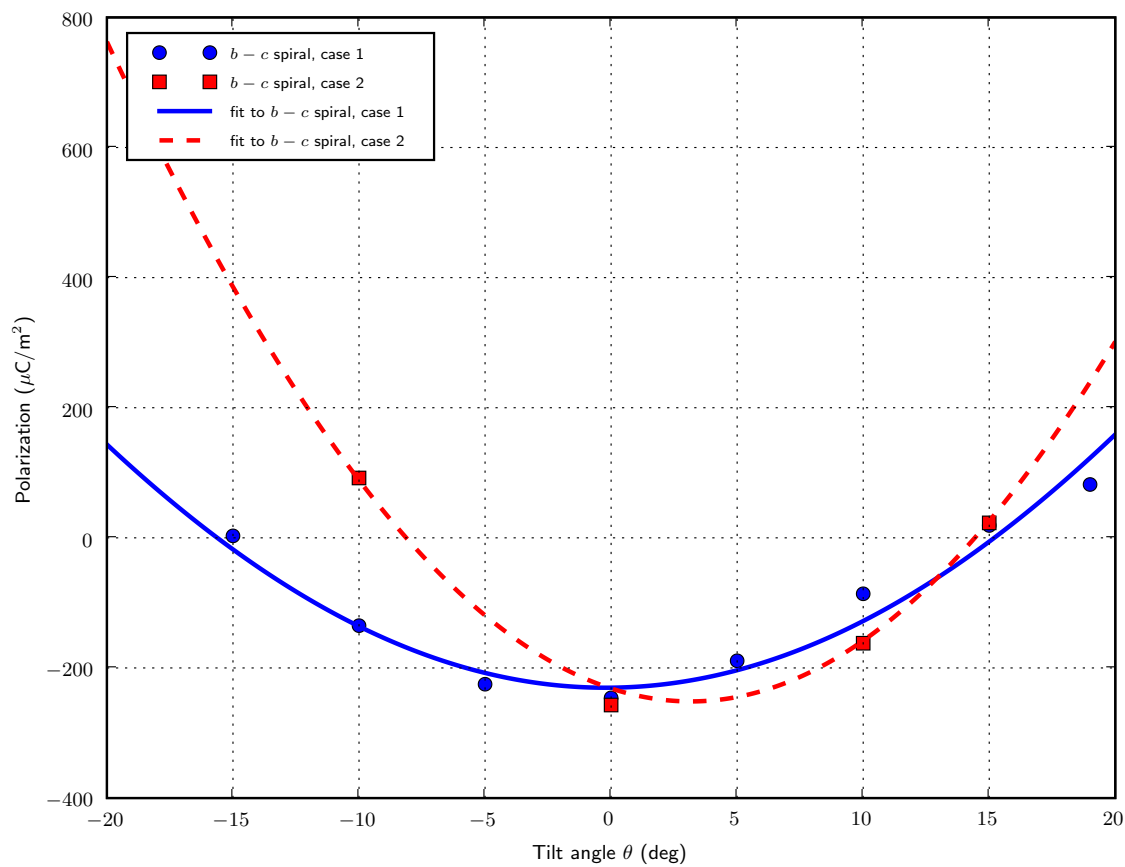
Figure 4.14: Dependence of electronic contribution to the polarization in the a–b spiral case on the MnO_6 octahedral rotation angle θ, which specifies the angle of rotation around $\hat{b}$ ($\hat{c}$) in the case 1 (case 2). In the case 1, the angle of rotation around $\hat{c}$ is approximately equal to $\theta/1.64$. See text for details.
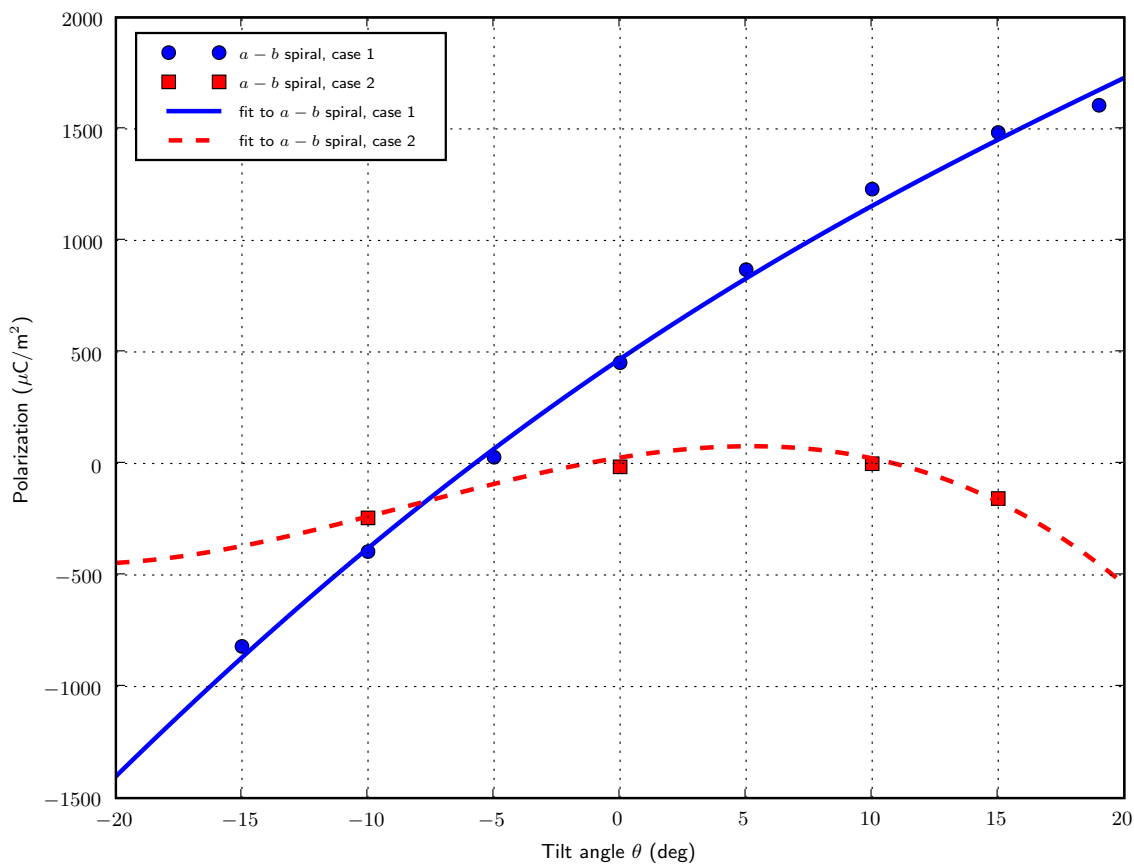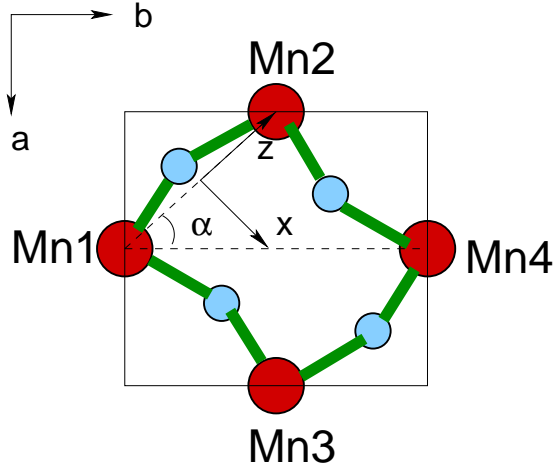
Figure 4.15: The local $(\hat{x},\hat{y},\hat{z})$ and global $(\hat{a},\hat{b},\hat{c})$ coordinate frames.

$\hat{c}$ for the unit vectors in the Cartesian directions as shown in Fig. 4.4. Other Cartesian frames will be used for each Mn–O–Mn triplet. For these we will reserve $\hat{z} = \hat{e}_{12}$ (see Fig. 4.3), while $\hat{x}$ and $\hat{y}$ are chosen so that $\hat{x}$, $\hat{y}$, and $\hat{z}$ form a right-handed system of coordinates with $\hat{x}$ lying in the a–b plane. The origin of this frame is put in the middle of the Mn–Mn bond. The angle between the bond and the direction of the spin spiral wave vector ($\hat{b}$) is denoted by α, i.e., $\cos\alpha = \hat{z} \cdot \hat{b}$ (Fig. 4.15). For the vertical bonds (i.e. bonds parallel to $\hat{c}$) the local and global Cartesian frames coincide and $\alpha = \pi/2$.

Now we classify the products of components of magnetic moments $\vec{S}_1$ and $\vec{S}_2$ using the symmetry properties of the products with respect to rotation around $\hat{z}$ and inversion symmetry. Namely, we will consider objects that are even or odd under inversion symmetry, and that are invariant (A_1), transform like a vector (x, y) (E_1), and transform like a vector $(x^2 - y^2, 2xy)$ (E_2) under rotation around $\hat{z}$. The result of such classification is shown in Tab. 4.7.

We then consider terms in the Hamiltonian that contain these spin products. Before proceeding further, we note that one can make a significant simplification. In the end we are interested in finding the expression for polarization in terms of the above spin products, and for this we need to sum the dipole moments from all Mn–Mn bonds and divide by the volume of the cell. This procedure leads to averaging of the objects from Tab. 4.7 over the spin spiral period. Therefore, it is better to calculate these averages in advance. We will denote such averages by $\langle \ldots \rangle_{ab}$ and

Table 4.7: Classification of the products of components of magnetic moments $\vec{S}_1$ and $\vec{S}_2$ by symmetry properties with respect to rotation around $\hat{z}$ and inversion symmetry.

$\hat{z}$		Inversion symmetry		
		Even		Odd
A_1	A_{1g}:	$f_0 = S_{1z}S_{2z}$ $f_0' = S_{1x}S_{2x} + S_{1y}S_{2y}$	A_{1u}:	$g_0 = S_{1x}S_{2y} - S_{1y}S_{2x}$
E_1	E_{1g}:	$\left(\begin{array}{l} f_x = S_{1x}S_{2z} + S_{1z}S_{2x} \\ f_y = S_{1y}S_{2z} + S_{1z}S_{2y} \end{array} \right)$	E_{1u}:	$\left(\begin{array}{l} g_x = S_{1x}S_{2z} - S_{1z}S_{2x} \\ g_y = S_{1y}S_{2z} - S_{1z}S_{2y} \end{array} \right)$
E_2	E_{2g}:	$\left(\begin{array}{l} f_s = S_{1x}S_{2x} - S_{1y}S_{2y} \\ f_t = S_{1x}S_{2y} + S_{1y}S_{2x} \end{array} \right)$		

$\langle \ldots \rangle_{bc}$ for the a–b and b–c spirals respectively. Consider the case of the b–c spiral first. For a given Mn1–O–Mn2 bond, the (normalized) magnetic moments on Mn1 and Mn2 are

$$
\begin{aligned}
S_{1a} &= 0 & S_{2a} &= 0 \\
S_{1b} &= -\sin\theta & S_{2b} &= -\sin(\theta + \phi) \\
S_{1c} &= \cos\theta & S_{2c} &= \cos(\theta + \phi),
\end{aligned}
\tag{4.15}
$$

where θ will be averaged over and ϕ is the angle between spins on the two neighboring Mn atoms. For the horizontal bonds shown in Fig. 4.15, $\phi = \pi k_s$, while for vertical bonds $\phi = \pi$. Let us define the average over the period of the spiral as

$$
\gamma_{\alpha\beta}^{b-c}(\phi) = \langle S_{1\alpha}S_{2\beta} \rangle_{bc} = \frac{1}{2\pi} \int_0^{2\pi} d\theta \, S_{1\alpha}(\theta, \phi) S_{2\beta}(\theta, \phi),
\tag{4.16}
$$

where α and β can be a, b or c. A straightforward calculation yields

$$
\gamma_{\alpha\beta}^{b-c} = \frac{1}{2} \begin{pmatrix} 0 & 0 & 0 \\ 0 & \cos\phi & \sin\phi \\ 0 & -\sin\phi & \cos\phi \end{pmatrix}.
\tag{4.17}
$$

Table 4.8: Relation between the spin components in the local ($\hat{x}, \hat{y}, \hat{z}$) and global ($\hat{a}, \hat{b}, \hat{c}$) frames. Angle α is the angle between $\hat{z}$ and $\hat{b}$ as shown in Fig. 4.15.

b–c spiral	a–b spiral
$S_x = S_b \sin \alpha$	$S_x = S_a \cos \alpha + S_b \sin \alpha$
$S_y = -S_c$	$S_y = 0$
$S_z = S_b \cos \alpha$	$S_z = -S_a \sin \alpha + S_b \cos \alpha$

By analogy, for the a–b spiral case (the a and c components of the magnetic moments in Eq. 4.15 are interchanged), one can find

$$
\gamma_{\alpha\beta}^{a-b} = \frac{1}{2} \begin{pmatrix} \cos \phi & -\sin \phi & 0 \\ \sin \phi & \cos \phi & 0 \\ 0 & 0 & 0 \end{pmatrix}.
\tag{4.18}
$$

We recall that objects in Tab. 4.7 are defined via the spin components in the local frame for a given Mn–Mn bond, while $\gamma_{\alpha\beta}^{b-c}$ and $\gamma_{\alpha\beta}^{a-b}$ are defined via S_a, S_b and S_c. The relation between the spin components in different frames is shown in Tab. 4.8.

Consider now, for example, the object $\langle f_0 \rangle_{bc}$. Using Tab. 4.8 we can write it as

$$
\langle f_0 \rangle_{bc} = \langle S_{1z} S_{2z} \rangle_{bc} = \langle S_{1b} S_{2b} \rangle_{bc} \cos^2 \alpha = \gamma_{bb}^{b-c} \cos^2 \alpha = \frac{1}{2} \cos \phi \cos^2 \alpha.
\tag{4.19}
$$

Similarly, one calculate the averages of all other objects in Tab. 4.7. The result is shown in Tab. 4.9.

Using the above analysis we want to find dipole moments for each Mn–O–Mn bond allowed by symmetry. Zero field dipoles can only be obtained from the energy terms linear in electric field, since $\vec{d} = -\vec{\nabla}_E U$. At the same time, the energy U must be invariant under inversion symmetry. For a moment, let us ignore oxygen displacements. Since the electric field $\vec{E}$ is odd under inversion symmetry, it can only couple to the terms in Tab. 4.7 that are also odd under inversion symmetry. In addition, the requirement that the energy must be invariant under the mirror symmetry that changes x to $-x$ leads to a conclusion that the A_{1u} term in Tab. 4.7 can only couple to an object with A_{1u} symmetry, the E_{1u} term can couple only to E_{1u}, etc. From the components of the vector of electric

Table 4.9: Averages over the spin spiral period of the objects in Tab. 4.7.

| spiral | Inversion symmetry | |
	Even	Odd
$b\text{--}c$	$\langle f_0 \rangle_{bc} = \frac{1}{2} \cos \phi \cos^2 \alpha$ $\langle f_0' \rangle_{bc} = \frac{1}{2} \cos \phi (1 + \sin^2 \alpha)$ $\langle f_x \rangle_{bc} = \frac{1}{2} \cos \phi \sin 2\alpha$ $\langle f_y \rangle_{bc} = 0$ $\langle f_s \rangle_{bc} = -\frac{1}{2} \cos \phi \cos^2 \alpha$ $\langle f_t \rangle_{bc} = 0$	$\langle g_0 \rangle_{bc} = -\sin \phi \sin \alpha$ $\langle g_x \rangle_{bc} = 0$ $\langle g_y \rangle_{bc} = \sin \phi \cos \alpha$
$a\text{--}b$	$\langle f_0 \rangle_{ab} = \frac{1}{2} \cos \phi$ $\langle f_0' \rangle_{ab} = \frac{1}{2} \cos \phi$ $\langle f_x \rangle_{ab} = 0$ $\langle f_y \rangle_{ab} = 0$ $\langle f_s \rangle_{ab} = \frac{1}{2} \cos \phi$ $\langle f_t \rangle_{ab} = 0$	$\langle g_0 \rangle_{ab} = 0$ $\langle g_x \rangle_{ab} = -\sin \phi$ $\langle g_y \rangle_{ab} = 0$

field one can only form an E_{1u} object, (E_x, E_y), which can couple to (g_x, g_y). This means that the energy term (zeroth order in oxygen displacement) must have the form

$$U_0 = -a(E_x g_x + E_y g_y), \tag{4.20}$$

where a is some constant. The dipole moment is then given by

$$\vec{d}_0 = a(g_x, g_y, 0), \tag{4.21}$$

or, after averaging over the spin spiral period,

$$\vec{d}_0 = a(\langle g_x \rangle, \langle g_y \rangle, 0). \tag{4.22}$$

Since $\phi = \pi$ for vertical bonds, $\langle g_x \rangle = \langle g_y \rangle = 0$ for both the b–c and a–b spirals. Therefore, there is no contribution to the polarization coming from the vertical bonds (this is a general result, regardless of whether we consider oxygen displacements or not). However, horizontal bonds can have nonzero dipole moments. In the case of the b–c spiral, only $\langle g_y \rangle_{bc} \neq 0$. Since in this case $\hat{y} = -\hat{c}$, the polarization is parallel to $\hat{c}$. In the case of a–b spiral, only $\langle g_x \rangle_{ab} \neq 0$. Taking into account dipole moments from all the bonds in the unit cell (see Fig. 4.15), one can see that the polarization is parallel to $\hat{a}$. Thus, we have shown from the symmetry analysis that in the b–c (a–b) spiral case the direction of polarization should be along $\hat{c}$ ($\hat{a}$) and proportional to $\sin \phi$ (or $\vec{S}_1 \times \vec{S}_2$), which is already familiar to us from Eq. 4.9. It also follows that within the current model (in which we ignore oxygen displacements) the magnitude of the polarization is the same for both spirals.

It may seem that we chose a tedious way to arrive at a simple result that is already known. However, this method allows us to go further, and take into account the displacements of oxygen ions from their ideal-perovskite positions. Suppose that for a given Mn–O–Mn bond the oxygen is displaced by $\vec{u}$ from the origin. Let us classify the terms linear in electric field $\vec{E}$ and displacement u in the same manner as we did for the spin products (see Tab. 4.10). Note that these objects are

Table 4.10: Symmetry classification of the products of components of electric field $\vec{E}$ and oxygen displacement vector $\vec{u}$.

A_{1g}	$v_0 = u_z E_z$ $v_0' = u_x E_x + u_y E_y$	$\vec{\nabla}_E v_0 = (0, 0, u_z)$ $\vec{\nabla}_E v_0' = (u_x, u_y, 0)$
A_{2g}	$\bar{v}_0 = u_x E_y - u_y E_x$	$\vec{\nabla}_E \bar{v}_0 = (-u_y, u_x, 0)$
E_{1g}	$(v_x, v_y) = (u_x, u_y) E_z$ $(v_x', v_y') = u_z (E_x, E_y)$	$\vec{\nabla}_E v_x = (0, 0, u_x), \quad \vec{\nabla}_E v_y = (0, 0, u_y)$ $\vec{\nabla}_E v_x' = (u_z, 0, 0), \quad \vec{\nabla}_E v_y' = (0, u_z, 0)$
E_{2g}	$(v_s, v_t) = (u_x E_x - u_y E_y, u_x E_y + u_y E_x)$	$\vec{\nabla}_E v_s = (u_x, -u_y, 0), \quad \vec{\nabla}_E v_t = (u_y, u_x, 0)$

even under inversion symmetry, and can only couple to f-terms in Tab. 4.7.

The corresponding energy term is

$$-U_1 = b_{11} v_0 f_0 + b_{12} v_0 f_0' + b_{21} v_0' f_0 + b_{22} v_0' f_0' + c(f_x v_x + f_y v_y) + c'(f_x v_x' + f_y v_y') + d(f_s v_s + f_t v_t).$$

$$(4.23)$$

Let us focus on the a–b spiral case, in which only $\langle f_0 \rangle_{ab}$, $\langle f_0' \rangle_{ab}$ and $\langle f_s \rangle_{ab}$ are non-zero, and all of them are equal to $1/2 \cos \phi$. In this case the energy takes a simpler form

$$-U_1^{a-b} = \frac{1}{2} \cos \phi \left[v_0(b_{11} + b_{12}) + v_0'(b_{21} + b_{22}) + d v_s \right]. \qquad (4.24)$$

The dipole moment (for a given bond) is then

$$\vec{d}_1^{a-b} = \frac{1}{2} \cos \phi \left(u_x[b_{21} + b_{22} + d], u_y[b_{21} + b_{22} - d], u_z[b_{11} + b_{12}] \right), \qquad (4.25)$$

which can be rewritten as

$$\vec{d}_1^{a-b} = (b_x u_x, b_y u_y, b_z u_z) \cos \phi, \qquad (4.26)$$

Table 4.11: Symmetry classification of the products of components of electric field $\vec{E}$ and oxygen displacement vector $\vec{u}$ to second order in oxygen displacements.

A_{1u}	$\bar{h}_0 = (u_x E_y - u_y E_x)u_z$	$\vec{\nabla}_E \bar{h}_0 = (-u_y u_z, u_x u_z, 0)$
E_{1u}	$(h_{1x}, h_{1y}) = u_z^2(E_x, E_y)$	$\vec{\nabla}_E h_{1x} = (u_z^2, 0, 0)$ $\vec{\nabla}_E h_{1y} = (0, u_z^2, 0)$
	$(h_{2x}, h_{2y}) = [u_x^2 + u_y^2](E_x, E_y)$	$\vec{\nabla}_E h_{2x} = (u_x^2 + u_y^2, 0, 0)$ $\vec{\nabla}_E h_{2y} = (0, u_x^2 + u_y^2, 0)$
	$(h_{3x}, h_{3y}) = u_z(u_x, u_y)E_z$	$\vec{\nabla}_E h_{3x} = (0, 0, u_x u_z)$ $\vec{\nabla}_E h_{3y} = (0, 0, u_y u_z)$
	$(h_{4x}, h_{4y}) = [u_x E_x + u_y E_y](u_x, u_y)$	$\vec{\nabla}_E h_{4x} = (u_x^2, u_x u_y, 0)$ $\vec{\nabla}_E h_{4y} = (u_x u_y, u_y^2, 0)$

where new constants b_x, b_y and b_z were defined. Consider a projection of this dipole moment on a-axis,

$$d_{1,a}^{a-b} = (b_x u_x \cos \alpha - b_z u_z \sin \alpha) \cos \phi. \tag{4.27}$$

To find the polarization along $\hat{a}$, we need to sum over such contributions coming from all bonds in the unit (20-atom) crystallographic cell (we already made an average over the spin spiral period, so there is no need to consider larger supercells). Consider, for example, bonds Mn_1–Mn_2 and Mn_3–Mn_4 as shown in Fig. 4.15. These two bonds make angle α with the b-axis. They also have the same phase difference ϕ. However, from $Pbnm$ symmetry it follows that u_x has opposite signs for these two bonds. This means that the contribution from the first term in Eq. 4.27 cancels out. If we consider now bond Mn_1–Mn_2, and the bond just above this (not shown in figure), we will find from symmetry that for these two bonds u_z has different sign. Therefore, the second term in Eq. 4.27 also cancels out.

Table 4.12: Parameters of the phenomenological model of the polarization extracted from the fits to Berry-phase calculations (a is given in $\mu C/m^2$, and the rest is in $\mu C/m^2/\text{Å}^2$).

	a	A	B_1	B_2	B_3	B_4
b–c spiral	-290	-1	1638	90	1772	
a–b spiral	80		-3484	-131	-2005	38452

Proceeding in this way, one can show that there is no electric polarization coming from the first order in oxygen displacements. In the second order, however, the situation is different. We will not discuss the derivation in full detail here, because it is essentially the same as for the first order. We will just give the final result. The relevant products of the components of electric field and oxygen displacements to second order in the latter are listed in Tab. 4.11. In the case of the b–c spiral the polarization is along the c axis and is given by

$$P_{bc,c} = \sin\phi \left\{ a + A u_x u_z + B_1 u_z^2 + B_2 u_x^2 + B_3 u_y^2 \right\}, \tag{4.28}$$

and in the case of a–b spiral the polarization is along the a axis:

$$P_{ab,a} = \sin\phi \left\{ a + B_4 u_x u_z + B_1 u_z^2 + B_3 u_x^2 + B_2 u_y^2 \right\}. \tag{4.29}$$

The fits (obtained separately for each of the two spin spirals) with these parameters are also shown in Fig. 4.13 and Fig. 4.14, and the calculated values for the parameters are given in Tab. 4.12.

As one can see from the figures, this model can give a fairly good description of the dependence of the polarization on oxygen displacements. However, it has serious shortcomings, as we shall discuss shortly. Nevertheless, already in this simple model, the b–c and a–b spirals have parameters unique to each case, which can explain why the polarization in the case of the b–c spiral can differ from that of the a–b spiral. We also note that a calculation of the polarization for the relaxed structure using the parameters from Tab. 4.12 yields $P_c = 1549\,\mu C/m^2$ and $P_a = 8\,\mu C/m^2$ for the b–c and a–b spirals respectively, in good agreement with the Berry-phase calculations.

The most serious shortcoming of the above model is that the parameters that appear in common
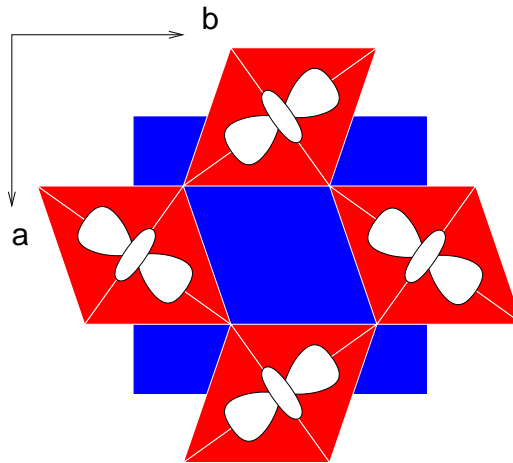
Figure 4.16: Orbital ordering in TbMnO$_3$. The $d_{3x^2-r^2}/d_{3y^2-r^2}$ orbitals are aligned along the longest Mn–O bonds. Orbital order is uniform along the c axis.

(a, B_1, B_2, and B_3) in the two fits have quite different values. Another serious problem is that it predicts certain polarization values (parameters a in Tab. 4.12) when there are no oxygen displacements from the centers of Mn–O–Mn bonds ($\vec{u} = 0$). However, when $\vec{u} = 0$ there is no Jahn-Teller distortion and the system should be metallic as we discussed in Sec. 4.4.2. It is not surprising that a simple symmetry analysis cannot distinguish between metallic and insulating states. However, one should keep in mind that there are limitation on the applicability of the model. Suppose we restrict ourselves to those displacements $\vec{u}$ that correspond to the insulating states only. For all such displacements, the Mn–O–Mn bonds do not have inversion symmetry. The question is then whether we are allowed to use this symmetry in the analysis in the first place. Moreover, the occupied e_g orbitals ($d_{3x^2-r^2}/d_{3y^2-r^2}$) align along the longest Mn–O bonds [114] as shown in Fig. 4.16. With such orbital ordering, the Mn–O–Mn bonds lying in the a–b plane do not have inversion symmetry even when $\vec{u} = 0$. We do not have to worry about the vertical Mn–O–Mn bonds because they have inversion symmetry.

Consider the configuration shown in Fig. 4.5(b). The Mn–O–Mn bonds have two mirror symmetries M_x and M_y. We may classify the products of spin components by their behavior under

Table 4.13: Classification of the products of the spin components of two neighboring spins $\vec{S}_1$ and $\vec{S}_2$, components of the polarization vector $\vec{P}$, and components of the oxygen displacement vector $\vec{u}$, by their behavior under the mirror symmetries M_x and M_y.

M_x	M_y				
+1	+1	$S_{1x}S_{2x}, S_{1y}S_{2y}, S_{1z}S_{2z}$	u_z	u_x^2, u_y^2, u_z^2	P_z
+1	−1	$S_{1y}S_{2z}, S_{1z}S_{2y}$	u_y	$u_y u_z$	P_y
−1	+1	$S_{1x}S_{2z}, S_{1z}S_{2x}$	u_x	$u_x u_z$	P_x
−1	−1	$S_{1x}S_{2y}, S_{1y}S_{2x}$		$u_x u_y$	

these two symmetries (see Tab. 4.13). Using the same notations as before for the local and global coordinate frames we can, for example, write a general expression for P_x as

$$P_x = (A_{xz}^{(0)}S_{1x}S_{2z} + A_{zx}^{(0)}S_{1z}S_{2x}) + (A_{xx}^{(1)}S_{1x}S_{2x} + A_{yy}^{(1)}S_{1y}S_{2y} + A_{zz}^{(1)}S_{1z}S_{2z})u_x$$

$$+ (A_{xy}^{(1)}S_{1x}S_{2y} + A_{yx}^{(1)}S_{1y}S_{2x})u_y + (A_{xz}^{(1)}S_{1x}S_{2z} + A_{zx}^{(1)}S_{1z}S_{2x})u_z + \ldots \quad (4.30)$$

In the above expression we only show terms that are zero and first order in $\vec{u}$ because the expression would be too long, but our analysis takes into account contributions coming from the second order as well. Similar expressions can be written for P_y and P_z. Projecting these contributions on the a, b, and c axes and averaging over the spin spiral period and all Mn-Mn bonds in the unit cell, we arrive at

$$P_{bc,c} = \sin\phi \left\{ C_0 + C_x u_x + C_z u_z + C_{xx} u_x^2 + C_{yy} u_y^2 + C_{zz} u_z^2 + C_{xz} u_x u_z \right\} \quad (4.31)$$

for the polarization in the case of the b–c spiral, and

$$P_{ab,a} = \sin\phi \left\{ A_0 + A_x u_x + A_z u_z + A_{xx} u_x^2 + A_{yy} u_y^2 + A_{zz} u_z^2 + A_{xz} u_x u_z \right\} \quad (4.32)$$

in the case of a–b spiral. Note that there are no common parameters in the two expressions. Also, linear terms in oxygen displacements appear. The results of the new fits are shown in Fig. 4.17

Table 4.14: Parameters C_i and A_i of the improved phenomenological model of the polarization extracted from the fits to Berry-phase calculations (C_0 and A_0 are expressed in $\mu C/m^2$, C_x, C_y, C_z, A_x, A_y, and A_z are in $\mu C/m^2/\text{Å}$, and the rest is in $\mu C/m^2/\text{Å}^2$).

i	0	x	z	xx	yy	zz	xz
b–c spiral	-285	-3466	211	1297	1143	3263	-30576
a–b spiral	92	-8245	529	555	-1403	361	-33707

and Fig. 4.18. Thus, this 'improved' model, though similar to the previous one, shows that in general there is no connection between the polarization in the b–c and a–b spirals. A calculation of the polarization for the relaxed structure using the parameters of the new fit (see Tab. 4.14) yields $P_c = 1600 \, \mu C/m^2$ and $P_a = 31 \, \mu C/m^2$ for the b–c and a–b spirals respectively.

4.7 Summary and discussion

We have used first-principles methods to compute the electronic and lattice contributions to the spin-orbit induced electric polarization in the cycloidal-spin compound TbMnO$_3$ with the spin spiral in the b–c plane, and find the lattice contribution to be strongly dominant. We provide a detailed analysis of the lattice contributions coming from individual sites and individual modes. Our result for the polarization agrees in sign and compares fairly well in magnitude with the experimentally measured value of $\sim$-600 $\mu C/m^2$ [86]. We also compare the results for two values of U (1 and 4 eV), and find that the mechanism of magnetoelectric coupling is quite independent of U. We find that ionic displacements depend linearly on the spin-orbit coupling, and that spin-orbit interaction on Mn sites plays the most important role in the lattice-mediated polarization.

The dependence of the polarization on the spin-spiral wave period is studied in detail. We find that it deviates significantly from the sinusoidal dependence expected from simple models. The polarization is almost linear in wave vector for absolute values of k_s up to 0.5.

The electronic contribution to the polarization is studied in detail for spin spirals lying in both the b–c and a–b planes. We find that in the latter case, the electronic contribution is of the same order

Figure 4.17: Dependence of electronic contribution to the polarization in the b–c spiral case on the MnO_6 octahedral rotation angle θ, which specifies the angle of rotation around $\hat{b}$ ($\hat{c}$) in the case 1 (case 2). In the case 1, the angle of rotation around $\hat{c}$ is approximately equal to $\theta/1.64$. See text for details. The result of the fit to the phenomenological model is also shown.
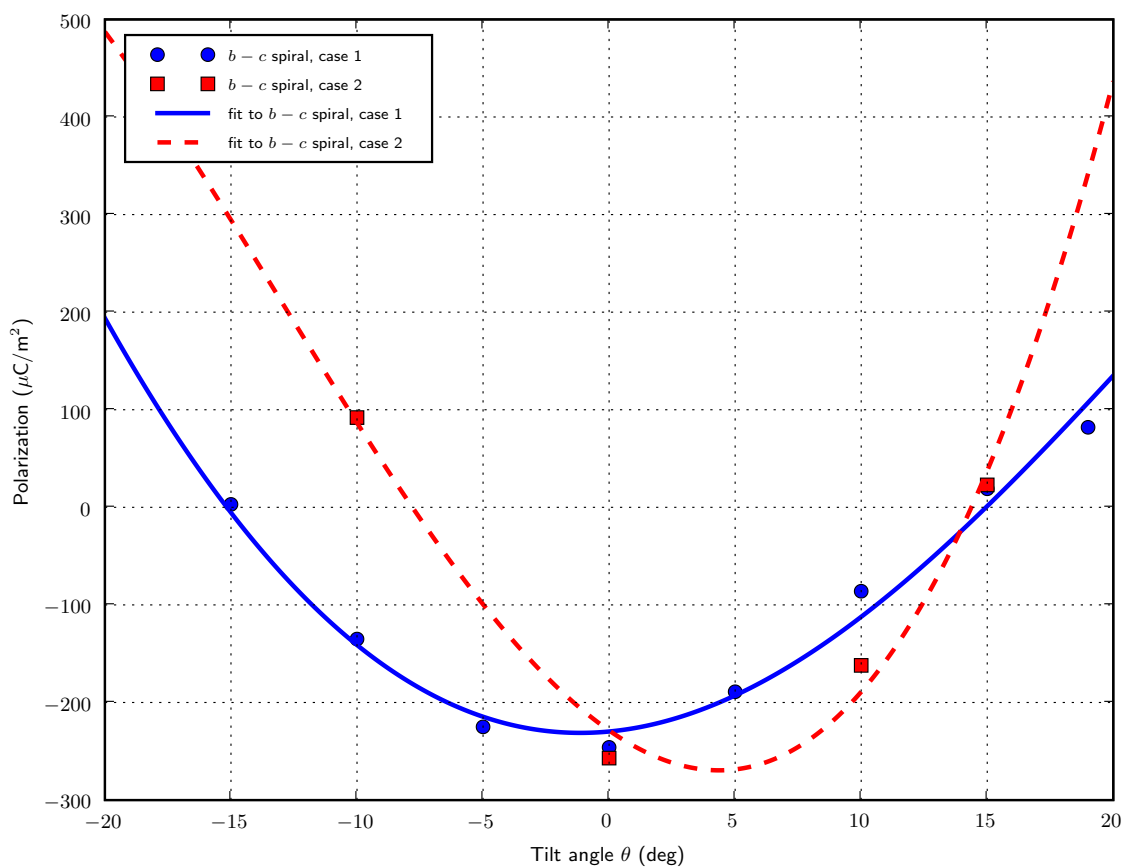
Figure 4.18: Dependence of electronic contribution to the polarization in the a–b spiral case on the MnO$_6$ octahedral rotation angle θ, which specifies the angle of rotation around $\hat{b}$ ($\hat{c}$) in the case 1 (case 2). In the case 1, the angle of rotation around $\hat{c}$ is approximately equal to $\theta/1.64$. See text for details. The result of the fit to the phenomenological model is also shown.
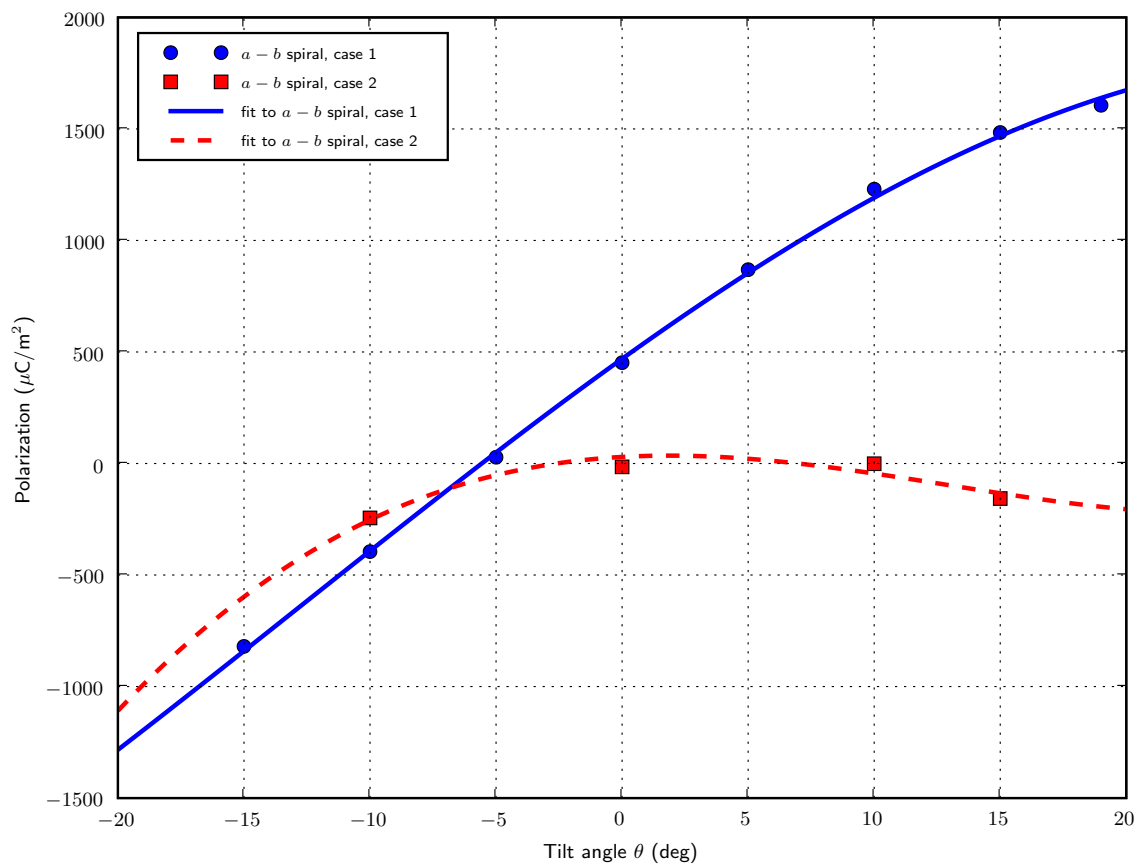
of magnitude as the lattice contribution. We also consider a structural model with rigid MnO_6 octahedral rotations, and show that electronic contribution to the polarization can significantly change with rotation angle even in the case of the b–c spiral, thus demonstrating that the fact that we could neglect this contribution for the relaxed structure was not a general result. We provide a phenomenological model describing the electronic contribution to the polarization which can explain how it can depend on oxygen displacements (to second order), and also demonstrates that the polarization in the b–c-spiral case can differ from that in the a–b-spiral case.

We found several indications that next-nearest-neighbor spin interactions are important in creating polarization in $TbMnO_3$. A construction of a microscopic model that takes these interactions into account would be of a great interest. This can be a subject for a further research.

Our work demonstrates that first-principles calculations can play an important role in understanding the mechanisms of electric polarization induction by cycloidal magnetic order. They can also give some insights in the search for materials with stronger magnetoelectric effects. In particular, to increase the effects of spin-orbit interaction, the use of heavier magnetic ions might be a good idea. Doping on the A site of $AMnO_3$ perovskites with ions having different radii can change the MnO_6 octahedral tilts, possibly leading to an increase in polarization.

The supercell approach used in this work can in principle be used for studies of other spiral magnets such as perovskite rare-earth manganates, $Ni_3V_2O_8$, $LiCu_2O_2$, etc. Since the effects studied are usually small, such calculations require high tolerances on the accuracy of the total energy and forces, and the number of unit cells one can model is limited by the computer power and memory. However these limitations will become less of an issue as technology advances.

Our calculations were mostly concerned with the ground state properties, and therefore temperature effects were not taken into account. Such effects can be studied with the help of time-dependent density functional theory calculations, Monte-Carlo simulations, or similar techniques. For example, Monte-Carlo simulations on a microscopic spin model were recently used to analyze the phase diagram of rare-earth manganites [109].

The work shows yet again the power of first-principles methods to answer important questions

in the theory of materials. Our results may be of use to experimentalists searching for materials with enhanced properties and to theorists trying to develop accurate microscopic models of the physical processes inside the materials.

Bibliography

[1] A. Malashevich and D. Vanderbilt, Phys. Rev. B **75**, 045106 (2007).

[2] J. Alonso et al., Inorg. Chem. **39**, 917 (2000).

[3] H. J. Xiang, S.-H. Wei, M.-H. Whangbo, and J. L. F. Da Silva, Phys. Rev. Lett. **101**, 037209 (2008).

[4] A. Malashevich and D. Vanderbilt, `arXiv:0905.3033v1`.

[5] R. Resta and D. Vanderbilt, in *Physics of Ferroelectrics: a Modern Perspective*, edited by K. M. Rabe, C. H. Ahn, and J.-M. Triscone (Springer-Verlag, Berlin, 2007).

[6] T. Mitsui, I. Tatsuzaki, and E. Nakamura, *An Introduction to the Physics of Ferroelecetrics* (Gordon and Breach Science Publishers, London, 1976).

[7] J. Valasek, Phys. Rev. **17**, 475 (1921).

[8] L. D. Landau and E. M. Lifshitz, *Statistical Physics* (Addison-Wesley, Reading MA, 1969).

[9] A. P. Levanyuk and D. G. Sannikov, Usp. Fiz. Nauk. **112**, 561 (1974).

[10] K. Lukaszewicz and J. Karut-Kalicinska, Ferroelectrics **7**, 81 (1974).

[11] C. J. Fennie and K. M. Rabe, Phys. Rev. B **72**, 100103(R) (2005).

[12] Y. Ishibashi and Y. Takagi, Jap. J. Appl. Phys. **15**, 1621 (1976).

[13] P. Hohenberg and W. Kohn, Phys. Rev. **136**, B864 (1964).

[14] W. Kohn and L. J. Sham, Phys. Rev. **140**, A1133 (1965).

[15] R. O. Jones and O. Gunnarsson, Rev. Mod. Phys. **61**, 689 (1989).

[16] R. G. Parr and W. Yang, *Density-Functional Theory of Atoms and Molecules* (Oxford University Press, New York, 1989).

[17] K. Terakura, T. Oguchi, A. R. Williams, and J. Kübler, Phys. Rev. Lett. **52**, 1830 (1984).

[18] K. Terakura, T. Oguchi, A. R. Williams, and J. Kübler, Phys. Rev. B **30**, 4734 (1984).

[19] J. P. Perdew, R. G. Parr, M. Levy, and J. J. L. Balduz, Phys. Rev. Lett. **49**, 1691 (1982).

[20] A. I. Liechtenstein, V. I. Anisimov, and J. Zaanen, Phys. Rev. B **52**, R5467 (1995).

[21] V. I. Anisimov, J. Zaanen, and O. K. Andersen, Phys. Rev. B **44**, 943 (1991).

[22] V. I. Anisimov, F. Aryasetiawan, and A. I. Liechtenstein, J. Phys.: Condens. Matter. **9**, 767

(1997).

[23] O. Gunnarsson, O. K. Andersen, O. Jepsen, and J. Zaanen, Phys. Rev. B **39**, 1708 (1989).

[24] J. F. Janak, Phys. Rev. B **18**, 7165 (1978).

[25] V. I. Anisimov, I. V. Solovyev, M. A. Korotin, M. Czyżyk, and G. A. Sawatzky, Phys. Rev. B **48**, 16929 (1993).

[26] J. C. Slater, Phys. Rev. **34**, 1293 (1929).

[27] J. J. Sakurai, *Modern Quantum Mechanics* (Addison-Wesley, Reading MA, 1994).

[28] F. M. F. de Groot, J. C. Fuggle, B. T. Thole, and G. A. Sawatzky, Phys. Rev. B **42**, 5459 (1990).

[29] S. L. Dudarev, G. A. Botton, S. Y. Savrasov, C. J. Humphreys, and A. P. Sutton, Phys. Rev. B **57**, 1505 (1998).

[30] J. P. Perdew and Y. Wang, Phys. Rev. B **45**, 13244 (1992).

[31] U. von Barth and L. Hedin, J. Phys. C: Solid State Phys. **5**, 1629 (1972).

[32] S. H. Vosko, L. Wilk, and M. Nusair, Can. J. Phys. **58**, 1200 (1980).

[33] J. Kübler, K.-H. Höck, and J. Sticht, J. Appl. Phys. **63**, 3482 (1988).

[34] P. A. M. Dirac, Proc. Roy. Soc. London Ser. A **117**, 610 (1928).

[35] P. A. M. Dirac, Proc. Roy. Soc. London Ser. A **118**, 351 (1928).

[36] J. D. Bjorken and S. D. Drell, *Relativistic Quantum Mechanics* (McGraw Hill, New York, 1964).

[37] D. D. Koelling and B. N. Harmon, J. Phys. C: Solid State Phys. **10**, 3107 (1977).

[38] P. E. Blöchl, Phys. Rev. B **50**, 17953 (1994).

[39] D. R. Hamann, M. Schlütter, and C. Chiang, Phys. Rev. Lett. **43**, 1494 (1979).

[40] D. Vanderbilt, Phys. Rev. B **41**, 7892 (1990).

[41] G. B. Bachelet, D. R. Hamann, and M. Schlütter, Phys. Rev. B **26**, 4199 (1982).

[42] X. Gonze, J. M. Beuken, R. Caracas, F. Detraux, M. Fuchs, G. M. Rignanese, L. Sindic, M. Verstraete, G. Zerah, F. Jollet, et al., Comput. Mater. Sci. **25**, 478 (2002).

[43] QUANTUM-ESPRESSO is a community project for high-quality quantum-simulation software, based on density-functional theory, and coordinated by Paolo Giannozzi. See http://www.quantum-espresso.org and http://www.pwscf.org.

[44] G. Kresse and D. Joubert, Phys. Rev. B **59**, 1758 (1999).

[45] G. Kresse and J. Furthmüller, Comput. Mater. Sci. **6**, 15 (1996); Phys. Rev. B **54**, 11169 (1996).

[46] R. D. King-Smith and D. Vanderbilt, Phys. Rev. B **47**, 1651 (1993).

[47] R. Resta, Rev. Mod. Phys. **66**, 899 (1994).

[48] A. Ohtomo, M. Kawasaki, T. Koida, K. Masubuchi, H. Koinuma, Y. Sakurai, Y. Yoshida, T. Yasuda, and Y. Segawa, Appl. Phys. Lett. **72**, 2466 (1998).

[49] S. Adachi, *GaAs and Related Materials* (World Scientific Publishing Co., 1994).

[50] A. Bykhovski, B. Gelmont, M. Shur, and A. Khan, J. Appl. Phys. **77**, 1616 (1995).

[51] T. Gruber, C. Kirchner, R. Kling, F. Reuss, and A. Waag, Appl. Phys. Lett. **84**, 5359 (2004).

[52] X. Zhang, H. Ma, Q. Wang, J. Ma, F. Zong, H. Xiao, and S. H. F. Ji, Physica B **364**, 157 (2005).

[53] Z. C. Tu and X. Hu, Phys. Rev. B **74**, 035434 (2006).

[54] H. J. Xiang, J. Yang, J. G. Hou, and Q. Zhu, Appl. Phys. Lett. **89**, 223111 (2006).

[55] Y. W. Heo, M. Kaufman, K. Pruessner, D. P. Norton, F. Ren, M. F. Chisholm, and P. H. Fleming, Solid-State Electron. **47**, 2269 (2003).

[56] Y. W. Heo, C. Abernathy, K. Pruessner, W. Sigmund, D. P. Norton, M. Overberg, F. Ren, and M. F. Chisholm, J. Appl. Phys. **96**, 3424 (2004).

[57] N. B. Chen, H. Z. Wu, D. J. Qiu, T. N. Xu, J. Chen, and W. Z. Shen, J. Phys.: Condens. Matter **16**, 2973 (2004).

[58] A. Schleife, F. Fuchs, J. Furthmüller, and F. Bechstedt, Phys. Rev. B **73**, 245212 (2006).

[59] A. Dal Corso, M. Posternak, R. Resta, and A. Baldareschi, Phys. Rev. B **50**, 10715 (1994).

[60] S. Limpijumnong and W. R. L. Lambrecht, Phys. Rev. B **63**, 104103 (2001).

[61] P. Gopal and N. A. Spaldin, J. Elec. Materials **35**, 538 (2006).

[62] W. R. L. Lambrecht, S. Limpijumnong, and B. Segall (1999), MRS Internet J. Nitride Semicond. Res. 4S1, G6.8.

[63] Y.-S. Kim, E.-C. Lee, and K. J. Chang, J. Korean Phys. Soc. **39**, S92 (2001).

[64] M. Sanati, G. L. W. Hart, and A. Zunger, Phys. Rev. B **68**, 155210 (2003).

[65] J. F. Sarver, F. L. Katnack, and F. A. Hummel, J. Electrochem. Soc. **106**, 960 (1959).

[66] S. Goedecker, M. Teter, and J. Huetter, Phys. Rev. B **54**, 1703 (1996).

[67] N. Troullier and J. L. Martins, Phys. Rev. B **43**, 1993 (1991).

[68] N. A. Hill and U. Waghmare, Phys. Rev. B **62**, 8802 (2000).

[69] J. Serrano, A. H. Romero, F. J. Manjón, R. Lauck, M. Cardona, and A. Rubio, Phys. Rev. B **69**, 094306 (2004).

[70] F. Decremps, F. Datchi, A. M. Saitta, A. Polian, S. Pascarelli, A. DiCicco, J. P. Itié, and F. Baudelet, Phys. Rev. B **68**, 104101 (2003).

[71] X. Wu, D. Vanderbilt, and D. R. Hamann, Phys. Rev. B **72**, 035105 (2005).

[72] M. Fiebig, J. Phys. D: Appl. Phys. **38**, R123 (2005).

[73] T. Kimura, T. Goto, H. Shintani, K. Ishizaka, T. Arima, and Y. Tokura, Nature **426**, 55 (2003).

[74] T. Lottermoser, T. Lonkai, U. Amann, D. Hohlwein, J. Ihringer, and M. Fiebig, Nature **430**, 541 (2004).

[75] N. Hur, S. Park, P. A. Sharma, J. S. Ahn, S. Guha, and S.-W. Cheong, Nature **429**, 392 (2004).

[76] G. Lawes, A. B. Harris, T. Kimura, N. Rogado, R. J. Cava, A. Aharony, O. Entin-Wohlman, T. Yildirim, M. Kenzelmann, C. Broholm, et al., Phys. Rev. Lett. **95**, 087205 (2005).

[77] L. C. Chapon, P. G. Radaelli, G. R. Blake, S. Park, and S. W. Cheong, Phys. Rev. Lett. **96**, 097601 (2006).

[78] A. Muñoz, M. T. Casáis, J. A. Alonso, M. J. Martínez-Lope, J. L. Martínez, and M. T. Fernández-Díaz, Inorg. Chem. **40**, 1020 (2001).

[79] I. A. Sergienko, C. Sen, and E. Dagotto, Phys. Rev. Lett. **97**, 227204 (2006).

[80] N. Aliouane, D. N. Argyriou, J. Strempfer, I. Zegkinoglou, S. Landsgesell, and M. v. Zimmermann, Phys. Rev. B **73**, 020102(R) (2006).

[81] Y. J. Choi, H. T. Yi, S. Lee, Q. Huang, V. Kiryukhin, and S.-W. Cheong, Phys. Rev. Lett. **100**, 047601 (2008).

[82] S.-W. Cheong and M. Mostovoy, Nature Materials **6**, 13 (2007).

[83] T. Kimura, Annu. Rev. Matter. Res. **37**, 387 (2007).

[84] T. Kimura, J. C. Lashley, and A. P. Ramirez, Phys. Rev. B **73**, 220401(R) (2006).

[85] M. Kenzelmann, A. B. Harris, S. Jonas, C. Broholm, J. S. S. B. Kim, C. L. Zhang, S.-W. Cheong, O. P. Vajk, and J. Lynn, Phys. Rev. Lett. **95**, 087206 (2005).

[86] Y. Yamasaki, H. Sagayama, T. Goto, M. Matsuura, K. Hirota, T. Arima and Y. Tokura, Phys. Rev. Lett. **98**, 147204 (2007); Phys. Rev. Lett. **100**, 219902(E) (2008).

[87] I. Dzyaloshinsky, J. Phys. Chem. Solids **4**, 241 (1958).

[88] T. Moriya, Phys. Rev. **120**, 91 (1960).

[89] I. A. Sergienko and E. Dagotto, Phys. Rev. B **73**, 094434 (2006).

[90] M. Mostovoy, Phys. Rev. Lett. **96**, 067601 (2006).

[91] P. G. Radaelli and L. C. Chapon, Phys. Rev. B **76**, 054428 (2007).

[92] A. B. Harris, J. Appl. Phys. **99**, 08E303 (2006).

[93] H. Katsura, N. Nagaosa, and A. V. Balatsky, Phys. Rev. Lett. **95**, 057205 (2005).

[94] P. Bruno and V. K. Dugaev, Phys. Rev. B **72**, 241302(R) (2005).

[95] C. Jia, S. Onoda, N. Nagaosa, and J.H. Han, Phys. Rev. B **74**, 224444 (2006); Phys. Rev. B **76**, 144424 (2007).

[96] C. D. Hu, Phys. Rev. B **77**, 174418 (2008).

[97] N. A. Hill, Annu. Rev. Mater. Res. **32**, 1 (2002).

[98] C. Wang, G.-C. Guo, and L. He, Phys. Rev. Lett. **99**, 177202 (2007).

[99] S. Picozzi, K. Yamauchi, B. Sanyal, I. A. Sergienko, and E. Dagotto, Phys. Rev. Lett. **99**, 227201 (2007).

[100] H. J. Xiang and M.-H. Whangbo, Phys. Rev. Lett. **99**, 257203 (2007).

[101] A. Malashevich and D. Vanderbilt, Phys. Rev. Lett. **101**, 037210 (2008).

[102] D. M. Ceperley and B. J. Alder, Phys. Rev. Lett. **45**, 566 (1980).

[103] A. M. Glazer, Acta Crystallogr. Sect. B **B28**, 3384 (1972).

[104] Y. Cui, C. Wang, and B. Cao, Solid State Communications **133**, 641 (2005).

[105] A. B. Harris and G. Lawes, in *Handbook of Magnetism and Advanced Magnetic Materials*, edited by H. Kronmüller and S. Parkin (Wiley-VCH, Amsterdam, 2007), vol. 4.

[106] T. Kimura, S. Ishihara, H. Shintani, T. Arima, K. T. Takahashi, K. Ishizaka, and Y. Tokura, Phys. Rev. B **68**, 060403(R) (2003).

[107] J.-S. Zhou and J. B. Goodenough, Phys. Rev. Lett. **96**, 247202 (2006).

[108] S. Dong, R. Yu, S. Yunoki, J.-M. Liu, and E. Dagotto, Phys. Rev. B **78**, 155121 (2008).

[109] M. Mochizuki and N. Furukawa, `arXiv:0905.1857v1`.

[110] E. Kroumova et al., Phase Transitions **76**, 155 (2003).

[111] N. Aliouane, K. Schmalzl, D. Senff, A. Maljuk, K. Prokeš, M. Braden, and D. N. Argyriou, Phys. Rev. Lett. **102**, 207205 (2009).

[112] L. Hedin and S. Lundqvist, in *Solid State Physics*, edited by H. Ehrenreich, F. Seitz, and

D. Turnbull (Academic, New York, 1969), vol. 23.

[113] S. Baroni and P. Giannozzi, Rev. Mod. Phys. **73**, 515 (2001).

[114] M. Tachibana, T. Shimoyama, H. Kawaji, T. Atake, and E. Takayama-Muromachi, Phys. Rev. B **75**, 144425 (2007).

Curriculum Vita
Andrei Malashevich

2009   Ph.D. in Physics, Rutgers University, NJ, USA.

2003   BS in Applied Physics and Applied Mathematics, Moscow Institute for Physics and Technology, Dolgoprudny, Russia.

2006-2009 Graduate Assistant, Department of Physics and Astronomy, Rutgers University, NJ.

2004-2006 Graduate School Fellow, Rutgers University, NJ.

Publications

Andrei Malashevich and David Vanderbilt, *First-principles study of improper ferroelectricity in TbMnO$_3$*, Phys. Rev. Lett. **101**, 037210 (2008).

Andrei Malashevich and David Vanderbilt, *First-principles study of polarization in Zn$_{1-x}$Mg$_x$O*, Phys. Rev. B **75**, 045106 (2007).